A detailed study of lost-particle backgrounds in the detector was also carried out to simulate the detector backgrounds due to beam-gas interactions at PEP-II. All devices are found to be well within acceptable limits for both average radiation damage and average occupancy, having typical safety factors relative to conservative limits of more than 20 for a five-year operating life. We have also examined the effects of the radiative Bhabha process and find it gives acceptably low backgrounds.

4.3 COLLECTIVE EFFECTS

In Chapter 3 we discussed the alternatives that might be considered in the design of a high-luminosity B factory, and indicated the reasons for the choices we have made for PEP-II. The lattice design presented in Section 4.1 is based on these choices. Having fixed these parameters, it is necessary to investigate the influence of the various intensity-dependent effects on the actual performance of the accelerator.

The main parameters we must achieve in PEP-II include:

- Beam energies of 9 GeV (HER) and 3.1 GeV (LER)
- Beam currents of 0.99 A (HER) and 2.14 A (LER)
- Bunch length of 1 cm
- Beam emittances of approximately 50 nm·rad (HER) and 66 nm·rad (LER)
- Beam energy spread of $\sigma_E/E \leq 1 \times 10^{-3}$

In terms of collective effects, the dominant issue is the relatively high beam current that must be supported in each ring. As was discussed briefly in Chapter 3, and as will be covered in more detail in Section 4.4, this constraint is associated mainly with the fact that the beam-beam tune shift parameter is taken to be a design limit, which means that the high luminosity must come mainly from the combined benefits of low beta functions and high currents.

A beam circulating in a storage ring interacts with its surroundings electromagnetically by inducing image currents in the walls of the vacuum chamber and other "visible" structures, such as beam position monitor (BPM) electrodes, kickers, RF cavities, bellows, valves, etc. This interaction leads, in turn, to time-varying electromagnetic fields that act on the beam and can give rise to instabilities. In most electron-positron colliders, single-bunch effects are the primary concern. The current threshold for these effects is defined by the ring impedance at high frequencies, $f > 8$ GHz, which correspond to wavelengths λ comparable to or less than the bunch length, say, $\lambda \leq 4\sigma_\ell$.

The issues with which we must deal for PEP-II fall into the broad categories of single-bunch and multibunch phenomena. Single-bunch phenomena include:

- Longitudinal and transverse single-bunch instabilities
- Beam loss from intrabeam (Touschek) scattering
- Beam loss from beam-beam (Bhabha) scattering
- Higher-order-mode (HOM) heating

Beam-gas scattering, though actually a single-particle effect, can be included in this category, as can the phenomenon of ion trapping in the electron beam.

For the PEP-II, however, the main concern is from coupled-bunch instabilities, where different bunches "communicate" through the narrow-band (high-Q) ring impedances. That is, wakefields deposited in various high-Q resonant objects can influence the motion of following bunches and can cause the motion to become unstable if the beam currents are too high. To effectively couple the bunch motion, HOMs must have a damping time $\tau \approx 2Q/\omega$ longer than the bunch spacing s_B/c. For modes with $Q \leq 100$, this restricts the frequencies $f \leq 8$ GHz. The frequency limit is lower for smaller Q. This effect is one of the most serious issues for the PEP-II design.

For PEP-II, we have opted for a situation in which the nominal beam currents of 0.99 A in the HER and 2.14 A in the LER are distributed in many (1658) bunches. Our reasoning is as follows: The multibunch instabilities are mainly driven by the total beam current, with little regard to how it is distributed in the ring. That is, once the bunch separation is small enough for bunches to fully see wakefields left by preceding bunches, the growth rates are independent of the details of the bunch pattern. Thus, if a high beam current is needed, coupled-bunch instabilities become almost unavoidable. If we choose a relatively small number of bunches to make up the high current, we do little to improve the situation with regard to coupled-bunch instabilities and simply make the single-bunch phenomena harder to manage—in effect requiring the accelerator designers to wage a two-front war. (This usually translates into impedance requirements for the ring that are difficult to meet.) It is true, of course, that the bandwidth requirement of a feedback system to deal with coupled-bunch motion is eased if the bunch spacing increases. However, we do not feel that this is a major limitation (see Section 5.6 for details), and it should not dominate the design decisions.

Given our decision to utilize many bunches, the parameters of the single bunches (emittances, bunch length, intensity) are not unusual—they are in the parameter regime in which PEP and many other colliders have run successfully for many years. This, in turn, means that heroic efforts at impedance reduction are not required to avoid problems with single-bunch effects.

4.3.1 Single-Bunch Issues

In this section, we focus on the issues of single-bunch instability thresholds, beam lifetime, and heating of the chamber due to parasitic HOM losses. We also discuss the issue of ion trapping and the means available to avoid or eliminate it. Before beginning, we digress briefly to define the beam impedances that drive the various instabilities.

4.3.1.1 Impedances. Beam instabilities can occur in either the longitudinal or transverse phase planes. Longitudinal instabilities are driven by voltages induced via interactions of the beam with its environment. The strength of the interaction can be characterized by the ring impedance $Z_{\|}(\omega)$, in ohms, which is defined by

$$V_{\|}(\omega) = -Z_{\|}(\omega)\, I_b(\omega) \tag{4-3}$$

where $V_{\|}(\omega)$ is the longitudinal voltage induced in the beam per turn arising from a modulation of the beam current $I_b(\omega)$ at some particular angular frequency ω.

Transverse instabilities arise from the transverse dipole wakefield, which gives a force that increases linearly with transverse distance from the electromagnetic center of the vacuum chamber and is antisymmetric in sign about that center. The transverse impedance (in Ω/m) is defined by

$$Z_{\perp}(\omega) = \frac{-i\int_0^{2\pi R} F_{\perp}(\omega,s)\,ds}{e\Delta I_b(\omega)} \tag{4-4}$$

where $F_{\perp}$ is the transverse force, integrated over one turn, experienced by a charge e having transverse displacement Δ. Explicitly, $F_{\perp}$ is given by

$$F_{\perp} = e\hat{\theta}(E_{\theta} + B_r) + e\hat{r}(E_r - B_{\theta}) \tag{4-5}$$

In a typical storage ring, the impedance seen by the beam can be loosely characterized as being either broadband or narrow-band. Sharp discontinuities in the vacuum chamber act as local sources of wakefields. These fields have a short time duration, which means that they include many frequency components, and we refer to the corresponding impedance as broadband.

The main contribution to the narrow-band impedance comes from the RF cavities. The approach we have adopted for PEP-II, using a small number of damped RF cavities, serves to substantially reduce the narrow-band impedance. Calculations and measurements with a prototype low-power cavity (see Section 5.5) have confirmed that the strongest HOMs of the damped cavities can be reduced to $Q \le 70$ without degradation of the fundamental mode. For the impedance estimates we use results of the code URMEL from Corlett [1992], which are in good agreement with the measured HOM spectrum [Byrd, 1993] given in Table 4-23.

The narrow-band longitudinal impedance of a cavity for low frequencies $\omega < \omega_{max}$ may be described as the sum over the modes

$$Z(\omega) = i\sum_{\omega_m<\omega_{max}} k_l \left[\frac{1}{(\omega-\omega_m)+i(\omega_m/2Q_m)} + \frac{1}{(\omega+\omega_m)+i(\omega_m/2Q_m)}\right] \tag{4-6}$$

For high frequencies $\omega > \omega_{max}$, a broadband high-frequency tail should be added. We can express the overall impedance as a series expansion over $\sqrt{\omega}$:

$$Z(\omega) = -i\frac{L\omega}{c^2} + R_W\sqrt{\omega} + R_{\Omega} + (1+i)Z_{cav}\sqrt{\frac{\omega_0}{\omega}} + \cdots \tag{4-7}$$

where the first term describes an inductive impedance, the second term represents the resistive-wall impedance, the third term corresponds to a constant resistivity, and the last describes the high-frequency impedance tail of the RF cavities. This part of the

Table 4-23. Monopole modes below cutoff.

f (MHz)	k_ℓ (V/pC)	R/Q (Ω)	Q
476	0.1694	113.2	30000
758	0.107	44.97	28
1016	0.000	0.006	246
1285	0.031	7.68	66
1296	0.027	6.57	907
1588	0.025	5.06	178
1821	0.000	0.06	295
2109	0.023	3.52	233
2168	0.000	0.01	201
2253	0.008	1.21	500

impedance rolls off as $\omega^{-1/2}$, in accordance with simulations and the Dôme-Lawson analytic result for a pillbox cavity with attached beam tubes.

The "shunt impedance" of a mode, R_n, gives the peak value of Re $Z(\omega)$ at the resonance. The loss factor of a mode is related to R/Q by

$$k_\ell = \frac{\omega}{2}\left(\frac{R}{Q}\right) \tag{4-8}$$

The total loss factor is given by a convolution of the impedance with the bunch spectrum $\rho(\omega)$;

$$k_{\text{tot}} = \frac{2}{cZ_0}\int_{-\infty}^{\infty} Z(\omega)\rho^2(\omega/c)\,d\omega \tag{4-9}$$

According to TBCI, a reentrant RF cavity with the dimensions shown in Fig. 5-93 has a loss factor $k_\ell = 0.515$ V/pC.

The parameter Z_{cav} can be defined by comparing the total loss calculated from Eqs. 4-6 to 4-8 with that given by TBCI. The parameter ω_{max} is somewhat arbitrary, in the sense that results are not sensitive to its value. For $f_{\text{max}} = 1260$ MHz, $Z_{\text{cav}} = 5.31$ kΩ.

RF Cavity. The wakefield of a cavity with an impedance of the type given by Eqs. 4-6 and 4-7 reproduces the wakefield of a cavity given by TBCI, Fig. 4-71. Indeed, an impedance of this form is actually a general expression that satisfies the conditions of causality and has the correct analytic properties.

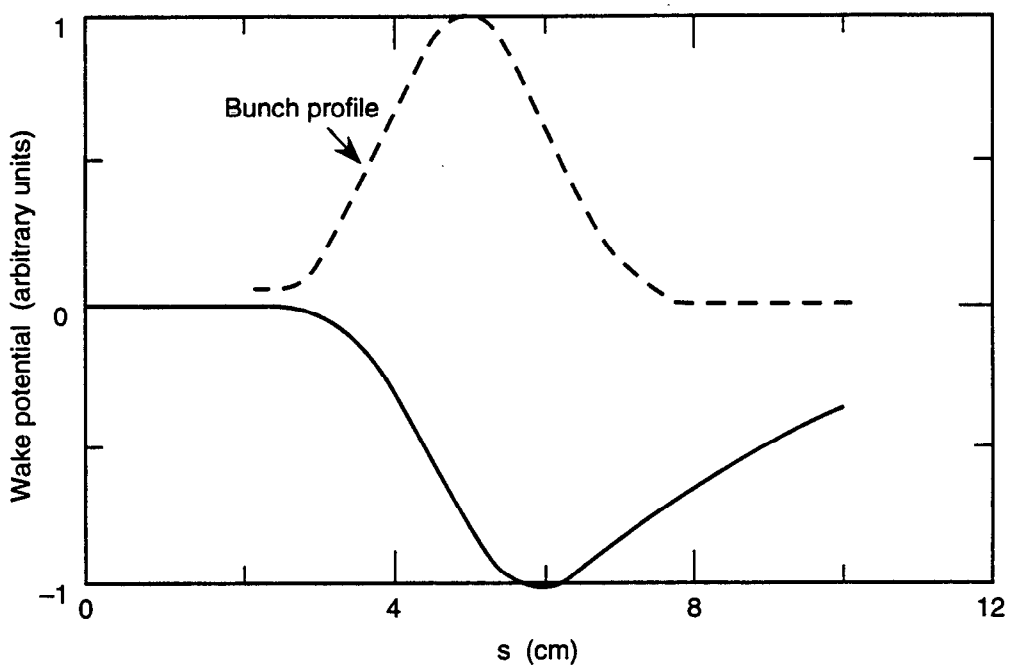

Fig. 4-71. Wakefield of PEP-II RF cavity calculated with TBCI.

The low-frequency limit $\omega \ll \omega_n$ of the narrow-band impedance (Eq. 4-6) is inductive; that is, as $\omega \to 0$,

$$Z(\omega) \to -i\frac{L\omega}{c^2} \tag{4-10}$$

where

$$L = \frac{4\pi}{Z_0}\sum_n \left(\frac{R}{Q}\right)_n \frac{c}{\omega_n} \tag{4-11}$$

(The sum in Eq. 4-11 should not include the fundamental mode of the cavity.) Note that the ratio $(Z/n)_0$ in this limit is independent of frequency and often is used as a single parameter describing the impedance. In our case, $(Z/n)_0 = 9.3\ \text{m}\Omega$ for one RF cavity.

At high frequencies, the narrow-band impedance is capacitive. It rolls off as ω^{-2} and is thus small compared with the high-frequency tail given by Eq. 4-7, which is the quantity relevant for single-bunch stability:

$$\frac{Z(n)}{n} = (1+i)\frac{Z_{\text{cav}}}{n^{3/2}}. \tag{4-12}$$

With Z_{cav} and (Z/n) as given above, this can be written as

$$\frac{Z(n)}{n} = (1+i)\left(\frac{Z}{n}\right)_0 \left(\frac{c}{\omega b_{\text{eff}}}\right)^{3/2} \tag{4-13}$$

where $b_{\text{eff}} = 4.96$ cm. At the bunch frequencies $\omega/c \approx 1/\sigma_\ell$, this is very close to the SPEAR-scaling relationship

$$Z/n \propto \left(\frac{\sigma_\ell}{b}\right)^{1.68} \tag{4-14}$$

where b is taken as an effective beam-pipe radius.

The impedance of the cavities (Eq. 4-12) rolls off as $n^{-3/2}$ and is thus small at high frequencies. Other components of the impedance, such as the resistive-wall impedance

$$\frac{Z(n)}{n} = Z_0\left(\frac{1-i}{2}\right)\frac{\delta}{b} \tag{4-15}$$

where δ is the skin depth, and the inductive impedance of the ring, $Z/n = -iL/c^2$, roll off more slowly and may become important in this high-frequency limit.

Resistive Wall. The PEP-II beam pipe is copper with a roughly elliptical cross section having half-axes of dimension 4.5 × 2.5 cm in the arcs (total length 6 × 243.2 m) and round stainless-steel pipe with radius 4.6 cm in the straight sections (total length 6 × 123.4 m). The average resistive-wall impedance is [J. Corlett, 1992]

$$\left\langle\frac{Z}{n}\right\rangle_{\text{RW}} = (1-i)\,\frac{2.55}{\sqrt{n}} \tag{4-16}$$

The change in conductivity going from copper to stainless steel produces some additional impedance that can be described as a change of the beam-pipe radius by a skin depth of the stainless-steel pipe, δ_{SS}. This results in an impedance

$$Z \simeq \frac{Z_0}{\pi}\frac{\delta_{SS}}{b} \tag{4-17}$$

which is negligibly small.

At the bunch frequencies $n \approx R/\sigma_\ell = 3.5 \times 10^4$, the resistive-wall impedance is larger than the total impedance of 10 RF cavities by a factor of 1.5, whereas at the bunch spacing frequencies $n \approx s_B/\sigma_\ell = 120$, it is smaller by a factor of 5.5×10^{-3}. Because Eq. 4-16 scales as $\sigma_\ell^{1/2}$, we might expect that SPEAR-scaling will not be valid for the short PEP-II bunches.

The rest of the impedance comes from the many small impedance-generating elements of the ring. A list of some of these elements is given in Table 4-24 for a half-sextant of the ring.

Miscellaneous Elements. The stainless-steel vacuum pipe in the straight sections is connected by two tapers per sextant, or 12 tapers per ring, to the octagonal copper tubes in the arcs. The beam pipe is separated from the vacuum DIP chamber by a slotted 5-mm-thick screen. There are six rows of longitudinal slots in the wall with 10 slots per meter, each slot 9 cm long and 0.2 cm wide. The total number of slots in the HER is about 60,000. Each cell has a shielded bellows at each quadrupole. There are also two

Table 4-24. Average number of the impedance-generating elements in a half-sextant (1/12) of the high-energy ring.

Component	Number of items
Flanges	60
BPMs	12
Vacuum ports	24
Bellows	24
Valves	1
Tapers	1
Slots of DIP screen	3000

vacuum ports per cell at each quadrupole for the lumped vacuum pumps. A 4-button design has been chosen for the BPM, with a button diameter of 1 cm and a 1-mm groove around each button. There are 18 valves in the HER (two valves per sextant at the ends of the arc sections, two valves in each RF section, and two valves in the interaction region). For the impedance estimate, flanges are taken simply as shallow grooves. Additional impedance-generating elements, not included in Table 4-24, include three kickers for the feedback system, several collimators, the injection port, and the various masks in the IR. Some special elements such as diagnostic devices, which are not considered at the present time, may be added later. These will not have a noticeable effect on the total impedance. Details on the vacuum chamber hardware may be found in Section 5.2. We note here that special efforts have been made in designing elements of the vacuum system to have minimum impedance by using shielded bellows, by tapering all shape transitions, by screening the vacuum ports and the pumps, etc.

The impedance of the ring may be estimated as the sum of the impedances of the individual elements. (Any cross-talk between elements tends to decrease the total impedance, making such an estimate conservative.) Most of these elements are discontinuities having resonant frequencies much higher than the frequencies within the bunch spectrum. They give rise, therefore, to a predominantly inductive impedance. This was confirmed by calculating wakefields of these elements with the code TBCI. For example, the wakefield of a shielded bellows, modeled as several shallow tapers, made up from a synchrotron mask and sliding contacts, is shown in Fig. 4-72. The wakefield of a $\sigma_\ell = 1$ cm bunch behaves like the derivative of the bunch density, as is typical for an inductive impedance. The maximum value of the wakefield, $W_{\max}$, is related to the inductance L of the bellows by

$$W_{\max} = \frac{L}{\sigma_\ell^2 \sqrt{2\pi e}} \tag{4-18}$$

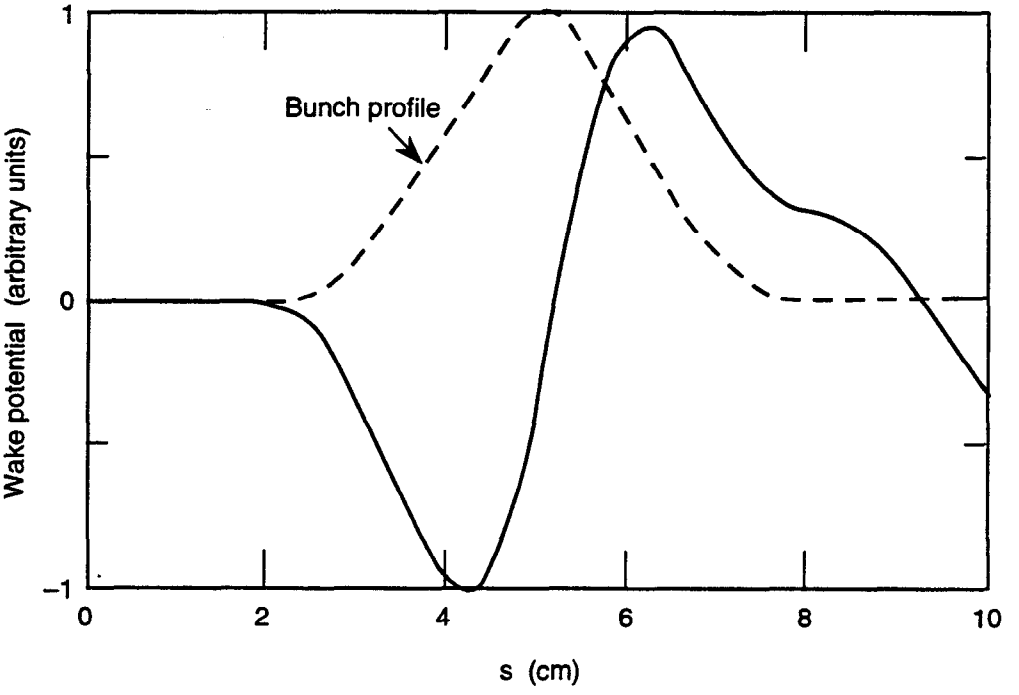

Fig. 4-72. Wakefield of PEP-II shielded bellows calculated with TBCI.

TBCI gives $W_{max} = 0.0121$ cm^{-1}, which correspond to an inductance $L = 0.05$ cm per bellows. Additional impedance is generated by the slots between the sliding fingers of the bellows. The impedance of a rectangular slot having a width w has been found analytically [Kurennoy, 1991] to be

$$\frac{Z(n)}{n} = -\frac{i}{3}\frac{Z_0}{4\pi^2}\frac{w^3}{Rb^2}. \tag{4-19}$$

The total contribution of the 24 slots per bellows, averaged over the azimuth of b, $2.5 < b < 4.5$ cm, is $L = 6 \times 10^{-3}$ cm. The total inductance of a bellows is 5.6×10^{-2} cm, or

$$\frac{Z}{n} = -i\,30\left(\frac{L}{R}\right) = -i\,1.4 \times 10^{-2}\,\Omega \tag{4-20}$$

for 288 bellows in the ring.

For purely inductive elements, the loss factor is zero. Indeed, the loss factor of a bellows given by TBCI is small, $k_\ell = 2.2 \times 10^{-3}$ V/pC per bellows, and strongly depends on the bunch length. We take this loss into account as a constant resistance that would give the same loss

$$R_\Omega = \frac{Z_0\sigma_\ell}{2\sqrt{\pi}}k_\ell = 67.4\ \Omega/\text{ring} \tag{4-21}$$

The loss factor of a hole is a second-order effect (proportional to w^5 and completely negligible). Measurements of the loss factor of a 6-in. PEP valve gave $k_\ell = 0.006$ V/pC,

which corresponds to $R_\Omega = 8.5\ \Omega$ per ring. The loss at PEP-II may be higher by $\sqrt{2}$ due to its shorter bunch length. We can similarly estimate the impedance of the vacuum ports, shielded by ten 14×0.2 cm slots, giving $Z/n = 5 \times 10^{-5}\ \Omega$ for 24 ports in the ring.)

The DIP screen slots can be modeled in the same way, giving a total contribution per ring of $Z/n = -i\ 0.03\ \Omega$.

For an impedance estimate, a flange can be modeled as a shallow cavity with inner and outer radii a, b, where $b - a \ll a$. For small gaps, $g \ll a$, the inductance [Bane, 1988] is

$$L = 2g\left(\frac{b-a}{a}\right) \tag{4-22}$$

If we take $a = 3$ cm for the inner radius, $b = a + 0.1$ cm for the outer radius, and a cavity gap of 0.25 mm, then $Z/n = -i1.1 \times 10^{-3}\ \Omega$ for one ring. TBCI gives the loss factor for such a cavity as $k_\ell = 2.46 \times 10^{-5}$ V/pC. The total contribution of the 576 flanges in one ring is $k_\ell = 0.018$ V/pC.

The impedance of a taper scales with the angle as $\sqrt{2\theta/\pi}$. The angle of the taper should be small compared with the ratio σ_ℓ/b. We chose 10° tapers. Modeling the transitions between straight sections and arcs together as a pair of tapers (the first a taper out, the second a taper in) has also been considered. This approach gives a more realistic result than simply adding the losses of two tapers independently. The loss of a pair of tapers calculated for the azimuthally symmetric pair and then multiplied by the azimuthal filling factor $4.5/(4.5 + 2.5) = 0.643$ is $k_\ell = 2.0 \times 10^{-2}$ V/pC. That gives $k_\ell = 0.125$ V/pC for 12 tapers in a ring, corresponding to $R_\Omega = 29.5\ \Omega$. The s-dependence of the wakefield corresponds to that of an inductive impedance and is similar to the wakefield of a bellows with $W_{\max} = 0.348$ V/pC. The inductance of the 12 tapers is $L = 11.46$ cm and gives

$$\mathrm{Im}\left[\frac{Z(n)}{n}\right] = 1.2 \times 10^{-2}\ \Omega$$

Some elements of the ring, such as feedback kickers and BPMs, have low-Q resonances at high frequencies, of the order of 10 GHz, that give an inductive tail at the bunch frequencies. Measurements of the beam impedance of a button electrode [Jacob et al., 1989] show resonances as summarized in Table 4-25. The low-frequency limit given by these modes, calculated from Eq. 4-11, is

$$\left(\frac{Z}{n}\right)_0 = -i \sum_n \left(\frac{R}{Q}\right)_n \frac{\omega_0}{\omega_n} \tag{4-23}$$

which gives $(Z/n) = 1.9 \times 10^{-7}\ \Omega$ per button. For 144 four-button BPMs, the total impedance is $(Z/n)_0 = 1.1 \times 10^{-4}\ \Omega$. The peak impedance at the resonance frequency of 3.3 GHz is $Z/n = 2.47 \times 10^{-6}\ \Omega$ per button, or $Z/n = 1.42 \times 10^{-3}\ \Omega$ per ring. This is completely negligible in comparison with, say, the resistive-wall impedance, which is $Z/n = 1.36 \times 10^{-2}\ \Omega$ at the bunch frequency $\omega = c/\sigma_\ell$ or $n = R/\sigma_\ell$. Hence, the resonant contribution of the BPMs can be neglected. The impedance of the BPMs, therefore, may be described as purely inductive. The inductance could alternatively be estimated by considering a number of holes with a diameter $w = 1$ mm equal to the diameter of the

Table 4-25. Resonances of a button electrode.

f (GHz)	Q	R_s (Ω)
3.3	17	0.06
16.2	470	0.72
18.3	110	0.46

BPM gap and a total surface area equal to the surface area of the gap. Impedance of such a hole is

$$\frac{Z(n)}{n} = -i\left(\frac{Z_0}{48\pi^2}\right)\left(\frac{w^3}{Rb^2}\right) \tag{4-24}$$

giving $(Z/n) = -i\ 1.3 \times 10^{-4}\ \Omega$ for 144 BPMs. We take this more conservative estimate for the contribution to the total impedance budget.

The total loss factor of the 144 BPMs in the ring due to the resonant modes is $k_\ell = 0.20$ V/pC. It should be mentioned that the contribution of the original PEP BPMs to the loss factor was found to be below the accuracy of the measurements.

The impedance of the three kickers for the longitudinal feedback system can be described [Corlett, 1992] as a $Q = 7$ resonance at $f = 16.2$ GHz, with a shunt impedance of $R = 170\ \Omega$. Other modes have parameters given by the sum of the resonant modes listed in Table 4-26. The total loss factor of the feedback system is $k_\ell = 2.15$ V/pC, and, for comparison, the low-frequency limit is $(Z/n) = 3.4 \times 10^{-3}\ \Omega$.

Coherent synchrotron radiation may produce at its maximum value a noticeable impedance:

$$(Z/n)_{\max} = 300\left(\frac{b}{R}\right) \approx 0.04\ \Omega \tag{4-25}$$

Table 4-26. HOM modes of the PEP-II longitudinal feedback kickers.

f (GHz)	R/Q (Ω)
2.6	9.3
3.1	2.2
3.3	3.5
5.0	1.8

However, the threshold frequency is very high

$$\left(\frac{\omega\sigma_\ell}{c}\right)_{\text{thr}} \approx \left(\frac{\sigma_\ell}{R}\right)\left(\frac{\pi R}{2b}\right)^{3/2} = 37$$

and the effect is suppressed exponentially.

The IR within ±80 cm from the IP has been described as a three-dimensional system of tapers and the impedance has been estimated using TBCI with proper azimuthal averaging. The wakefield found by TBCI corresponds to an inductive impedance with $W_{\max} = 0.62$ V/pC, giving an inductance of $L = 2$ cm and an impedance of $Z/n = 1.8 \times 10^{-3}\ \Omega$. The loss factor of this portion of the IR is $k_\ell = 0.059$ V/pC or $R_\Omega = 12.5\ \Omega$.

The impedance of crotches and the injection port must be similar to the impedance of the septa in the SLC damping rings; these have been investigated with MAFIA by Bane [1988] and shown to give an inductive impedance with $L = 2$ cm.

Fabrication errors and misalignments of the sections of the vacuum pipe can give additional impedance. For example, the misalignment Δ of two adjacent sections of beam pipe with a radius b results in a real impedance $(Z_0/\pi)(\Delta/b)$ and a reactive impedance with inductance $L = 6\Delta^2/b$. Five hundred joints with $\Delta = 1$ mm and $b = 5$ cm give an additional inductance of $L = 6$ cm, or $(Z/n)_0 = 0.005\ \Omega$. Tilting of the slots in the DIP screen by an angle θ with respect with the beam plane increases the impedance of a slot of length l and width w by a factor of $[1 + (l/w)\theta]$. This defines the tolerance of the tilt angle $\theta < w/l \approx 22$ mrad, which does not give substantial fabrication problems.

The total impedance of the ring is the sum of the impedance of the cavities (Eqs. 4-6 and 4-7), the resistive wall (Eq. 4-16), the constant resistance R_Ω representing losses in the mostly inductive components, and the inductive impedance $-i(Z/n)_0$. Contributions of the individual elements to the total inductive impedance $(Z/n)_0$ are given in Table 4-27.

With a "contingency" $Z(n)/n = 0.024\ \Omega$ for the collimators, the total inductive impedance is $Z(n)/n = 0.10\ \Omega$.

The total longitudinal wake function can be calculated from the longitudinal impedance. It is shown in Fig. 4-73.

Transverse Impedance. The transverse impedance may be estimated as

$$Z_\perp = \frac{Z_\parallel c}{\omega b^2} \tag{4-26}$$

It rolls off with frequency faster than does the longitudinal impedance and is maximum at frequencies close to the cutoff frequency $\omega \approx c/b$.

4.3.1.2 Longitudinal Microwave Instability. The first instability we consider is the longitudinal microwave instability, sometimes referred to as turbulent bunch lengthening. This instability, which has been seen in numerous proton and electron storage rings, is not a "fatal" instability, in the sense that it does not lead to beam loss. Instead, the instability causes an increase in both the bunch length and the momentum spread of a bunched beam. Its threshold (peak) current is given by

Table 4-27. The PEP-II inductive impedance budget.

Component	Impedance (Ω)
BPMs	1.3×10^{-5}
Vacuum ports	5×10^{-5}
Bellows	1.4×10^{-2}
Flanges	1×10^{-3}
Valves	6×10^{-3}
Tapers	1.6×10^{-2}
DIP screen	3×10^{-2}
Feedback system	3.5×10^{-3}
Interaction region	2×10^{-3}
Injection, crotches	3.6×10^{-3}
Total	0.076

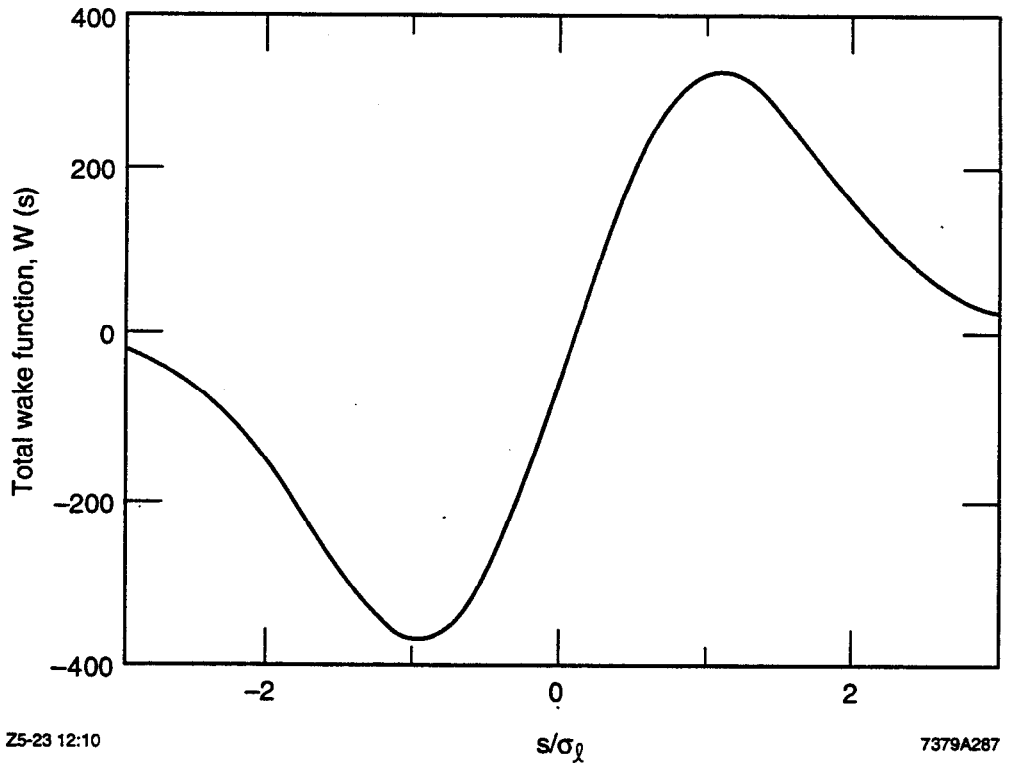

Fig. 4-73. Total longitudinal wakefield for PEP-II HER.

$$I_p = \frac{2\pi|\eta|\,(E/e)\,(\beta\sigma_p)^2}{\left|\frac{Z_\parallel}{n}\right|_{\text{eff}}} \tag{4-27}$$

where $|Z_\parallel/n|_{\text{eff}}$ is the effective broadband impedance of the ring and $\eta = \alpha - 1/\gamma^2$ is the phase-slip factor.

The average bunch current of the LER, 1.3 mA, corresponds to a 113-A peak current for a Gaussian bunch with $\sigma_\ell = 1$ cm. For the LER parameters, $\alpha = 1.31 \times 10^{-3}$, $\sigma_p = (\delta p/p)_{\text{rms}} = 8 \times 10^{-4}$, and $E = 3.1$ GeV, stability requires $|Z/n| \leq 0.144\ \Omega$.

The effective impedance in Eq. 4-27 is defined as the impedance averaged over the bunch spectrum. For short bunches, for which the spectrum is wide compared with the frequency range of the impedance, the relevant parameter is

$$\left|\frac{Z_\parallel}{n}\right|_{\text{eff}} = \frac{\int [Z(n)/n]\,\rho^2(n)\,dn}{\int \rho^2(n)\,dn} \tag{4-28}$$

The main contribution to this integral comes from low frequencies, which are irrelevant to single-bunch stability. Therefore, to properly estimate the effective impedance for single-bunch stability, the integration should be performed starting with the harmonic number n_m corresponding to a wavelength comparable to or smaller than the bunch length. Figure 4-74 depicts $|Z/n|_{\text{eff}}$ and a plot of Re $Z(n)/n$ vs Im Z/n for different values of n_m. In the left column, $n_m = 300$ and the value of the effective impedance is of the order of 2 Ω. The middle column is for $n_m = 3500$, which corresponds to including a maximum wavelength equal to the RF wavelength. The right column in Fig. 4-74 corresponds to a maximum wavelength of $20\sigma_\ell$. This limit already gives acceptable effective impedance. The Z/n at high frequencies is always within the area of stability allowed by Landau damping. A calculation with $n_m = 10500$ (or $20\sigma_\ell$) gives $|Z(n)/n| = 0.185\ \Omega$. It agrees well with the SPEAR-scaling [Chao and Gareyte, 1976] estimate of

$$\left(\frac{Z}{n}\right)_0 \left(\frac{\sigma_\ell}{b}\right)^{1.68} \tag{4-29}$$

with $(Z/n)_0 = 2.4\ \Omega$ for the beam pipe radius $b = 4.6$ cm. This appears consistent with PEP bunch lengthening measurements, which can be described with SPEAR scaling and the parameter $(Z/n)_0 = 3\ \Omega$. However, SPEAR scaling, which can be expected in the situation when the impedance is dominated by the RF cavities, i.e., for long bunches, may be invalid for shorter bunches, as was mentioned above. Figure 4-75 shows the dependence of the effective impedance on the bunch length.

To estimate the growth from the longitudinal microwave instability, we must assume a value for the broadband impedance of the ring. For the PEP-II HER, this value—usually dominated by the RF system in a high-energy storage ring—is expected to be lower than the value of $|Z/n|_0 = 3\ \Omega$ obtained from measurements at PEP [Rivkin, 1987].

The equivalent broadband contribution to the impedance seen by the beam can be estimated, for a given RF system, following the approach of Zisman et al. [1986].

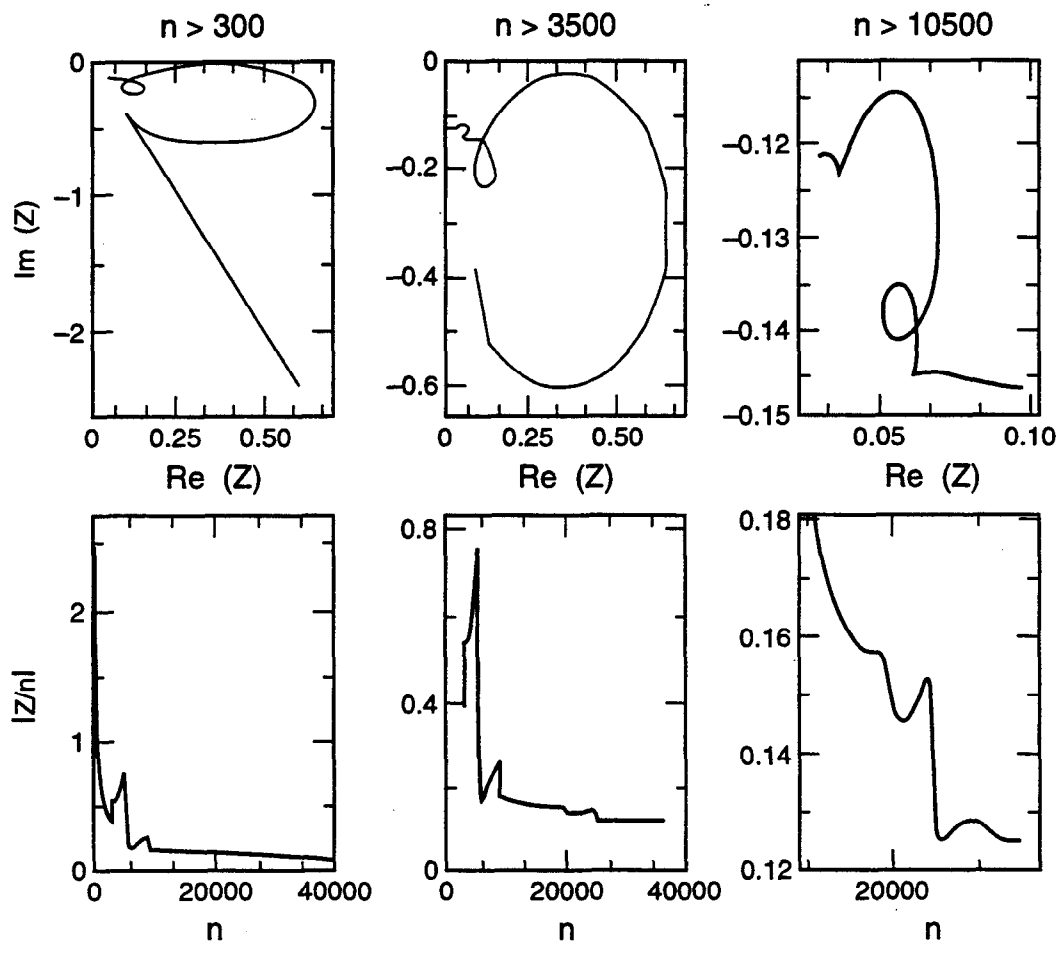

Fig. 4-74. (Upper) Plot of real vs imaginary impedance of PEP-II for various assumptions about $n = \omega/\omega_0$. (Lower) Plot of absolute value of Z/n for various values of low-frequency cutoff n.

Basically, this involves estimating the frequency shift that would be induced in a long beam bunch by the aggregate of the many cavity HOMs, and then determining the strength of a $Q = 1$ broadband resonator that would produce the same effect. That is, we take

$$\left|\frac{Z_{\|}}{n}\right|_{\mathrm{BB,RF}} = \sum_{\mathrm{HOMs}} \left|\frac{Z_{\|}}{n}\right|_j = \sum_j \left(\frac{R_s\,\omega_0}{Q\,\omega_R}\right)_j \tag{4-30}$$

where R_s, ω_R, and Q are the shunt impedance, resonant angular frequency, and quality factor, respectively, of the jth HOM, and ω_0 is the particle (angular) revolution frequency. With this approach, we find that the present PEP RF system contributes an equivalent broadband component of $|Z/n| \approx 0.026\ \Omega$/cell. Applying the same prescription to the PEP-II RF cavity (described in Section 5.5) yields an equivalent broadband contribution of $|Z/n| \approx 0.01\ \Omega$ for the first few trapped modes.

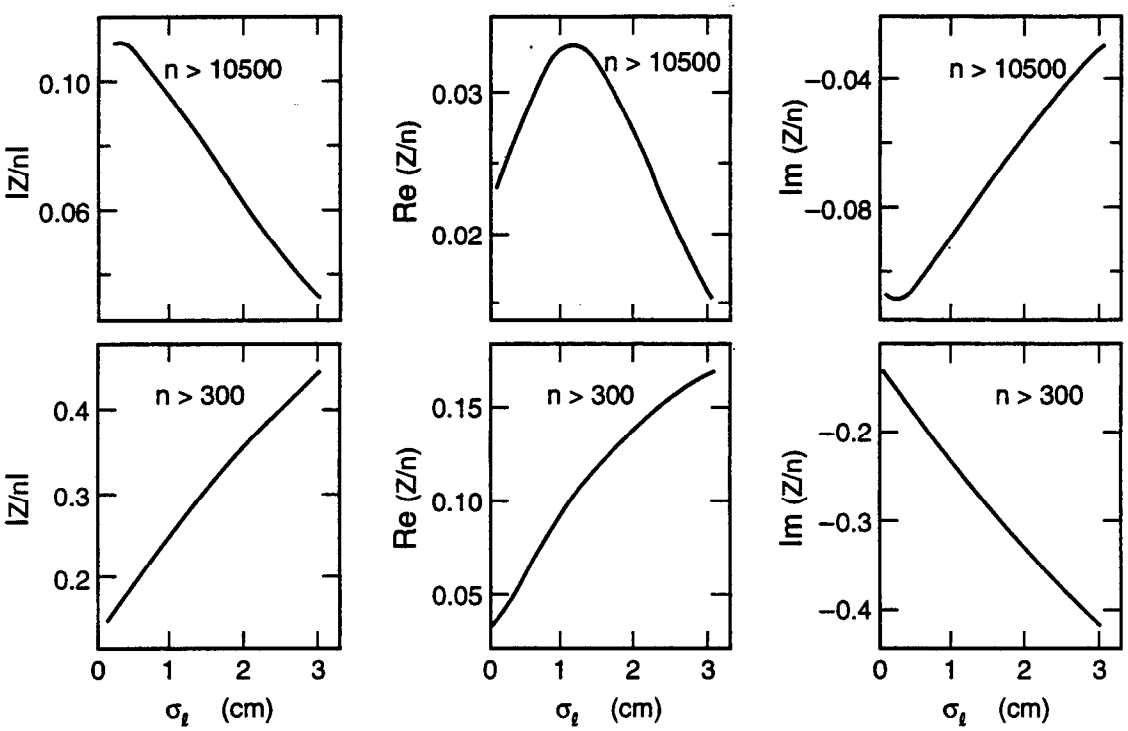

Fig. 4-75. Plots of the absolute value of Z/n (left column), the real part of Z/n (center column) and the imaginary part of Z/n (right column) vs bunch length. The upper row corresponds to a high cutoff frequency (wavelengths of the order of the bunch length); the lower row corresponds to a very low cutoff frequency.

A more significant gain is made by producing the required voltage and providing the required power to the beam (to replenish the losses to synchrotron radiation) with many fewer RF cells than the 120 used now at PEP. In the design described in Section 5.5, the voltage is provided by only 20 RF cells in the HER or 10 cells in the LER. This decrease in the number of cells reduces, by about a factor of six, the broadband impedance in the ring that stems from the RF system (estimated in PEP to be about two-thirds of the total). Thus, we expect to reduce the RF contribution to the broadband impedance to about 0.3 Ω. Clearly, however, the broadband impedance from the other components in the beam path (valves, bellows, BPMs, etc.) must contribute to the total seen by the beam, and there will be additional hardware in the PEP-II rings (for example, feedback kickers) that will have an effect.

The PEP chamber has a broadband impedance of about 1 Ω, and it is prudent, for now, to take the larger value to account for those impedance-producing components that have not been considered yet. With this in mind, for simulations with ZAP, which uses the SPEAR scaling approach (Eq. 4-28), we have adopted a total broadband impedance $|Z/n|_0 = 1.5\ \Omega$ (half that of PEP), which is consistent with the calculated $|Z/n|_{\text{eff}} = 0.18\ \Omega$ for the average beam pipe radius of 3.3 cm. As we will see, even this fairly conservative assumption does not lead to any difficulties in the parameter regime in which the PEP-II rings are designed to operate.

To maintain bunch lengths in both rings that are short compared with the small β^* value of 1.5 cm in the LER, we adopt an RF voltage in the HER of 18.5 MV. As shown in Fig. 4-76a, this voltage gives an rms bunch length of $\sigma_\ell = 1$ cm at the required single-bunch current of 0.6 mA. For the LER (see Fig. 4-76b), a 1-cm bunch at the design current of 1.3 mA can be obtained with a voltage of 5.9 MV.

The expected bunch lengthening beyond threshold is shown in Fig. 4-77a for the HER, based on the threshold formula given in Eq. 4-27. We remain well below the threshold at the required single-bunch current of 0.6 mA. The situation for the LER is shown in Fig. 4-77b; again we are well below threshold at the nominal 1.3 mA/bunch value. The curves in Figs. 4-77a and 4-77b are based on the so-called SPEAR-scaling ansatz, mentioned earlier. It is worth noting here that we have estimated the natural momentum spread of the low-energy beam to be 8×10^{-4}. This relatively large value is associated with the significant amounts of "extra" synchrotron radiation (generated in the wigglers) needed to achieve the proper emittance and to preserve the ability to reach equal damping decrement if need be.

Because the collider must be able to accommodate some energy variability, we have also considered the effects of moderate changes from the nominal operating energies of 9 GeV (HER) and 3.1 GeV (LER). In Fig. 4-78, we show the energy dependence of the microwave threshold current at the specified operating voltages for the two rings. The steepness of these curves is mainly due to the increase in natural momentum spread with energy (see Eq. 4-27). The dependence of the threshold current on voltage is shown for several different energies in Figs. 4-79a (HER) and 4-79b (LER). The preference for higher voltage is a consequence of the decrease in effective impedance as the bunch length decreases.

In our calculations we have ignored the effect of potential-well distortion, which—for short bunches—is predicted to reduce the bunch length; this effect is expected to be minor.

From these estimates, we conclude that there are no problems associated with the longitudinal microwave instability, provided the low-frequency broadband impedance of each ring can be kept at or below 1.5 Ω.

4.3.1.3 Transverse Mode-Coupling Instability. Because the ring is large, we must also consider the transverse mode-coupling instability, which is known [Zisman et al., 1988] to limit the single-bunch current in PEP. This instability arises when the imaginary part of the transverse impedance $Z_\perp$ couples the frequency of the $m = 0$ and $m = -1$ synchrotron sidebands. For long bunches, the threshold is expected to scale as

$$I_b = \frac{4\,(E/e)\,\nu_s}{\left\langle \mathrm{Im}\,(Z_\perp)\,\beta_\perp \right\rangle R} \frac{4\sqrt{\pi}}{3}\,\sigma_\ell \qquad (4\text{-}31)$$

where ν_s is the synchrotron tune, $\beta_\perp$ is the beta function at the location of the impedance, and R is the average ring radius. Although the transverse impedance is expected to decrease for very short bunches [Zisman 1990a], we are operating in a regime where the mode-coupling threshold is more or less independent of bunch length. For the impedance presently expected for the HER, a simple scaling from measured PEP data based on

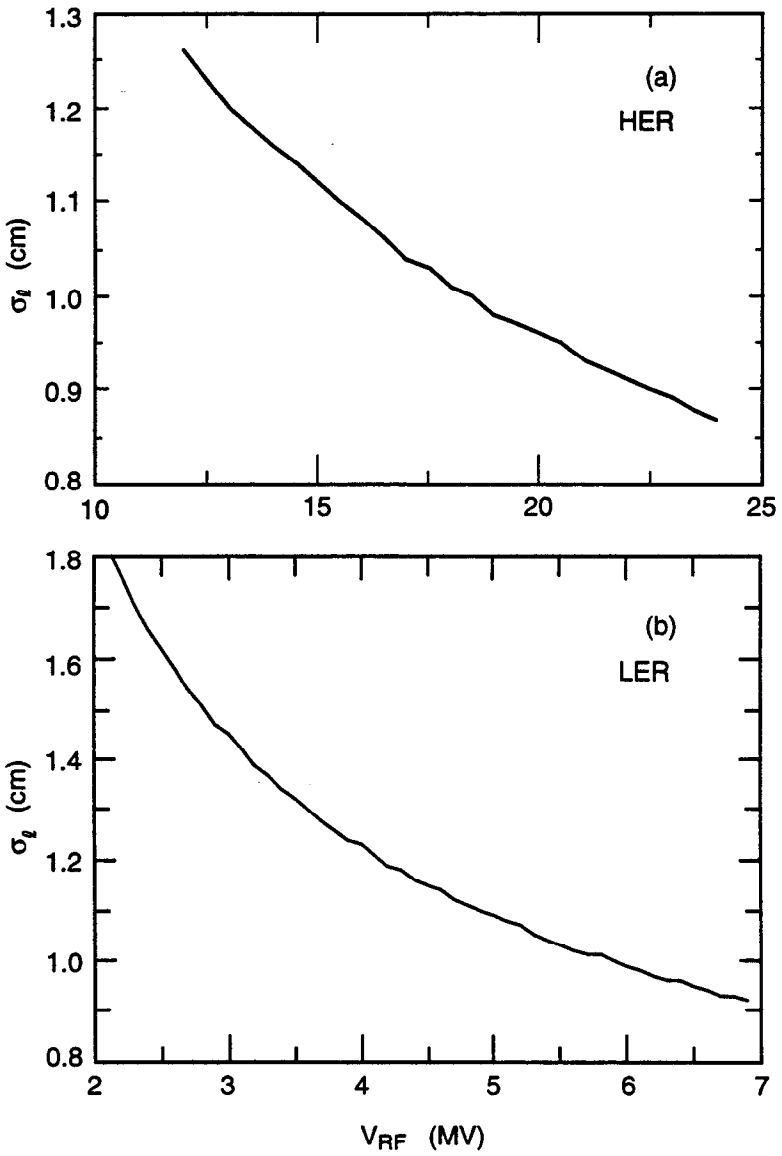

Fig. 4-76. Plot of (a) HER and (b) LER bunch lengths as a function of RF voltage. A 1-cm bunch requires V_{RF} = 18.5 MV in the HER and V_{RF} = 5.9 MV in the LER.

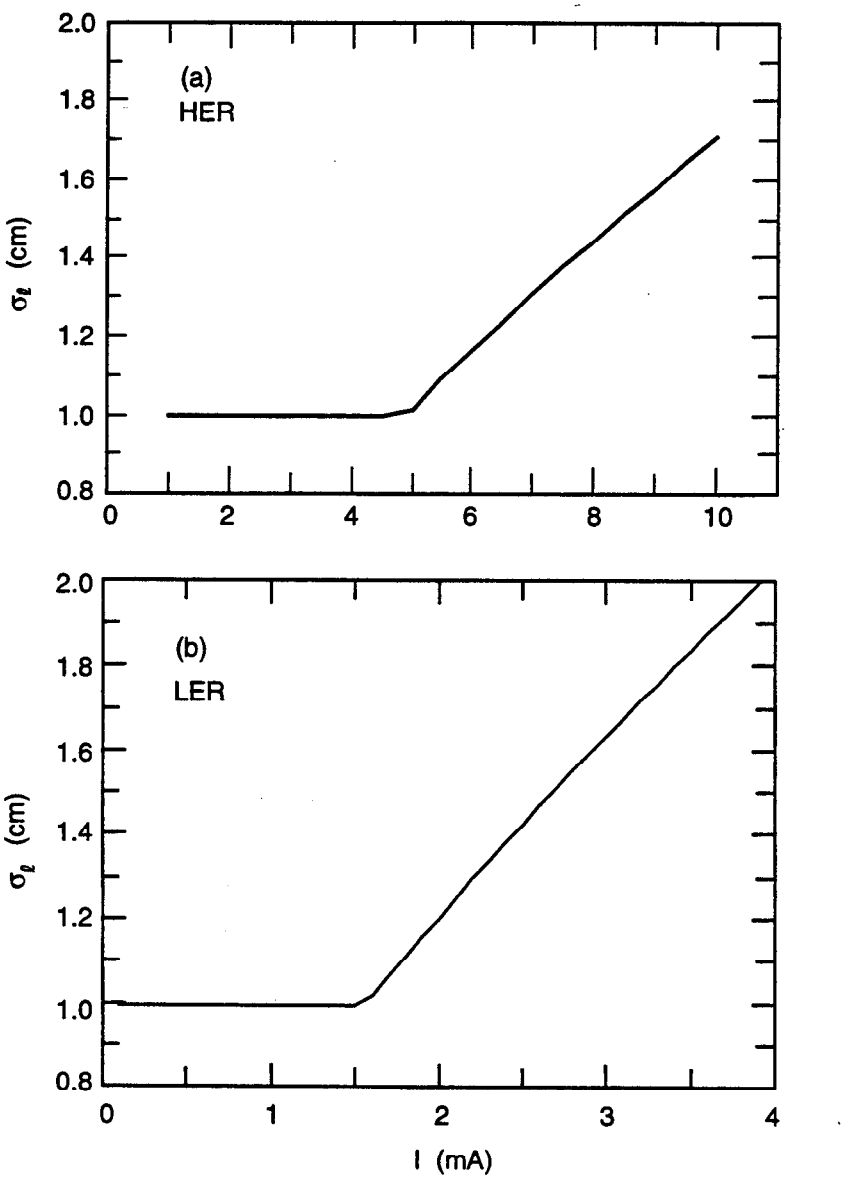

Fig. 4-77. Plot of (a) HER and (b) LER bunch lengths as a function of current, showing the onset of bunch lengthening. Even above threshold, the bunch length increases only slowly with current.

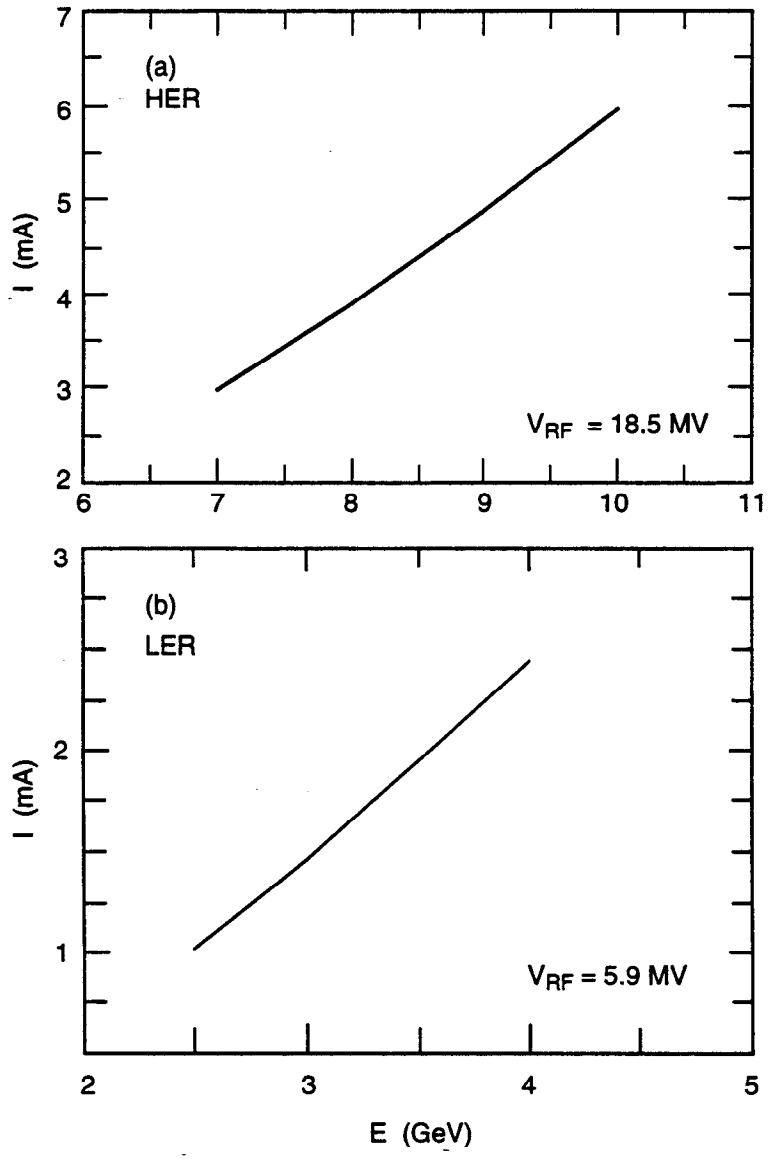

Fig. 4-78. Plot of the microwave threshold current in (a) the HER and (b) the LER as a function of energy, for V_{RF} = 18.5 MV (HER) and V_{RF} = 5.9 MV (LER). The required single-bunch currents of 0.6 mA (HER) and 1.3 mA (LER) are below the instability threshold in this energy range.

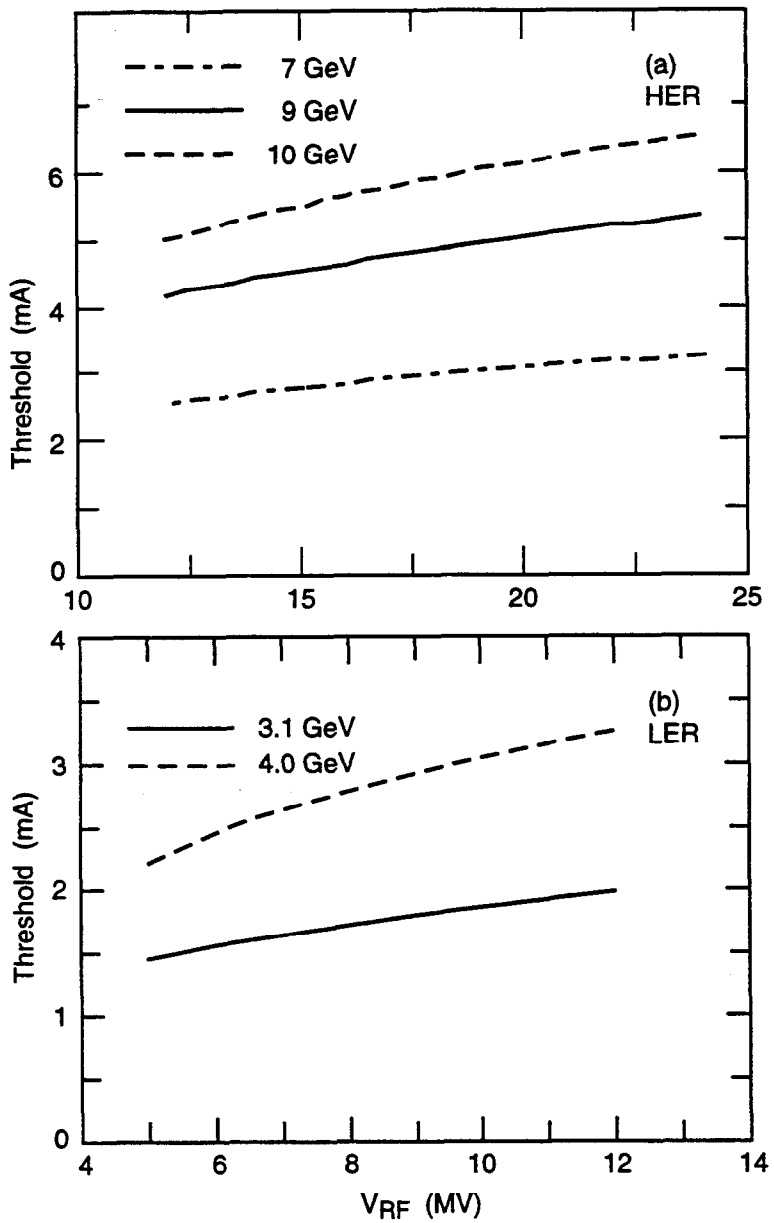

Fig. 4-79. Plot of the microwave threshold current in (a) the HER and (b) the LER as a function of RF voltage, for several beam energies. For the HER, the threshold current is well beyond the required 0.6 mA. For the LER, the threshold current approaches the required operating value of 1.3 mA only for the lowest voltage.

Eq. 4-31, shown in Table 4-28, suggests that the transverse mode-coupling threshold should be somewhat higher for PEP-II than for PEP, even though both the HER and LER will have a lower beam energy than did PEP. The scaled threshold value for the LER, about 10 mA/bunch, is well beyond the required single-bunch current of 1.3 mA and should pose no problem.

To estimate the transverse mode-coupling threshold in each ring more reliably, we used the code MOSES [Chin, 1988]. Initially, we considered a $Q = 1$ resonator impedance having a cutoff frequency of 1 GHz and a transverse impedance of 0.5 MΩ/m. The calculations take into account the effect of bunch lengthening at high currents, which is ignored in the simple scaling arguments presented in Table 4-28. The threshold currents, corresponding to the crossing of the mode $m = 0$ and mode $m = -1$ frequencies, are 37 mA for the HER (Fig. 4-80a) and 8.8 mA for the LER (Fig. 4-80b), in good agreement with the scaling estimates.

Because the RF cavities are no longer expected to be the dominant impedance source, we have also considered the situation in which the transverse impedance comes mainly from the arc vacuum chamber hardware. In this case, the cutoff frequency for $Z_\perp$ increases to 1.9 GHz, and the strength of the impedance (weighted by the fraction of the circumference that consists of arc chambers, roughly 70%) increases to about 1.3 MΩ/m. For these parameters, MOSES predicts the transverse thresholds to be 6.5 mA for the HER and 2.2 mA for the LER.

Table 4-28. Scaling comparison for transverse mode-coupling threshold.

	Low-energy ring	PEP	High-energy ring
E [GeV]	3.1	14.5	9.0
$\beta_\perp$ [m]	20	87	20
R [m]	350	350	350
ν_s [10^{-2}]	3.7	4.6	5.3
$Z_\perp$ [MΩ/m]	0.5	0.8	0.5
Relative factor[a]	1.2	1	5.0
Observed [mA]	—	8.5	—

[a] Factor $= \dfrac{E\nu_s}{Z_\perp \beta_\perp R}$

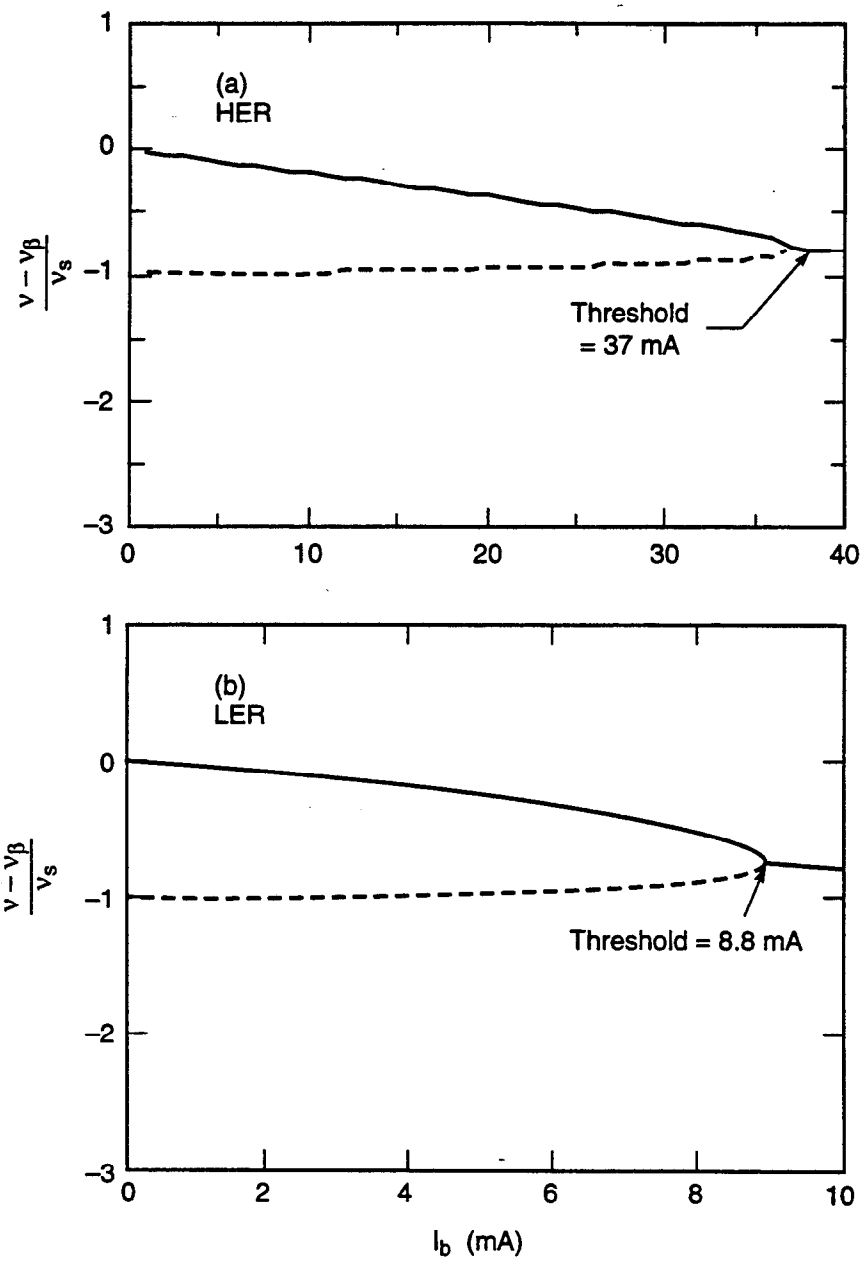

Fig. 4-80. Calculation of transverse mode-coupling instability threshold for (a) the HER, assuming $Z_\perp = 0.5\ M\Omega/m$ and (b) the LER, assuming $Z_\perp = 0.5\ M\Omega/m$. The instability sets in when the $m = 0$ and $m = -1$ frequencies merge. This calculation represents a limitation in the horizontal plane; the vertical limitation is lower (see text).

To put these results in context, we note that the maximum allowable single-bunch current in the PEP-II rings is 1.8 mA, corresponding to 3 A in 1658 bunches. Thus, the transverse mode-coupling instability is not expected to limit the performance of PEP-II.

Although the RF cavities are not the dominant contributors to the transverse impedance, it is still best to "hide" them in a low-beta region of the ring. This should be more easily accomplished in the PEP-II HER than in PEP, because the total length of RF structure will be considerably shorter. Indeed, it would be possible, in principle, to adapt the focusing of the RF straight sections to permit very low beta functions in both planes.

4.3.1.4 Intrabeam Scattering. Although we are considering beams of fairly high energy, the requirements for relatively short bunches and relatively high peak currents make emittance growth from intrabeam scattering (IBS) a possible concern. IBS collisions occur because, in the bunch rest frame, not all particles are moving in the same direction. In general, the temperatures in the transverse phase planes (x and y) are higher than in the longitudinal plane. This results in small-angle multiple scattering occurring mainly in such a way as to transfer momentum from the transverse to the longitudinal plane. However, in dispersive regions of the lattice, this momentum change results in the excitation of a betatron oscillation and thus gives rise to an increase in horizontal emittance.

To be sure this is not a concern, we performed calculations on each of the rings at the lowest energy now being considered: 7 GeV for the HER and 2.5 GeV for the LER. In the HER case, our estimates indicate that no growth is expected. In the LER case, the lower beam energy enhances the IBS growth rates, and the single-bunch current is higher than for the high-energy beam, so we might expect an observable growth. However, in the LER these aspects are compensated by the larger transverse emittance values. Thus, even here we predict no emittance growth from intrabeam scattering.

4.3.1.5 Beam and Luminosity Lifetime. For a high-energy electron beam, there are four main processes that lead to beam loss: Touschek and gas scattering for the single beams, and Bhabha ($e^+e^- \rightarrow e^+e^-$) and radiative Bhabha ($e^+e^- \rightarrow e^+e^-\gamma$) interactions for the beams in collision. For single beams at PEP-II, the first of these effects is not generally important, but the second one is. For the colliding beams, the radiative Bhabha interactions dominate the luminosity lifetime. Lifetimes presented in this section are quoted as mean (that is, $1/e$) values.

Touschek Scattering. The Touschek scattering mechanism is related to the IBS mechanism described above. The main difference is that we are concerned now with large-angle, single-scattering events that change the scattered particle's momentum sufficiently to make it fall outside the momentum acceptance of the accelerator.

The limit on the tolerable momentum deviation from the design value can come from several sources. There is a longitudinal limit from the potential well ("RF bucket") provided by the RF system. Particles deviating in momentum from the nominal value by more than this amount do not undergo stable synchrotron oscillations and are lost. There can also be a transverse limit on momentum acceptance, arising from the excitation of a betatron oscillation when the Touschek scattering event takes place in a dispersive region of the lattice. For large momentum deviations ($\delta p/p \approx$ several percent), the resultant

betatron oscillation can either hit the vacuum chamber wall elsewhere in the lattice (physical aperture limit) or exceed the dynamic aperture of the machine. Because the lifetime for Touschek scattering increases approximately as $(\Delta p/p)^3$, where $(\Delta p/p)$ is the limiting momentum acceptance value, there is the potential for a strong degradation if the acceptance is too low.

For detector background reasons, we envision the possibility of installing collimators in the arcs that would restrict the particle amplitudes to about $10\sigma_x$ motion. To see how this affects the various lifetimes, ZAP has been modified to include this possibility.

The RF voltage in the HER, selected to be 18.5 MV so as to produce short beam bunches, actually provides too large an acceptance ($\Delta p/p$ = 1%) compared with the estimated limitation from the physical aperture ($\Delta p/p$ = 0.7%). This is not beneficial to the lifetime, since it results in a higher bunch density and thus a higher collision probability; this is the price we must pay to obtain short bunches. Fortunately, the Touschek lifetime is not a major concern in this parameter regime, as shown in Fig. 4-81a. At 9 GeV, a Touschek lifetime of 870 hours is predicted for the HER based on the physical aperture limit. If a 10σ limit is applied, the Touschek lifetime is still 188 hours.

In the LER, the physical momentum acceptance limit, $\Delta p/p \approx 1.3\%$, is the same as that of the RF bucket. Although the energy is lower than in the HER, the large acceptance makes the Touschek lifetime about 270 hours, and thus not of concern. With a 10σ aperture restriction, the lifetime becomes 65 hours, which is still quite comfortable. We see (Fig. 4-81b) that a 10σ aperture becomes quite noticeable at the lower energies, where the lifetime drops to below 10 hours.

Gas Scattering. Gas scattering involves collisions with residual gas nuclei present in the vacuum chamber. Such collisions can be either elastic or inelastic (bremsstrahlung). In the former case, particle loss results from the excitation of a betatron oscillation that exceeds the physical or dynamic aperture of the ring; in the latter case, the loss results from a momentum change that exceeds the momentum acceptance of the ring (see discussion above).

The HER must accommodate 0.99 A of circulating beam to reach a luminosity of 3×10^{33} cm^{-2} s^{-1}. This high beam current will give a large desorbed-gas load, and substantial pumping speed is needed to maintain a background gas pressure below 10 nTorr in the ring. The PEP-II vacuum system is designed to produce a pressure of less than 5 nTorr under these conditions, so we base our lifetime estimates on this value (N_2 equivalent).

For the HER (see Fig. 4-82a), the estimated lifetime from gas scattering—dominated by the bremsstrahlung process—is 6 hours at a pressure of 5 nTorr. This beam loss process is much more severe in its effects than the Touschek scattering process; therefore, we have placed great emphasis (see Section 5.2) on a vacuum system design capable of maintaining a good pressure in the presence of a large gas load from synchrotron-radiation desorption. It is worth noting here that our lifetime estimates are somewhat pessimistic in that they are based on a fixed gas pressure. In reality the pressure will decrease as the beam current decreases, making the lifetimes longer than the values quoted here.

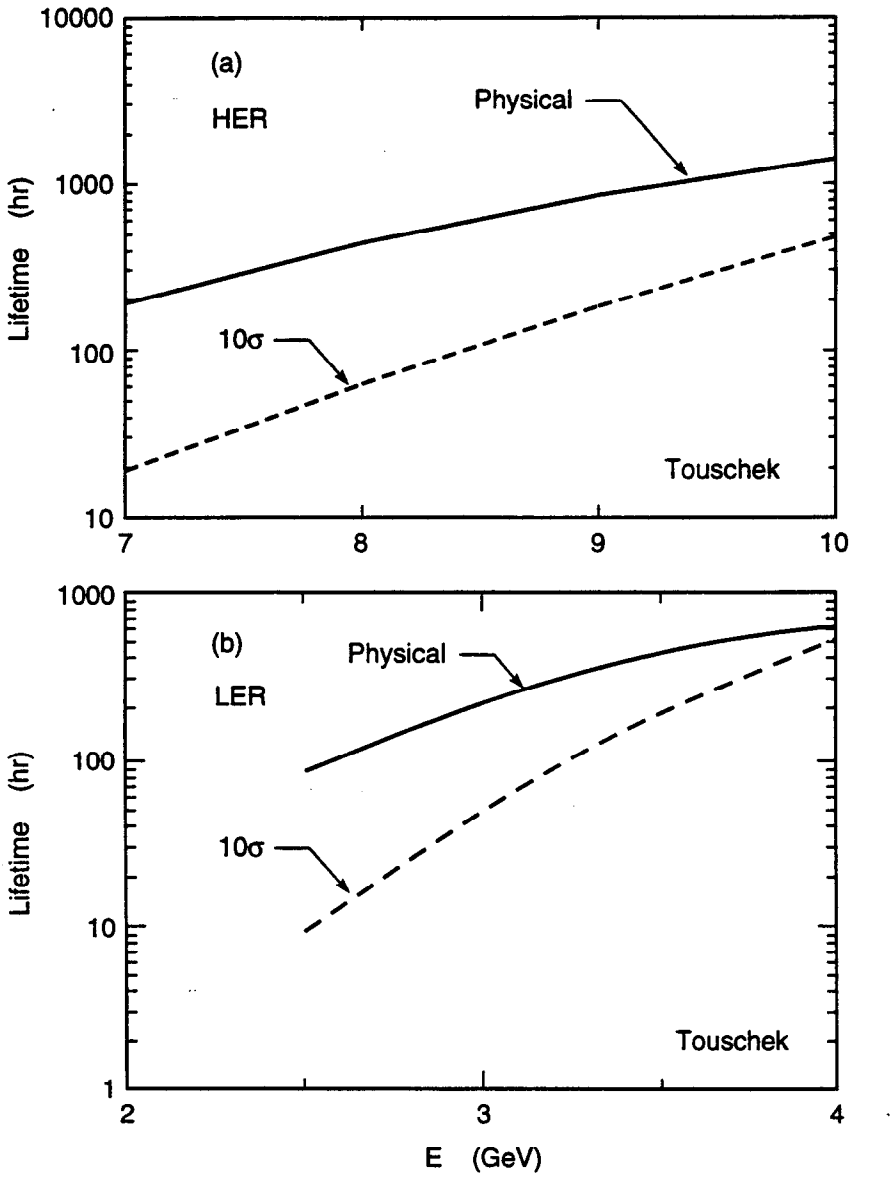

Fig. 4-81. Plot of Touschek lifetime as a function of beam energy in (a) the HER and (b) the LER. The solid line corresponds to taking the physical aperture of the vacuum chamber as the transverse limitation; the dashed line assumes a 10σ aperture restriction in the injection straight section.

For the LER at a gas pressure of 6 nTorr (N_2 equivalent), the lifetime is roughly equally matched between elastic scattering and bremsstrahlung losses (see Fig. 4-82b); the overall beam lifetime is 2.7 hours. Even for the LER, special care must be taken in the design of the vacuum chamber; this topic is discussed in Section 5.2.

Luminosity Lifetime. A potentially important contribution to beam lifetime is the loss of particles due to interactions between the individual particles in the two beams. In

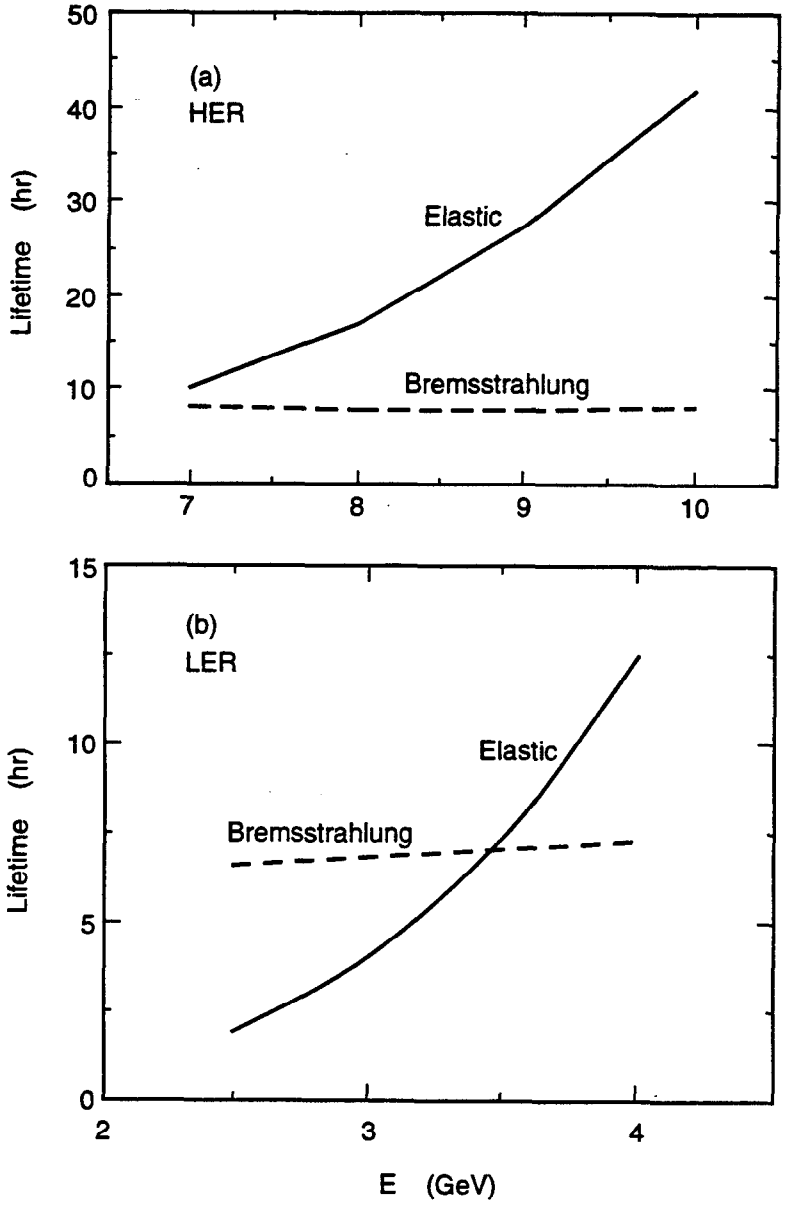

Fig. 4-82. Plot of gas-scattering lifetime as a function of beam energy for (a) the HER and (b) the LER. For the elastic scattering (solid line), an aperture restriction of 10σ was taken in each plane, with the vertical σ being calculated with the fully coupled vertical emittance. An average pressure of 5 nTorr (N_2 equivalent) was assumed for the HER and 6 nTorr for the LER.

particular, we consider the loss of particles due to $e^+e^- \rightarrow e^+e^-$ and $e^+e^- \rightarrow e^+e^-\gamma$ interactions that scatter beam particles outside the accelerator acceptance.

If the e^+e^- cross section leading to loss of a particle from beam i is σ_i, then the loss rate depends on the luminosity according to

$$\frac{dN_i}{dt}(t) = -\sigma_i \mathcal{L}(t) \tag{4-32}$$

Each beam may consist of a number of bunches (not including gaps), n_{bi} with a number of particles per bunch, $N_{bi}(t)$. The subscript b is used to indicate that this is a quantity for a single bunch, and the subscript i refers to the beam (i = +,–). The total number of particles in a given beam is $N_i = n_{bi}N_{bi}$. We introduce the notation $N_{0,i} \equiv N_i(0)$, and we also use $\mathcal{L}_0 \equiv \mathcal{L}(0)$ to denote quantities evaluated at $t = 0$.

To determine the beam and luminosity lifetimes for the processes of interest, we need to know how the luminosity depends on the beam currents. This dependence is determined to some extent by the operation of the storage ring. We adopt here a conservative model that assumes that the bunch sizes do not vary with time. Then the luminosity is given by

$$\mathcal{L}(t) = \frac{N_{b+}(t)N_{b-}(t)n_{bi}f_i}{2\pi\sqrt{\left(\sigma_{x,+}^{*2} + \sigma_{x,-}^{*2}\right)\left(\sigma_{y,+}^{*2} + \sigma_{y,-}^{*2}\right)}} \tag{4-33}$$

The $\sigma_{x,\pm}^*$ and $\sigma_{y,\pm}^*$ in this equation are the transverse rms spot sizes at the interaction point (IP). All time-dependent terms are explicitly indicated. It is assumed that the bunches are distributed such that all bunches meet opposing bunches at the IP (that is, bunches meet bunches and gaps meet gaps), hence $n_{b+}f_+ = n_{b-}f_-$ is the bunch collision frequency. Here, f_i is the revolution frequency for beam i. We also assume that any modifications to the above formula from considerations such as finite bunch lengths and nonzero crossing angles are time independent.

Equations 4-32 and 4-33 lead to two coupled differential equations in the beam currents:

$$\begin{aligned} \frac{dN_+}{dt} &= -k\sigma_+ N_+ N_- \\ \frac{dN_-}{dt} &= -k\sigma_- N_+ N_- \end{aligned} \tag{4-34}$$

where

$$k \equiv \frac{\mathcal{L}_0}{N_{0,+}N_{0,-}} \tag{4-35}$$

The solution is

$$N_+(t) = N_{0,+}\frac{1-r}{e^{Gt}-r}$$

$$N_-(t) = N_{0,-}\frac{1-r}{1-re^{-Gt}} \tag{4-36}$$

where

$$G \equiv \mathcal{L}_0\left(\frac{\sigma_+}{N_{0,+}} - \frac{\sigma_-}{N_{0,-}}\right) \tag{4-37}$$

and

$$r \equiv \frac{N_{0,+}\sigma_-}{N_{0,-}\sigma_+} \tag{4-38}$$

The $1/e$ beam lifetimes are given by

$$\tau_+ = \frac{1}{G}\ln\left[e + r(1-e)\right]$$

$$\tau_- = -\frac{1}{G}\ln\left[\frac{1}{r}(1-e+re)\right] \tag{4-39}$$

The time-dependence of the luminosity is

$$\mathcal{L} = \mathcal{L}_0 e^{Gt}\left(\frac{1-r}{e^{Gt}-r}\right)^2 \tag{4-40}$$

We define the luminosity lifetime τ to be the time it takes the luminosity to reach $1/e$ of its initial value:

$$\tau = \frac{1}{G}\ln\left\{\frac{e}{2}\left[(1-r)^2 + 2r/e + (1-r)\sqrt{(1-r)^2 + 4r/e}\right]\right\} \tag{4-41}$$

The more important mechanism of the two Bhabha processes considered here is loss due to bremsstrahlung ($e^+e^- \rightarrow e^+e^-\gamma$) of a photon, which can change the energy of a beam particle sufficiently to put it outside the energy acceptance of the accelerator. An excellent approximation for the cross section to lose a particle from beam i due to bremsstrahlung is [Altarelli and Buccella, 1964]

$$\sigma_{\text{brems } i} \approx \frac{16\alpha r_e^2}{3}\left[\left(\ln\frac{E_{\text{c.m.}}^2}{m_e^2}-\frac{1}{2}\right)\left(\ln\frac{E_i}{k_{\min i}}-\frac{5}{8}\right)+\frac{1}{2}\left(\ln\frac{E_i}{k_{\min i}}\right)^2-\frac{3}{8}-\frac{\pi^2}{6}\right] \quad (4\text{-}42)$$

In this expression, $k_{\min i}$ is the minimum energy of a radiated photon that causes loss of a particle from beam i. Thus, $k_{\min i}/E_i$ can be taken as the fractional energy aperture of the machine for beam i. This cross section depends slowly on the energy aperture and on $E_{\text{c.m.}}$.

Table 4-29 shows the bremsstrahlung beam loss cross section for PEP-II calculated according to Eq. 4-42. The fractional energy aperture is limited by the transverse aperture rather than by the RF voltage—we have used a value corresponding to ten times the rms energy spread of the beam.

We note that the large circumference of the PEP-II rings (2200 m) helps to produce a comfortably large luminosity lifetime from this source. Even if future upgrades result in a higher luminosity, we do not have a problem. For example, suppose we anticipate a luminosity of 1×10^{34} cm^{-2} s^{-1}. As a "worst case," suppose further that this gain is achieved at the same beam currents as in our nominal design, either by reaching higher tune shifts or by focusing more strongly. In this case, the luminosity lifetime is inversely proportional to the luminosity, so 12.6 hours at 3×10^{33} cm^{-2} s^{-1} becomes 3.8 hours at 1×10^{34} cm^{-2} s^{-1}. This would still be acceptable, although it would then be comparable to the beam-gas luminosity decay rate.

Another loss mechanism, typically not as important as the bremsstrahlung considered above, is the loss due to Bhabha ($e^+e^- \rightarrow e^+e^-$) scattering at sufficiently large angles to escape the acceptance of the machine. To a good approximation for the small angles and high energies that we consider, the cross section to lose a particle from beam i is

$$\sigma_{\text{Bhabha } i} \approx \frac{8\pi\alpha^2}{E_{\text{c.m.}}^2}\frac{E_j}{E_i}\left(\frac{1}{\theta_{\min x;i}^2}+\frac{1}{\theta_{\min y;i}^2}\right) \quad (4\text{-}43)$$

Table 4-29. Bremsstrahlung luminosity lifetime calculation.

Parameter	Symbol	High-energy ring	Low-energy ring
Fractional energy aperture	f_E	0.0061	0.0081
Min. energy in brems. integral [MeV]	$k_{\min}$	55.1	25.1
Brems. cross section for particle loss [cm^2]	$\sigma_{e^+e^-\gamma}$	3.0×10^{-25}	2.8×10^{-25}
Bremsstrahlung beam lifetime [hr]	$\tau_{\text{Br } i}$	14.8	34.4
Bremsstrahlung luminosity lifetime [hr]	τ_{Br}	12.6	

where $\theta_{\min x,y;i}$ is the minimum horizontal or vertical scattering angle in the laboratory frame leading to particle loss, and $j = (-,+)$. Cross sections in units of GeV^{-2} may be converted to cm^2 by multiplying by 3.89×10^{-28} GeV^2 cm^2.

Table 4-30 summarizes the calculation for the PEP-II design. For the minimum angles, we have made our usual assumption that the limiting aperture is 10σ (using the uncoupled horizontal and the fully coupled vertical beam sizes). Because the Bhabha cross section to lose a beam particle is substantially smaller than the cross section in our earlier bremsstrahlung loss example, this is not a significant lifetime consideration.

We conclude that the luminosity lifetime from $e^+e^- \rightarrow e^+e^-$ and $e^+e^- \rightarrow e^+e^-\gamma$ will not be a significant limitation for PEP-II at a luminosity of $\mathcal{L} = 3 \times 10^{33}$ cm^{-2} s^{-1}. Even at a luminosity of 1×10^{34} cm^{-2} s^{-1}, the large circumference (and hence large number of particles per unit of beam current) of the PEP-II rings ensures that these sources of beam loss will not seriously degrade the lifetime.

4.3.1.6 Higher-Order-Mode Losses. A complete specification of the thermal loading in the vacuum chamber must take into account the localized heating of beamline components due to the absorption of power generated by the beam in the form of HOM losses. We estimate the HOM power as

$$P_{\mathrm{HOM}} = 1.6 \times 10^{-10} N_b I k_\ell \ [\mathrm{kW}] \tag{4-44}$$

where N_b is the number of particles per bunch, I (in A) is the total current, and k_ℓ (in V/pC) is the loss factor for the ring due to its impedance. For the PEP-II design parameters, the HOM power in the HER is given by [Heifets, 1990a]

$$P_{\mathrm{HOM}} = 4.3\, k_\ell \ [\mathrm{kW}] \tag{4-45}$$

The equivalent value for the LER is

$$P_{\mathrm{HOM}} = 20\, k_\ell \ [\mathrm{kW}] \tag{4-46}$$

Table 4-30. Bhabha luminosity lifetime calculation.

Parameter	Symbol	High-energy ring	Low-energy ring
Minimum angle in Bhabha integral [rad]	$\theta_{\min x}$	3.17×10^{-3}	4.22×10^{-3}
Minimum angle in Bhabha integral [rad]	$\theta_{\min y}$	1.12×10^{-2}	1.49×10^{-2}
Bhabha cross section for beam loss [cm^2]	$\sigma_{e^+e^-}$	1.73×10^{-28}	8.16×10^{-28}
Bhabha beam lifetime [hr]	$\tau_{\mathrm{Bh}\,i}$	26000	12000
Bhabha luminosity lifetime [hr]	τ_{Bh}	10064	

The loss factor is defined as

$$k_\ell = \frac{1}{\pi}\int_0^\infty Z(\omega)\, e^{-(\omega\sigma_\ell/c)^2} d\omega \tag{4-47}$$

Based on the impedance values estimated here, the total loss factor of the LER with 10 RF cavities is k_ℓ = 11.2 V/pC. Of this, the RF cavities give 5.15 V/pC, the ring components give 3.25 V/pC, and the resistive wall gives 2.8 V/pC.

The HOM power deposition in the LER is then found from Eq. 4-46 to be P = 225 kW. For the HER there are 10 additional RF cavities that contribute an additional loss factor of 5.15 V/pC. The HOM power for the HER is then P = 70 kW. To be conservative, we double these $P_{\rm HOM}$ values in determining RF parameters, that is, we use $P_{\rm HOM}$ = 150 kW for the HER and $P_{\rm HOM}$ = 450 kW in the LER. The total HOM loss in the IR from both beams is P = 1.2 kW. This is very small compared with the power deposited by the synchrotron radiation (about 75 kW).

We estimate the ohmic losses (power deposition per unit length) from a beam with k_B bunches in the ring as

$$\frac{dP}{dz} = k_B f_0 \left(\frac{e^2}{2\pi b}\right)\frac{N_b^2}{\sigma_\ell^{3/2}}\sqrt{\frac{2}{\sigma Z_0}}\,\Gamma(3/4) \tag{4-48}$$

For the beryllium pipe at the IP, $\sigma = 3.1 \times 10^5\ \Omega^{-1}\ \mathrm{cm}^{-1}$ and b = 2.5 cm. For the two beams with parameters k_B = 1658, f_0 = 136 kHz, $N_b = 2.75 \times 10^{10}$ (HER) and 5.91×10^{10} (LER), we find dP/dz = 0.70 W/cm.

The estimate shows also that the HOM power will be absorbed mostly outside of the interaction region. The wakefields generated outside of, but absorbed within, the IR deposit very little energy because the average loss factor per unit length outside of the IR (excluding RF cavities) is much smaller than that of the IR. This contribution may be dominated by the wakefields generated at the crotches far away from the IP.

Energy deposition could be enhanced substantially if there were trapped modes in the IR, provided their wavelengths were multiples of the bunch spacing. We have tried to find the trapped modes in a structure that reproduces the real IR structure within ±25 cm from the IP and then is continued with straight pipes, using the code MAFIA. We failed to find any trapped modes [Ko, 1990]. This is not surprising in an open structure such as the PEP-II IR.

4.3.1.7 Ion Clearing. The trapping of positively charged ions produced by collisions between electrons of the beam and background gas molecules has degraded the performance of many electron storage rings. The production rate for the total ring is 1.3×10^9 ions per turn at an average pressure of 5 nTorr. The linear theory of ion trapping is quite simple. When an electron beam bunch passes near an ion, the ion experiences a restoring force toward the beam axis. This force results in a change in the transverse velocity of the ion. Between bunch passages, the transverse velocity produces a change in the transverse position of the ion. This pattern is repeated for each passage of an electron bunch.

To estimate the ion motion, it is useful to consider [Villevald, 1993] the transverse charge density of the electron beam as a Gaussian profile with rms width and height σ_x and σ_y, respectively. The equation of vertical motion for an ion in the electron bunch may be written as

$$\ddot{y} + \hat{\Omega}_y^2 \, y = 0 \tag{4-49}$$

where

$$\frac{\hat{\Omega}_y^2}{c^2} = \frac{2\hat{I}}{I_p A \sigma_y (\sigma_x + \sigma_y)} \tag{4-50}$$

with $\hat{I}$ the peak current of the bunch, c the speed of light, $I_p = m_p c^3/e = 3.1 \times 10^7$ A the Budker current of a proton, and A the ion mass number. The bunch cross section varies around the ring, but, for purposes of estimation, we can take $\sigma_x = 0.1$ cm, $\sigma_y = 0.02$ cm, an ion mass of 20, and a peak current 130 A. These parameters give $\hat{\Omega}_y = 4 \times 10^8$ rad/s. The bunch length τ and the bunch spacing Δt are 30 ps and 4.2 ns, respectively. Since both the quantities $\hat{\Omega}_y \tau$ and $\hat{\Omega}_y^2 \tau \, \Delta t$ are much less than one radian, we can neglect the bunch structure of the beam and describe the ion motion as occurring in the potential well of a continuous electron beam. Figure 4-83 shows the depth of the potential well for a

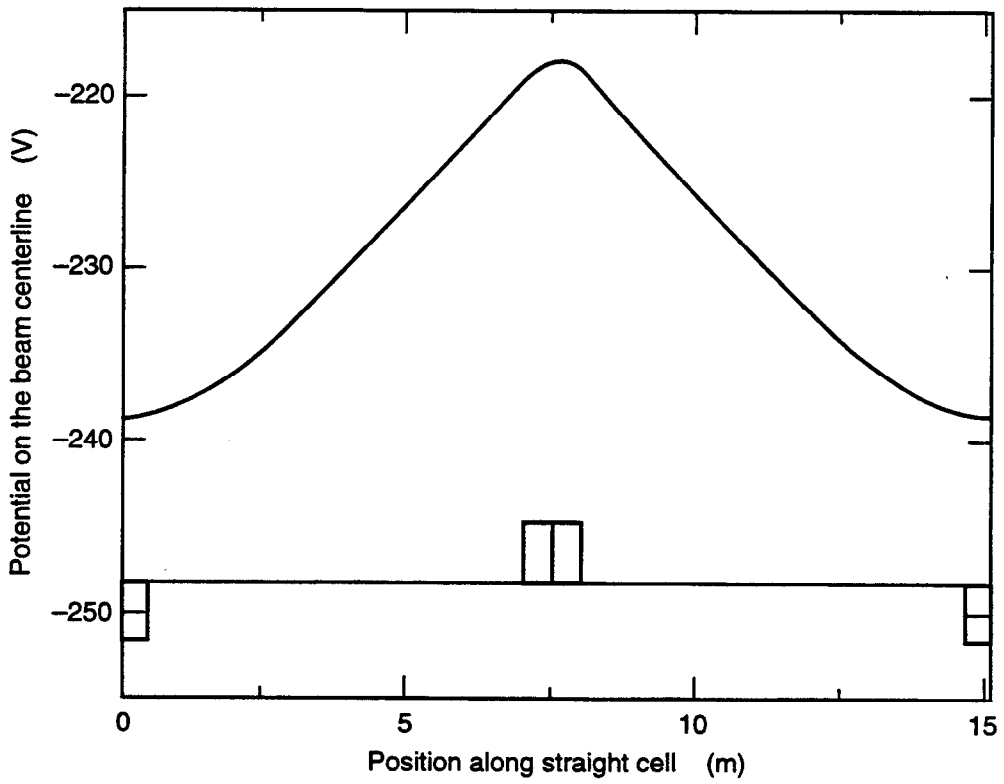

Fig. 4-83. Depth of potential well for a singly charged ion in the HER straight section.

singly charged ion along the straight section lattice cell. The average transverse ion motion can be obtained from Eq. 4-49 by replacing the peak current in Eq. 4-50 by the average current $I = 0.99$ A. The ion effectively sees a continuous electron beam and oscillates with an average frequency of $\Omega_y = 3.3 \times 10^7$ rad/s. The same analysis applied to the horizontal ion motion gives $\Omega_x = 1.5 \times 10^7$ rad/s. For a continuous bunched beam in the HER, ions will be trapped unless measures are taken to remove them.

The best known approach to avoiding ion trapping is to leave a gap in the electron bunch train. This gap need be only a few percent of the total ring circumference, so that only a small increase in the single-bunch current is necessary to achieve the same luminosity obtained for the continuous bunch train. An ion will be linearly unstable whenever the gap satisfies the following condition:

$$\left|\cos\left[\Omega_{x,y}\left(T_0-\Delta T\right)\right]-\frac{\Omega_{x,y}\,\Delta T}{2}\sin\left[\Omega_{x,y}\left(T_0-\Delta T\right)\right]\right|>1 \qquad (4\text{-}51)$$

where T_0 is the revolution period and ΔT is the gap length. For $T_0 = 7.3$ μs, the phase advance of ion oscillation during the passage of the bunch train is given by $\Omega_{x,y}(T_0 - \Delta T) \approx 170$ rad and stability is sensitive to small parameter variations. For a particular combination of current, beam cross section, and ion mass, the ion would perform nearly an exact number of half-integer oscillations during the passage of the bunch train. This would result in violation of the instability condition, Eq. 4-51. Therefore there will be locations along the ring where ions can be trapped (see Fig. 4-84). The typical width of each of these zones is of the order of a few centimeters. These locations shift along the beam orbit as the current decays and/or the beam cross section changes. The ratio of the total length of stability zones to the ring circumference has been calculated as a function of gap length from Eq. 4-51 and is plotted in Fig. 4-85, which shows the percentage of ions trapped in stability zones as a function of gap length for various ion masses (for the average current in the HER of 0.99 A). The design length of the HER gap is 88 bunches or 5% of the ring circumference. This choice gives a total length of the transverse stability zones of the order of 18% of the circumference for a typical ion mass number of $A = 20$; a longer gap doesn't change this percentage drastically.

The majority of the ions are expected to leave the stable zones due to longitudinal motion caused by variation of the depth of the beam potential well with azimuth (due to variation of the transverse beam sizes σ_x and σ_y, as shown in Fig. 4-83) and, for nonzero transverse amplitude, due to the cross-field force. A time of the order of 2–3 revolution periods is enough for the ion to drift from the stability zone and become transversely unstable.

A worst case would occur when an ion is both transversely and longitudinally stable and the zone of stability coincides with the minimum of the beam potential well, that is, when ions are generated at the QD location (see Fig. 4-83). The typical width of the stability zone near the minimum of the beam potential well varies from $w = 18$ cm for hydrogen ($A = 2$) to $w = 85$ cm for carbon dioxide ($A = 44$). Ions will accumulate in these zones from one turn to another. The frequencies of the trapped ions should be within the frequency range

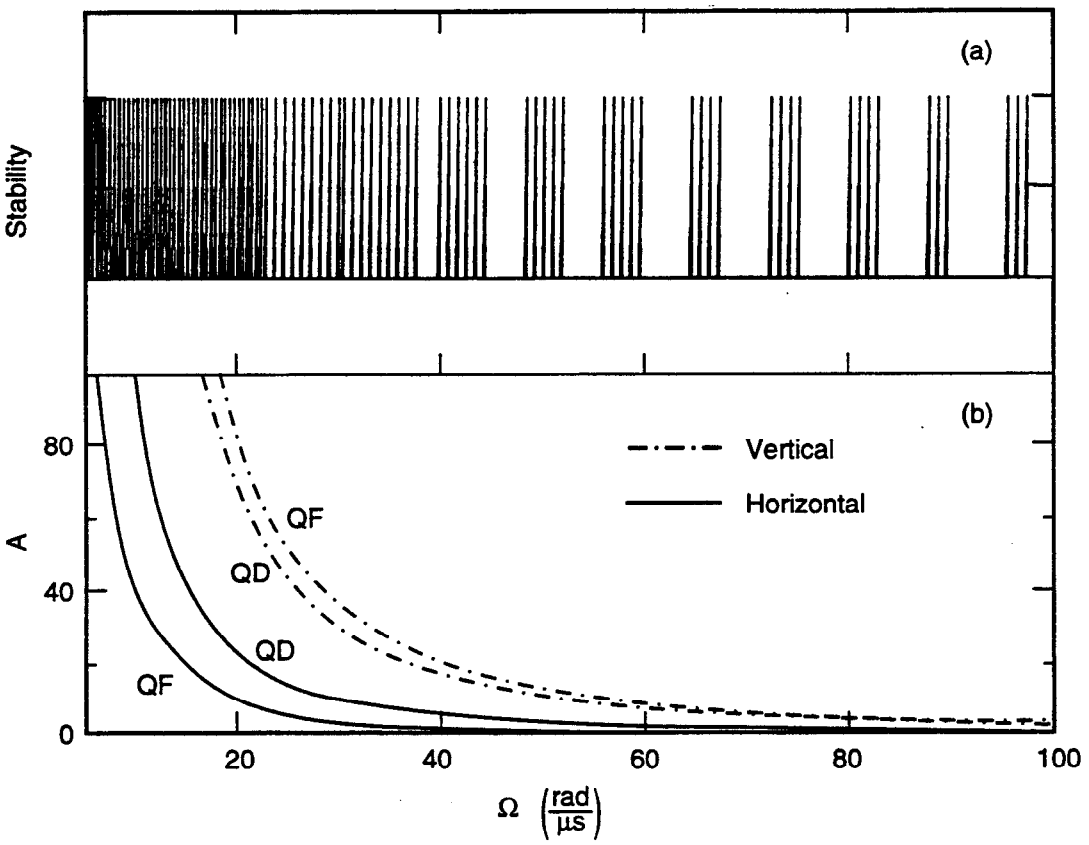

Fig. 4-84. (a) Stable zones for ion trapping, plotted as a function of ion frequency. (b) Frequencies for different masses at QF and QD locations.

$$\frac{\Delta\Omega_{x,y}}{\Omega_{x,y}} = \frac{2}{\Omega_{x,y}\,T_0}\cot^{-1}\left(\frac{\Omega_{x,y}\,\Delta T}{2}\right) \tag{4-52}$$

For heavy ions, A ≈ 44, and a gap length $\Delta T/\bar{T} = 0.05$, we find $\Omega\Delta T \gg 1$ and $\Delta\Omega/\Omega$ very small, about 3×10^{-3}.

The number of accumulated ions in a stable zone is limited by two effects that change the ion frequency: the space charge of the trapped ions and the amplitude dependence of the frequency Ω. The space-charge effect produces a frequency shift Eq. 4-52 when the ion linear density is

$$\Delta N_i^{st} = 2\,\frac{N_e}{cT_0}\,\frac{\Delta\Omega_y}{\Omega_y} \tag{4-53}$$

where $N_e = 4.5 \times 10^{13}$ is the total number of electrons in the HER. Therefore, the number of ions trapped in this stable zone is $w\Delta N_i^{st}$ ions. The total number of the stability zones coinciding with the bottom of the beam potential well cannot exceed the number of lattice cells in the HER: $n_{cell} = 144$, so the maximum number of trapped ions is

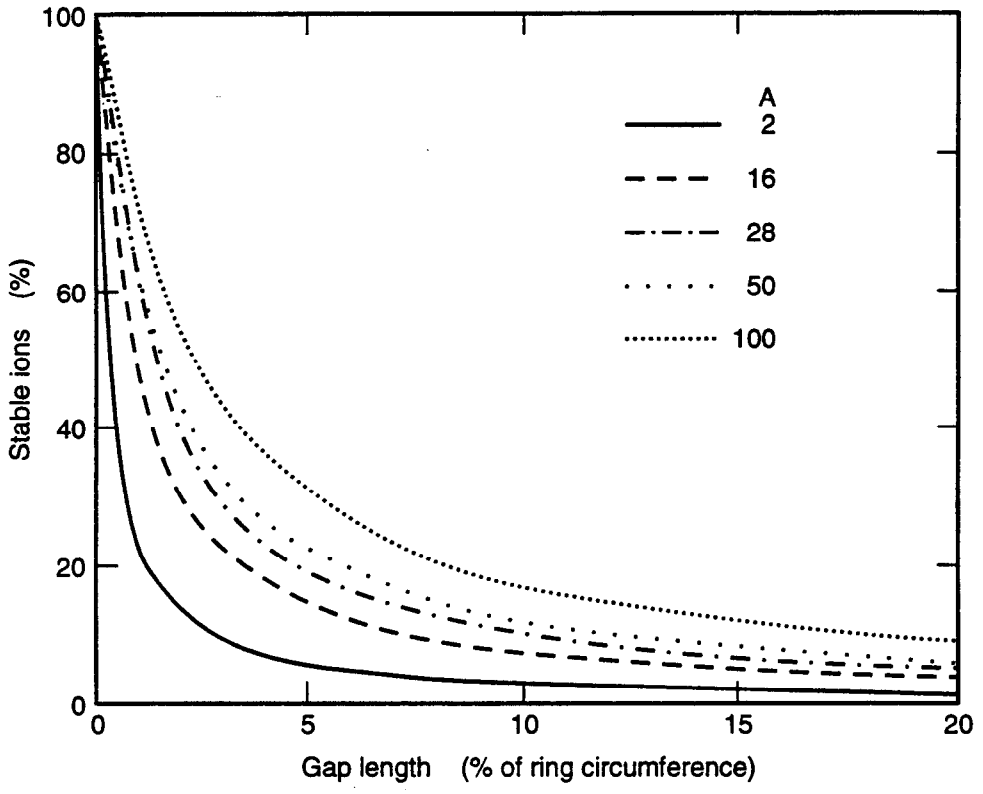

Fig. 4-85. Percentage of circumference that gives stable ion motion as a function of the length of the ion-clearing gap.

$$N_i^{st} = \Delta N_i^{st}\, wn_{\text{cell}} \tag{4-54}$$

For hydrogen $N_i^{st} = 1.3 \times 10^8$ and for carbon dioxide $N_i^{st} = 1.3 \times 10^{10}$.

The accumulation of these ions is a relatively slow process, taking 10^3–10^4 turns. During this time, the number of trapped ions will also decrease due to fluctuations of the beam current and transverse beam size. In reality, the number of trapped ions is also less than that given by Eq. 4-54 because the straight-section cells, dispersion-suppressor cells, and arc cells are not all identical. We see that the number of trapped hydrogen ions is much lower than the total number of ions produced during the revolution period of the HER, $N_i = 1.3 \times 10^9$. However, the number of trapped heavy ions ($A = 44$) is significant.

There is an additional reduction in the number of trapped ions due to the dependence of the ion frequency on ion amplitude a_y. For example,

$$\Omega_y = \Omega_y^0 \left[1 - \left(\frac{a_y}{4\sigma_{y,e}}\right)^2\right] \tag{4-55}$$

An amplitude $a_y/\sigma_{y,e} = 0.22$ corresponds to a frequency shift $\Delta\Omega/\Omega \approx 3 \times 10^{-3}$. Such a shift reduces the total number of stable ions by an order of magnitude, making their effect small compared with that of single-turn ions. The maximum betatron tune shift generated

by trapped heavy ions is

$$\Delta\nu_y^{st} = \frac{N_i^{st}}{2\pi}\frac{1}{\gamma}\frac{r_e\hat{\beta}_y}{\hat{\sigma}_y(\hat{\sigma}_y + \hat{\sigma}_x)} \tag{4-56}$$

For a beam current $I = 0.99$ A in the HER, $\hat{\beta}_y = 2500$ cm, $\gamma = 1.8 \times 10^4$ (the relativistic factor), and beam sizes at the QD locations of $\hat{\sigma}_x = 0.07$ cm, $\hat{\sigma}_y = 0.022$ cm, the tune shift is 0.04 and the betatron tune spread due to the trapped ions is of the order of $\delta\nu_y^{st} = 0.03$. In reality, the effect is even larger, because the distribution function of trapped ions is expected to be narrower than the distribution function of the electron beam (see Fig. 4-86) [Tavares, 1992], which increases the tune shift by a factor of two. However, only a small number of electrons, about 0.25%, experience a tune shift of this magnitude (which is still less than the tune shift given by the beam-beam interaction).

In considering the effects of unstable ions, it is convenient to divide them into two groups. The first group we refer to as "single-turn" ions, that is, ions accumulated during the passage of the previous bunch train. The total number of single-turn ions is

$$N_i = N_e\,\frac{T_0}{\tau_i} = 1.3 \times 10^9 \tag{4-57}$$

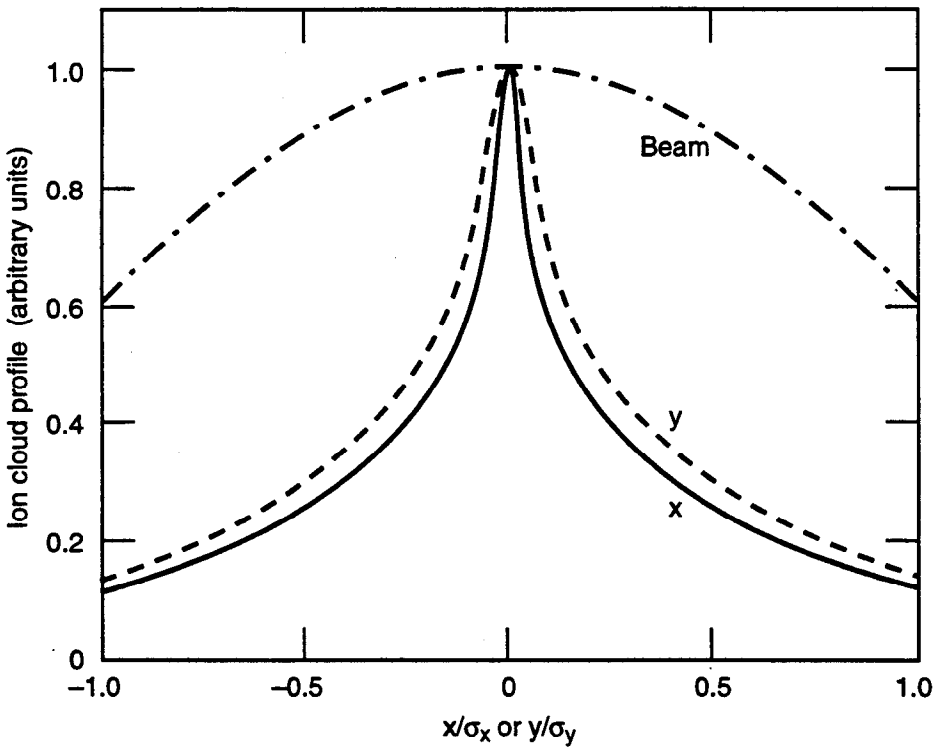

Fig. 4-86. Calculated distribution of trapped ions compared with beam dimensions.

where $\tau_i = 0.25$ s is the total ionization time. These ions cannot be removed by lumped clearing electrodes. Single-turn ions produce a betatron tune spread from bunch to bunch. Indeed, there are no single-turn ions at the head of the bunch train, whereas the number of single-turn ions for the last bunch of the train is given by Eq. 4-57. The bunch-to-bunch betatron tune spread is given by

$$\Delta\nu_y = \frac{N_i}{2\pi}\frac{1}{\gamma}\frac{r_e\langle\beta_y\rangle}{\sigma_y(\sigma_y+\sigma_x)} = 0.002 \tag{4-58}$$

for the HER current of $I = 0.99$ A and $\langle\beta_y\rangle = 1.5 \times 10^3$ cm the beta function averaged over the ring circumference. This tune spread is unavoidable even with clearing electrodes.

The second category of unstable ions involves "many-turn" ions, that is, ions generated and trapped during many previous turns. During the time of the gap passage, these ions reach large amplitudes, so we need to consider nonlinear theory in analyzing their behavior. Generally speaking, the amplitude dependence of the ion oscillation frequency may result in nonlinear resonances. The resonance condition is

$$k\Omega_{x,y} = n\omega_0 \tag{4-59}$$

where ω_0 is the revolution frequency and k and n are integers. For $\Omega_{x,y} \approx 3 \times 10^7$ rad/s, $\omega_0 = 8.6 \times 10^5$ rad/s, and $k = 1$, the order of the resonance is $n \approx 35$. Resonances of such high order are suppressed strongly. Therefore, a linearly unstable ion remains unstable at large amplitudes. This statement has been confirmed by computer simulations in which it was shown that the betatron tune shift due to many-turn ions is

$$\Delta\hat{\nu}_y \approx \Delta\nu_y \frac{q}{1-q} \tag{4-60}$$

where $\Delta\nu_y$ is the tune shift due to single-turn ions, given by Eq. 4-58, and the parameter q is proportional to the atomic number A

$$q \equiv \frac{\sigma_x^2}{c^2\Delta T^2}\frac{A\pi m_p c^2}{eIZ_0} = 6.8 \times 10^{-4} A \tag{4-61}$$

with $I = 0.99$ A and $Z_0 = 377\ \Omega$ (the impedance of free space). The tune-shift value obtained from Eq. 4-60 is small in comparison with the shift due to single-turn ions for our design current.

The nonlinear field of the single-turn ion cloud results in a betatron tune spread given by

$$\delta\nu_y = \frac{\partial\nu_y}{\partial\varepsilon_y}\varepsilon_y = \frac{3\varepsilon_y}{32}\frac{e}{\gamma m_e c^2}\oint_C \beta_y^2(s)\frac{\partial^3 E_y}{\partial y^3}ds \tag{4-62}$$

With $\varepsilon_y = 1.93 \times 10^{-9}$ m·rad, E_y the electric field of the ion cloud (for the cloud of single-turn ions, $\partial^3 E_y/\partial y^3 = -2$ kV/cm), and C the ring circumference, we find $\delta\nu_y = -0.002$.

Figure 4-87 shows the horizontal and vertical "bunch-to-bunch" betatron tune spread induced by single-turn ions as a function of HER current. Although these ions cannot be removed by lumped clearing electrodes, this is not necessary because the tune spread from them is well below the corresponding value due to the beam-beam interaction.

The betatron tune spread due to the trapped heavy ions (Eq. 4-56) is of the order of the beam-beam tune shift. Hence, ion clearing might be necessary near the horizontally defocusing quadrupoles in the arcs and straight sections.

A closely related possible problem in PEP-II is that of cross-talk between the DIPs and the beam, a phenomenon observed at CESR. The effect at CESR is believed to be related to the penetration of the electrostatic field through the slots of the screen [Sagan and Welch, 1992]. Such an effect scales with the slot width w and the thickness of the screen as $w^2 e^{-\pi d/w}$. Simulations with POISSON (see Fig. 4-88) show that, for PEP-II parameters, the field at the beam is reduced to 0.012 V/cm—a negligible amount—with 5.5 kV on the DIPs.

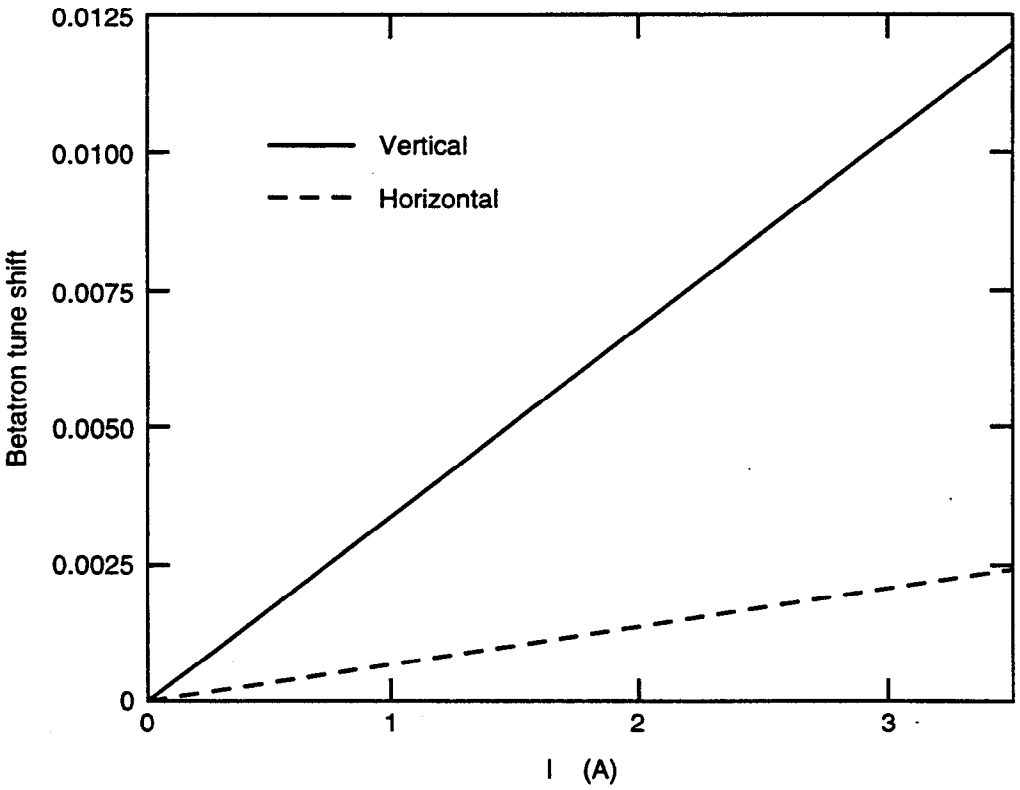

Fig. 4-87. Betatron tune spread due to trapped ions.

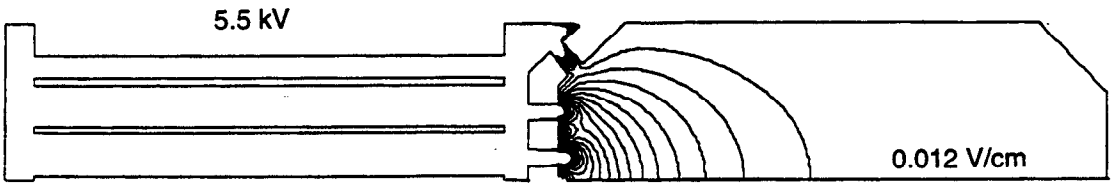

Fig. 4-88. Calculated electric field in beam chamber due to high-voltage on DIPs. A voltage of 5.5 kV in the pump chamber produces an electric field of only 0.012 V/cm at the beam location.

4.3.2 Coupled-Bunch Instabilities

As mentioned earlier, wakefields in high-Q resonant structures in a storage ring cause different beam bunches to interact. In general, such high-Q resonances result from the HOMs of the RF cavities. For certain values of relative phase between bunches, the coupled-bunch motion can grow and become unstable, leading to beam loss. In addition to the relative phase between bunches, the instabilities are characterized by their motion in longitudinal (synchrotron) phase space. Longitudinally, the $a = 0$ mode (corresponding to no motion) cannot be unstable, so the lowest longitudinal instabilities are characterized by $a = 1$ (dipole) synchrotron motion. In the *transverse* case, the $a = 0$ motion can also become unstable (referred to as "rigid-dipole" motion).

In the case of PEP-II, we require a relatively large number of RF cells, both to generate the voltage needed to produce the short bunches and to replace the beam power lost to synchrotron radiation each turn. Combined with the required very high average beam currents, the substantial RF system can produce extremely rapid growth of coupled-bunch instabilities. In the cases studied here, the most severe growth comes from the lowest modes, that is, $a = 1$ longitudinally and $a = 0$ transversely.

We have estimated the growth rates for both longitudinal and transverse instabilities for typical PEP-II parameters, that is, 1746 bunches having a total current of 0.99 A (HER) or 2.14 A (LER). This bunch number, which ignores the gap for clearing ions, is necessary for calculations performed with ZAP in the frequency domain.

Two different cases, based on the cavity design described in Section 5.5, were studied:

Case A: Undamped cavities; 20 cells (HER) or 10 cells (LER)

Case B: As in A, but with HOMs damped to $Q = 70$; 20 cells (HER) or 10 cells (LER)

In Case A, we examined the behavior of a standard PEP-II cavity with no HOM damping. This cavity has a high shunt impedance for the fundamental while having reasonable values for the HOMs. Case B represents what happens when the higher-order RF modes of the single-cell system are heavily de-Qed by external means, such as the waveguides described in Section 5.5.

Predictions of longitudinal growth times (for the fastest-growing mode) for both RF scenarios considered are summarized in Tables 4-31 and 4-32. The undamped cavity

Table 4-31. Longitudinal coupled-bunch growth times for the PEP-II HER (9 GeV; τ_E = 18.4 ms) at a beam current of 0.99 A.

(A) Undamped	
$\tau_{a=1}$	0.06 ms
$\tau_{a=2}$	2.0 ms
(B) Damped to Q = 70	
$\tau_{a=1}$	7.7 ms
$\tau_{a=2}$	363 ms

(Case A) gives a = 1 growth times below 0.1 ms. Substantial de-Qing (Case B) does help slow down the growth considerably, to times on the order of 8 ms. Note that the feedback system power required to counteract these instabilities will scale as the square of the growth rate, so the change associated with damping the cavity HOMs is very significant.

Although not shown in Tables 4-31 and 4-32, we have also observed that the fundamental mode of the RF system is capable of causing instability for selected coupled-bunch normal modes. This problem is handled via feedback on the cavity itself, as described in Sections 5.5 and 5.6. Transverse results, summarized in Tables 4-33 and 4-34, are similar to those for the longitudinal case. Here, too, we find for Case A that the two lowest synchrotron modes, a = 0 and a = 1, have growth times much shorter than the radiation damping time. We again note the benefits of substantial de-Qing (Case B) in slowing down the growth rates to more manageable levels. For Case A, it is the RF HOMs that dominate the predicted instability growth times for both a = 0 and a = 1

Table 4-32. Longitudinal coupled-bunch growth times for the PEP-II LER (3.1 GeV; τ_E = 19.8 ms) at a beam current of 2.14 A.

(A) Undamped	
$\tau_{a=1}$	0.03 ms
$\tau_{a=2}$	1 ms
(B) Damped to Q = 70	
$\tau_{a=1}$	3.8 ms
$\tau_{a=2}$	180 ms

Table 4-33. Transverse coupled-bunch growth times for the PEP-II HER (9 GeV; τ_x = 37.2 ms) at a beam current of 0.99 A.

(A) Undamped	
$\tau_{a=0}$	0.20 ms
$\tau_{a=1}$	3.2 ms
(B) Damped to Q = 70	
$\tau_{a=0}$	4.5 ms
$\tau_{a=1}$	122.0 ms

synchrotron modes. For Case B, however, the growth of the instability is driven exclusively by the resistive-wall impedance for a = 0 modes (though the cavity HOMs still dominate the growth time for the a = 1 modes). Thus, the transverse feedback system power requirements are determined by the resistive-wall instability, as discussed in Section 5.6.2.

Although the feedback system design (Section 5.6) is based on detailed simulations of the multibunch growth rates, the simple estimates made here already justify the effort that has gone into designing an effective HOM damping system for the RF cavities (described in Section 5.5).

Table 4-34. Transverse coupled-bunch growth times for the PEP-II LER (3.1 GeV; τ_x = 40.3 ms) at a beam current of 2.14 A.

(A) Undamped	
$\tau_{a=0}$	0.1 ms
$\tau_{a=1}$	1.4 ms
(B) Damped to Q = 70	
$\tau_{a=0}$	1.1 ms
$\tau_{a=1}$	21.4 ms

4.3.3 Summary of Findings

Total beam current limitations in both rings will depend upon the ability of the vacuum system to maintain an acceptable pressure, about 5 nTorr, in the presence of 1–2 A of circulating beam. Neither bunch lengthening and widening due to the longitudinal microwave instability (which places a limit on the allowable broadband impedance), nor current limitations arising from the transverse mode-coupling instability are predicted to be constraints in the multibunch scenario considered here.

We have seen here that the performance of both high- and low-energy rings is likely to be limited mainly by coupled-bunch instabilities. Our choice of specially designed single-cell RF cavities helps to reduce the longitudinal HOM impedance by permitting the voltage to be produced with relatively few cells and by permitting the cavity HOMs to be effectively damped. Feedback systems able to deal with the remaining growth have been designed; they are described in Section 5.6.

4.4 BEAM-BEAM ISSUES

As discussed in Chapter 3, the desire to achieve high luminosity leads one naturally to specify high currents and/or small beam sizes. These tend to make the beam-beam interaction stronger, which, in turn, may lead to beam blowup, coherent oscillations, or fast particle losses that could defeat the purpose of the initial specification.

If the beam-beam interaction is sufficiently weak, the beams behave as if there were no collisions, and the performance is controlled by the single-beam parameters of the two rings. This condition implies a relative simplicity in the operation of the collider, because the two beams are effectively decoupled. The price one must pay for this simplicity is that, in order to achieve a specified luminosity, the weakness of the beam-beam interaction must be compensated by using large beam currents distributed over many bunches, or over few bunches with a large beam emittance. Either of these approaches can become a problem for other aspects of the design, such as the vacuum system or RF system, and can also lead to various kinds of beam instabilities.

If the beam-beam interaction is significant, the dynamical beam parameters generally deviate from their nominal values. A strong beam-beam interaction naturally tends to imply a high luminosity, but it entails the potential for the problems mentioned above. In addition, the operation becomes relatively more complicated because the two beams are effectively coupled.

Obviously, the desired luminosity performance of the collider implies specifications on the dynamical quantities. The nominal quantities, on the other hand, imply specifications on the individual rings. If the beam-beam dynamics were well understood, it would be possible to translate specifications from dynamical to nominal quantities, and then to proceed to the design of the two rings individually. Unfortunately, our understanding is incomplete. This is particularly true for asymmetric colliders, which involve the additional complication of having two separate rings. Furthermore, all beam-beam simulation tools in existence take nominal parameters as input and produce dynamical quantities as output. Therefore, the understanding obtained from beam-beam

4.3.3 Summary of Findings

Total beam current limitations in both rings will depend upon the ability of the vacuum system to maintain an acceptable pressure, about 5 nTorr, in the presence of 1–2 A of circulating beam. Neither bunch lengthening and widening due to the longitudinal microwave instability (which places a limit on the allowable broadband impedance), nor current limitations arising from the transverse mode-coupling instability are predicted to be constraints in the multibunch scenario considered here.

We have seen here that the performance of both high- and low-energy rings is likely to be limited mainly by coupled-bunch instabilities. Our choice of specially designed single-cell RF cavities helps to reduce the longitudinal HOM impedance by permitting the voltage to be produced with relatively few cells and by permitting the cavity HOMs to be effectively damped. Feedback systems able to deal with the remaining growth have been designed; they are described in Section 5.6.

4.4 BEAM-BEAM ISSUES

As discussed in Chapter 3, the desire to achieve high luminosity leads one naturally to specify high currents and/or small beam sizes. These tend to make the beam-beam interaction stronger, which, in turn, may lead to beam blowup, coherent oscillations, or fast particle losses that could defeat the purpose of the initial specification.

If the beam-beam interaction is sufficiently weak, the beams behave as if there were no collisions, and the performance is controlled by the single-beam parameters of the two rings. This condition implies a relative simplicity in the operation of the collider, because the two beams are effectively decoupled. The price one must pay for this simplicity is that, in order to achieve a specified luminosity, the weakness of the beam-beam interaction must be compensated by using large beam currents distributed over many bunches, or over few bunches with a large beam emittance. Either of these approaches can become a problem for other aspects of the design, such as the vacuum system or RF system, and can also lead to various kinds of beam instabilities.

If the beam-beam interaction is significant, the dynamical beam parameters generally deviate from their nominal values. A strong beam-beam interaction naturally tends to imply a high luminosity, but it entails the potential for the problems mentioned above. In addition, the operation becomes relatively more complicated because the two beams are effectively coupled.

Obviously, the desired luminosity performance of the collider implies specifications on the dynamical quantities. The nominal quantities, on the other hand, imply specifications on the individual rings. If the beam-beam dynamics were well understood, it would be possible to translate specifications from dynamical to nominal quantities, and then to proceed to the design of the two rings individually. Unfortunately, our understanding is incomplete. This is particularly true for asymmetric colliders, which involve the additional complication of having two separate rings. Furthermore, all beam-beam simulation tools in existence take nominal parameters as input and produce dynamical quantities as output. Therefore, the understanding obtained from beam-beam

simulations proceeds, in some sense, "in reverse." In practice, therefore, the only way to arrive at a specification of nominal beam parameters is to proceed by iterations.

The basic strategy we adopt for PEP-II is to choose values for the nominal quantities (including the beam-beam parameters ξ_0) to achieve a certain (nominal) luminosity, and then to verify by simulations that the dynamical behavior is close to nominal. If the dynamical results are substantially different from the nominal expectations, we change the nominal parameters and try again until an acceptable solution is found.

As mentioned earlier in this report, the key figure-of-merit for PEP-II (or any other particle "factory") is high integrated luminosity. This implies that a proper design must have good operational reliability and high average luminosity. This last requirement implies high peak luminosity, long beam lifetime, and the capability for rapid injection; the first two requirements are almost always in conflict.

The bulk of the beam-beam studies carried out to date, which are summarized here, have set a priority on demonstrating the feasibility of attaining or exceeding a short-time-average luminosity of 3×10^{33} cm^{-2} s^{-1}. In this section, we present one set of parameters that strikes a balance between the conflicting requirements mentioned above. This solution is not necessarily unique or optimal, but it is an existence proof that such a value for the luminosity is an achievable goal. The short-time-average luminosity is determined by the dynamics of the beam core, while the beam lifetime is determined by the long-time dynamics of the tails of the beam. Since high peak luminosity is a necessary (but not sufficient) condition for good average luminosity, we have mainly focused our efforts on the dynamics of the beam core. Preliminary results from studies of beam-tail distributions (see Section 4.4.5) indicate acceptable beam lifetimes.

A complete set of beam-beam studies would need to address a large number of issues, such as those arising from the energy and lattice asymmetries, multibunch coherent effects, magnet nonlinearities, multiple parasitic collisions, injection transients, and beam lifetime calculations. Such a task is beyond the reach of any single tool available today, so one must necessarily resort to various approximations; the studies summarized here are no exception. For this reason we cannot, in general, interpret our results quantitatively. However, we do believe that qualitative comparisons between results for different parameter values provide us with valid guidance with regard to desirable or undesirable changes in these parameters. This philosophy underlies the interpretation of our beam-beam studies, particularly multiparticle simulations.

In summary, although substantial work remains to be done, we are confident that the solution we propose here will lead to a productive *B* factory, and we further expect that improved solutions can be found by modest modifications of various parameters.

4.4.1 Nominal and Dynamical Beam Quantities

In the absence of the beam-beam interaction, the beam parameters are determined by the lattice, the energy, and the RF parameters of each ring. In particular, this is true of the emittances and therefore the beam sizes at the interaction point (IP). From these one can compute the beam-beam parameters and the resultant luminosity in the limit that the beam-beam interaction does not change them; the quantities calculated in this limit are referred to here as *nominal* and are indicated by a subscript 0. As an example of our

notation, the nominal vertical beam size at the IP, $\sigma^*_{0y,+}$ and beam-beam parameter $\xi_{0y,+}$ of the positron beam, and the nominal luminosity $\mathcal{L}_0$ are given by

$$\sigma^*_{0y,+} = \sqrt{\varepsilon_{0y,+}\beta^*_{y,+}} \tag{4-63a}$$

$$\xi_{0y,+} = \frac{r_0 N_- \beta^*_{y,+}}{2\pi\gamma_+\sigma^*_{0y,-}\left(\sigma^*_{0x,-} + \sigma^*_{0y,-}\right)} \tag{4-63b}$$

$$\mathcal{L}_0 = \frac{N_+ N_- f_c}{2\pi\sqrt{\left(\sigma^{*2}_{0x,+} + \sigma^{*2}_{0x,-}\right)\left(\sigma^{*2}_{0y,+} + \sigma^{*2}_{0y,-}\right)}} \tag{4-63c}$$

where $\beta^*_{y,+}$ and $\varepsilon_{0y,+}$ are the vertical beta function at the IP and the nominal emittance of the positron beam, the $N_\pm$ are the numbers of particles per bunch, r_0 is the classical electron radius, and f_c is the bunch collision frequency. We assume here that the bunches collide head-on, that they have elliptical Gaussian transverse profiles with common axes, and that they have lengths comparable to or smaller than their transverse beta functions. In this case, the so-called "hourglass" reduction effect is small [Furman, 1991a]. There are three more beam-beam parameters, whose expressions are obtained from the above by the replacements $x \leftrightarrow y$ and/or $+ \leftrightarrow -$. If the bunches are evenly spaced by a distance s_B, the bunch collision frequency is, in the relativistic limit, $f_c = c/s_B$, where c is the speed of light.

Once the beams are brought into collision, the emittances inevitably deviate from their nominal values and, as a result, so do all quantities involving the beam sizes, including the beam-beam tune shift and the luminosity. These are the *dynamical* quantities, denoted without the subscript 0; the dynamical quantities corresponding to those in Eqs. 4-63 above are given by

$$\sigma^*_{y,+} = \sqrt{\varepsilon_{y,+}\beta^*_{y,+}} \tag{4-64a}$$

$$\xi_{y,+} = \frac{r_0 N_- \beta^*_{y,+}}{2\pi\gamma_+\sigma^*_{y,-}\left(\sigma^*_{x,-} + \sigma^*_{y,-}\right)} \tag{4-64b}$$

$$\mathcal{L} = \frac{N_+ N_- f_c}{2\pi\sqrt{\left(\sigma^{*2}_{x,+} + \sigma^{*2}_{x,-}\right)\left(\sigma^{*2}_{y,+} + \sigma^{*2}_{y,-}\right)}} \tag{4-64c}$$

In this discussion, we assume that the beam-beam interaction does not induce coherent oscillations or a relative displacement of the closed orbits at the IP. This is discussed in greater detail when we describe our simulation results in Section 4.4.4.

4.4.2 Transparency Symmetry

The fact that an asymmetric collider necessarily consists of two rings enlarges the beam dynamics parameter space considerably relative to a single-ring, symmetric collider. The bunches in the two rings see different RF systems, different lattice functions, and different magnetic fields. Even the simplest beam-beam dynamics study requires, at a minimum, the specification of the following quantities:

- Two values for the number of particles per bunch, $N_{\pm}$
- Six beam sizes (two transverse and one longitudinal for each beam)
- Four beta functions at the IP (one vertical and one horizontal for each beam)
- Six tunes
- Two sets of damping decrements

In general, the four beam-beam parameters are different, as can be seen from Eq. 4-63.

Because no asymmetric e^+e^- colliders exist at present, and because the consequences of the beam-beam interaction are not completely understood for intense beams, it has been argued [Garren, 1989; Chin, 1989, 1990] that a cautious approach would be to require that the beam dynamics of an asymmetric collider resemble as closely as possible the dynamics of a symmetric one. In this way, the design can draw upon the valuable experience gained from single-ring colliders. This is the so-called "transparency symmetry" condition; it is reached by imposing constraints on the parameters of the two rings according to the following:

(i) Pairwise equality of nominal beam-beam parameters: $\xi_{0x,+} = \xi_{0x,-}$ and $\xi_{0y,+} = \xi_{0y,-}$

(ii) Pairwise equality of nominal beam sizes: $\sigma^*_{0x,+} = \sigma^*_{0x,-}$ and $\sigma^*_{0y,+} = \sigma^*_{0y,-}$

(iii) Equality of damping decrements of the two rings

(iv) Equality of the tune modulation amplitudes due to synchrotron oscillations: $(\sigma_\ell \nu_s/\beta^*_{x,y})_+ = (\sigma_\ell \nu_s/\beta^*_{x,y})_-$, with σ_ℓ the bunch length and ν_s the synchrotron tune

These conditions have been arrived at by a combination of analytic arguments and by trial and error in simulations. It has been shown that, in certain cases, the predicted performance is better when the above conditions are satisfied than when they are badly violated [Chin, 1989, 1990]. From the theoretical perspective, however, the status of this transparency symmetry is not completely settled: It has been argued, from general principles, that the *global* beam-beam limit (understood to mean maximum integrated luminosity at a fixed overall cost) in an asymmetric collider can only be reached under asymmetric conditions [Tennyson, 1990]. However, it is possible that this beam-beam limit can be achieved only at the price of relinquishing too much flexibility and therefore operational reliability, or of undesirably tight tolerances. Furthermore, it is not known at present how different the luminosity at the beam-beam limit would be compared with what could be achieved in a given transparent-symmetric design. On the other hand, by demanding that the dynamics of the two beams be identical, a single-particle Hamiltonian

analysis in the linear-lattice approximation leads to a more restrictive set of transparency conditions than those above [Krishnagopal and Siemann, 1990b]. This analysis implies that the tunes, emittances, beta functions, beam-beam parameters, and bunch lengths of the two beams must be pairwise equal. The only freedom left over is a trade-off between energy and bunch current such that $(N\gamma)_+ = (N\gamma)_-$.

In any case, the design of PEP-II must strike a compromise among competing requirements from different areas of the design. This compromise requires accommodating certain constraints, such as those arising from single-particle nonlinear dynamics, synchrotron radiation masking, etc., that affect an idealized optimization of the beam-beam interaction. As a result of this compromise, the present design of PEP-II satisfies exactly only conditions (i) and (ii) above. However, as will be discussed later in this section, we have also carried out studies in which condition (i) is violated [Eden and Furman, 1993a]. These studies show that the dynamics behaves smoothly as the nominal beam-beam parameters move away from equality. The PEP-II design allows enough flexibility to accommodate such a departure from condition (i), within a certain range, should further research indicate the need. For now, however, we have adopted the approximate transparency symmetry as a prudent starting point in the design.

An important practical implication of the constraints above is that they reduce considerably the parameter space and hence simplify the design. A mathematical advantage of transparency symmetry is that the luminosity can be very simply and conveniently expressed in terms of a single beam-beam parameter. First, we note that condition (ii) above implies that there is a single nominal beam-aspect ratio r,

$$\left(\frac{\sigma_{0y}^*}{\sigma_{0x}^*}\right)_+ = \left(\frac{\sigma_{0y}^*}{\sigma_{0x}^*}\right)_- \equiv r \tag{4-65}$$

and that the expression for the nominal luminosity simplifies to

$$\mathcal{L}_0 = \frac{N_+ N_- f_c}{4\pi\sigma_{0x}^*\sigma_{0y}^*} \tag{4-66}$$

By combining conditions (i) and (ii), we have [Garren, 1989; Chin, 1990; Furman, 1991b]

$$\frac{\beta_{x,-}^*}{\beta_{x,+}^*} = \frac{\beta_{y,-}^*}{\beta_{y,+}^*} = \frac{(EI)_-}{(EI)_+} \tag{4-67}$$

where I = total beam current (assuming no gaps). One also finds that there is a single beta-function ratio (rather than two) and a single nominal emittance ratio:

$$\frac{\beta_{y,+}^*}{\beta_{x,+}^*} = \frac{\beta_{y,-}^*}{\beta_{x,-}^*} \equiv r_\beta \quad \text{and} \quad \frac{\varepsilon_{0y,+}}{\varepsilon_{0x,+}} = \frac{\varepsilon_{0y,-}}{\varepsilon_{0x,-}} \equiv r_\varepsilon \tag{4-68}$$

so that the beam-size ratio becomes

$$r = \sqrt{r_\varepsilon r_\beta} \tag{4-69}$$

The nominal beam-beam tune shift parameters are related to r_β and r_ε by

$$\frac{\xi_{0y}}{\xi_{0x}} = \sqrt{\frac{r_\beta}{r_\varepsilon}} = \frac{r_\beta}{r} \tag{4-70}$$

and the nominal luminosity is

$$\mathcal{L}_0 = K(1+r)\xi_{0y}\left(\frac{EI}{\beta_y^*}\right)_{+,-} \tag{4-71}$$

where the subscript +,– means that the expression in parentheses can be taken from either beam, because of Eq. 4-67. The constant K is

$$\begin{aligned} K &= \frac{1}{2er_0mc^2} \\ &= 2.17\times10^{34}\ \left[\mathrm{cm^{-2}s^{-1}}\right]\cdot\left[\frac{\mathrm{cm}}{\mathrm{GeV\cdot A}}\right] \end{aligned} \tag{4-72}$$

where mc^2 is the rest energy of the electron and e is its charge. Therefore, if we express the energy E in GeV, the current I in A, and the beta function in cm, we obtain

$$\mathcal{L}_0 = 2.17\times10^{34}\,(1+r)\xi_{0y}\left(\frac{EI}{\beta_y^*}\right)_{+,-}\quad\left[\mathrm{cm^{-2}\ s^{-1}}\right] \tag{4-73}$$

Note that ξ_{0y} cannot be varied independently of the other parameters, since it is related to them through Eqs. 4-69 and 4-70. It is also worth commenting that Eq. 4-73 can be rewritten, if desired, in terms of horizontal, rather than vertical, parameters by making the replacements $y \rightarrow x$ and $r \rightarrow 1/r$.

In contrast, the nominal aspect ratio r, the beta function ratio r_β, and the nominal emittance ratio r_ε are free parameters, except that they are related by Eq. 4-69.

If, in addition to the transparency symmetry condition (i), we impose the extra requirement that *all four* beam-beam parameters should be equal, that is

$$\xi_{0x,+} = \xi_{0y,+} = \xi_{0x,-} = \xi_{0y,-} \equiv \xi_0$$

as we will in our simulations presented below, then one finds the additional equality $r = r_\beta = r_\varepsilon$ or, explicitly,

$$\frac{\sigma_{0y,+}^*}{\sigma_{0x,+}^*} = \frac{\sigma_{0y,-}^*}{\sigma_{0x,-}^*} = \frac{\beta_{y,+}^*}{\beta_{x,+}^*} = \frac{\beta_{y,-}^*}{\beta_{x,-}^*} = \frac{\varepsilon_{0y,+}}{\varepsilon_{0x,+}} = \frac{\varepsilon_{0y,-}}{\varepsilon_{0x,-}} = r \tag{4-74}$$

The formula for the luminosity reads the same as the previous case, Eq. 4-73, except that now the beam-beam parameter carries no index *y*.

4.4.3 Physics of the Simulation Codes

For our simulations, we employ two distinct codes (one by H. Yokoya and another, called "TRS," by Tennyson [1989]) that are similar, but not identical. Each of these codes represents a beam bunch by a collection of many (we have used up to 256) "superparticles." Initially, these superparticles have a Gaussian distribution in phase space. At the IP, the rms beam sizes σ_x and σ_y are calculated from the superparticle distribution at every turn. Although the shape of the distribution deviates from Gaussian as time progresses, for the purposes of computing the beam-beam kick, it is a good approximation (for the range of parameters of interest to us) to retain the Gaussian shape, albeit with time-dependent σ_x and σ_y. From these distributions, the beam-beam force on each superparticle of the opposing bunch is computed by means of the well-known expression for the transverse electric field in terms of the complex error function [Bassetti and Erskine, 1980]. Deviations from a Gaussian shape are monitored; if the dynamic distribution were to differ substantially from Gaussian, one would have reason to doubt the results, owing to the lack of self-consistency. The importance of allowing for, and consistently treating, non-Gaussian distributions has been emphasized [Krishnagopal and Siemann, 1991]. At present, it appears that such an extension implies a significant complication in the tracking codes and a major increase in the computer time needed. This work remains to be carried out in the future to confirm that, in this parameter regime, our present predictions are not significantly modified.

Each beam is transported through the rest of the machine by a linear matrix; that is, no lattice nonlinearities are considered. Synchrotron radiation and damping are included and are represented by localized kicks. The RF system is also represented by a localized kick. Typically, the beams are tracked for three to five damping times to verify that an equilibrium situation has been reached. (For the specific set of parameters studied here, we have verified that five damping times is long enough to yield stable results and that three damping times is often adequate.)

The electromagnetic fields produced by relativistic particles are Lorentz-contracted into a thin disk perpendicular to the direction of motion. As a consequence, the force on a single particle due to the opposing bunch is, to a good approximation, strictly transverse; longitudinal forces can be neglected. (Indeed, the integrated longitudinal force is *exactly* zero in the case when the beta function is constant during the collision.) What cannot be neglected, however, is the fact that the opposing bunch has a finite longitudinal extent.

Near the IP, the vertical beta function is small and the betatron phase of a particle changes rapidly. Consequently, the net force due to the opposing bunch (that is, the beam-beam interaction) is distributed over a wide range of betatron phase. Because most beam-beam limiting phenomena are resonant in nature, this feature, called phase averaging, is important and must be incorporated into beam-beam calculations and simulations [Krishnagopal and Siemann, 1990a].

Phase averaging thus emphasizes the importance of the longitudinal extent of the beam-beam interaction. A Hamiltonian analysis that includes this feature predicts resonance strengths that are smaller than those calculated by models in which the beam-beam interaction is approximated by a single kick (impulse approximation). This also implies that resonance overlap, and the stochastic motion that results from it, set in at higher currents than would be estimated in the impulse approximation.

In the simulation results presented here, we allow for phase averaging by dividing the bunch longitudinally into several slices. Typically, five slices are used, although spot-checks with nine slices have sometimes been made. Both codes distribute the slices evenly along the length of the bunch and symmetrically about its center. However, the slices farthest away from the center are located in different places in the two codes. In Yokoya's code, the outermost slices are located at a distance $s = \pm 2\sigma_\ell$ from the bunch center, regardless of the number of slices. In TRS, the corresponding outermost distance is $s = \pm[1+ (n-3)/12]\sigma_\ell$, where n is the total number of slices. Thus, the two codes have identical slicing algorithms only when 15 slices are used; for fewer slices, TRS code concentrates the slices closer to the center of the bunch than does Yokoya's code. As the bunches pass through each other during the collision, the beta functions seen by the different slices are different, since the slices collide at points away from the IP. In the neighborhood of the IP, we take the s-dependence of the beta functions to correspond to that of a drift.

Besides the distinctions discussed above, the codes also differ in technical details having to do with the way certain quantities are averaged from turn to turn in order to smooth out statistical fluctuations associated with the relatively small number of superparticles.

The lattice design described in Section 4.1 has head-on collisions at the IP, with magnetic separation of the beams. However, the beams go into their own vacuum pipes only after traveling about 3 m away from the IP; as a result, they experience several grazing collisions on their way into and out of the IP. There are four such "parasitic" crossings on either side of the IP. These parasitic crossings couple the dynamics of all bunches, so a completely faithful simulation of the PEP-II beam-beam dynamics would require 1658 bunches per ring, along with a gap equivalent to 88 bunches. Since this is an impractical requirement for any present-day simulation, we make two simplifying approximations: (i) We consider only the first parasitic crossing on either side of the IP and (ii) we use only one bunch per ring, which is "reused" (so that this bunch collides three times per turn—two parasitic crossings plus the main collision at the IP—with the same partner in the other beam).

The first approximation is quite reasonable, since, as discussed in more detail below, the effect of the first parasitic crossing overwhelms all the others. The second approximation rests on the sensible assumption that, in reality (or in a faithful simulation), the particle distributions are not expected to differ much from bunch to bunch, especially when the bunches interact at a distance, as is the case at the parasitic crossings.

Given the complicated process that is being simulated, it is natural to test the predictions of the simulation codes against known experimental results. As an example, we have studied the particular PEP configuration summarized in Table 4-35 with Yokoya's code. We find that the luminosity prediction agrees with the measured value to

Table 4-35. PEP parameters used in simulation comparison.[a]

Betatron tunes	
Horizontal	21.2962
Vertical	18.2049
Beta functions at IP	
Horizontal [m]	1.342
Vertical [m]	0.053
Dispersion at IP	
Horizontal [m]	0.00049
Emittances	
Horizontal [nm·rad]	99.6
Vertical [nm·rad]	3.96
Synchrotron tune	0.043
Beam current [mA]	18.85
Nominal beam-beam parameter, ξ_0	
Horizontal	0.04653
Vertical	0.04653
Luminosity	
Nominal [$cm^{-2}\,s^{-1}$]	5.07×10^{31}
Observed [$cm^{-2}\,s^{-1}$]	4.80×10^{31}
Simulation [$cm^{-2}\,s^{-1}$]	4.34×10^{31}

[a] Data from E. Bloom and M. Donald.

within 10%. In fact, the simulation result is actually slightly *pessimistic,* since it is 10% below the observed luminosity. We also predict from the simulations that there will be no saturation of the dynamic beam-beam tune-shift parameter ξ up to a beam current of 30 mA—again in agreement with experimental observations. Calculations for other PEP configurations yield more or less equivalent agreement with the observed luminosities.

We have also tested TRS for the case of PEP, for a different configuration from that above, including the effect of the parasitic crossings in the arcs. The comparison with experiment is summarized in Fig. 4-89. In this comparison, too, we find reasonable agreement with experiment. Again, we note that the code tends to underestimate the luminosity.

Insofar as the simulation results in both cases are consistent in trend with the actual PEP observations, we feel that the predictions derived from these codes are reasonable guides for the design of PEP-II. Implied in this statement is the assumption that there is

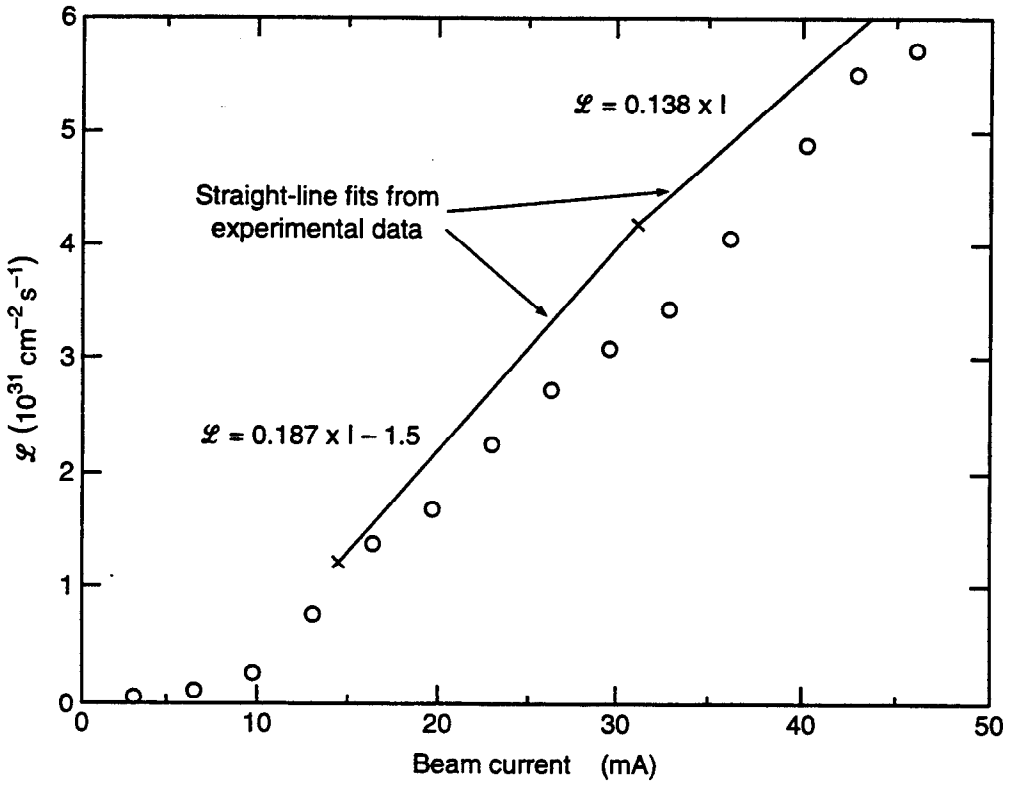

Fig. 4-89. Plot of observed luminosity at PEP and the simulation results from TRS. The tune values used in the simulation were slightly different from those used in the experiment itself; preliminary results show that the agreement improves when the tunes are the same.

no new physics that enters into the beam-beam interaction due to the asymmetric collisions. At the present time, we have every reason to believe that this assumption is valid.

4.4.4 Beam Dynamics Studies

The primary parameters that determine the strength of the beam-beam interaction are the four nominal beam-beam parameters, $\xi_{0x,\pm}$ and $\xi_{0y,\pm}$. If these are small enough, and if the working point of the ring is not too close to the integer tunes, ξ_0 is equal to the nominal tune spread induced by the beam-beam interaction. We adopt, as a starting point, the fully symmetric condition

$$\xi_{0x,+} = \xi_{0y,+} = \xi_{0x,-} = \xi_{0y,-} = 0.03 \tag{4-75}$$

The specification of $\xi_0 = 0.03$ is intended to be conservative, insofar as existing machines have already achieved substantially higher values of ξ_0 [Rice, 1989, 1990; Seeman, 1985]. As mentioned, this strategy of setting the beam-beam interaction to be

reasonably weak has the desirable consequence that the beam behavior will be close to nominal. This has the advantage of preserving operational flexibility, because the closer to nominal the beam-beam dynamics is, the more controllable is the machine performance. (Clearly, in an operating collider, the machine parameters will be adjusted to maximize the luminosity. The idea here is not to limit the machine performance, but rather to leave room for subsequent improvements.)

As mentioned earlier in this section, most of our beam-beam studies carried out to date have set a priority on demonstrating the feasibility of attaining or exceeding a dynamical luminosity value of 3×10^{33} cm^{-2} s^{-1}. We have studied first the short-time-average luminosity, which is determined by the dynamics of the beam core. This is studied quite effectively with "weak-strong" and "strong-strong" simulations involving a few hundred macroparticles per bunch tracked for several damping times, neglecting all lattice nonlinearities. Previous experiments and simulations for CESR [Jackson and Siemann, 1990] provide justification for the linear-lattice approximation since they show that magnet nonlinearities do not affect the core dynamics significantly once a good working point is adopted. On the other hand, the dynamics of the beam tails, relevant to beam lifetime, might be expected to be more sensitive to nonlinearities.

Specifically, the focus of our simulations has been to try to answer the following questions:

- Can a region of the tune plane be found such that the dynamics is close to nominal (that is, relatively small beam blowup)?
- Is the orbit separation between the two beams at the parasitic collisions large enough?
- Is the value of 0.03 for the beam-beam parameter conservative enough? How does the dynamics behave for $\xi = 0.05$?
- How do the beams behave during the first few damping times following injection?
- How do they behave after injection is complete but the beams are still separated by the injection orbit bump?
- How sensitive is the dynamics to changes in the asymmetry of the design?

Our basic strategy is first to choose nominal parameters and then to verify that the beam-beam interaction does not cause significant deviations from them. If the beam dynamics is substantially different from nominal (for example, if beam blowup is too large or beam lifetime too short), we change the nominal parameters and try again until an acceptable solution is found. In more detail, this strategy is divided into several steps:

(*i*) *Set nominal parameters.* Our design goal is a nominal luminosity of $\mathcal{L}_0 = 3 \times 10^{33}$ cm^{-2} s^{-1}. From this requirement and other considerations, a complete set of parameters for both rings can be derived (see Appendix A). For the purposes of this section, however, we show only an abbreviated list in Table 4-36. Further, because the collider design has evolved in parallel with the simulation study, some of the final parameters in Appendix A differ slightly from those in this section. The parameters indicated in Table 4-36, however, are the values used in the simulation study.

In Table 4-36, E is the beam energy, s_B is the bunch spacing, and f_c is the bunch collision frequency at the IP ($f_c = c/s_B$); V_{RF}, f_{RF}, and ϕ_s are the RF voltage, frequency,

Table 4-36. Main PEP-II parameters used in the beam-beam simulation studies.

	LER (e^+)	HER (e^-)
$\mathcal{L}_0$ [$cm^{-2}\ s^{-1}$]	3×10^{33}	
C [m]	2199.32	2199.32
E [GeV]	3.1	9.0
s_B [m]	1.26	
f_c [MHz]	238.000	
V_{RF} [MV]	9.5	18.5
f_{RF} [MHz]	476.000	476.000
ϕ_s [deg]	170.6	168.7
α	1.5×10^{-3}	2.41×10^{-3}
ν_s	0.050	0.052
σ_ℓ [cm]	1.0	1.0
σ_E/E	1.00×10^{-3}	0.616×10^{-3}
N [a]	5.630×10^{10}	2.586×10^{10}
I [A]	2.147	0.986
ε_{0x} [nm·rad]	61.27	45.95
ε_{0y} [nm·rad]	2.451	1.838
β_x^* [m]	0.375	0.500
β_y^* [m]	0.015	0.020
σ_{0x}^* [μm]	151.6	151.6
σ_{0y}^* [μm]	6.063	6.063
τ_x [turns]	5,014	5,014
τ_y [turns]	5,014	5,014

[a]These values for N do not take into account the existence of the ion-clearing gap, that is, they assume 1746 equally spaced bunches.

and synchronous phase, respectively; α is the momentum compaction factor; ν_s is the synchrotron tune; σ_ℓ is the rms bunch length; and τ_x, τ_y are the horizontal and vertical damping times, respectively. The other parameters are the emittances ε, beta functions β, and nominal rms beam sizes σ_0 at the IP.

The parameter values in Table 4-36 are consistent with Eq. 4-75 and our stated luminosity goal, as can be easily verified. The values do not, however, correspond exactly to the requirements of transparency symmetry, on account of the difference in the amplitudes of the tune modulation:

$$\left(\frac{\sigma_\ell \nu_s}{\beta_x^*}\right)_+ = 1.33\times 10^{-3}\,, \quad \left(\frac{\sigma_\ell \nu_s}{\beta_x^*}\right)_- = 1.04\times 10^{-3}$$
$$\left(\frac{\sigma_\ell \nu_s}{\beta_y^*}\right)_+ = 3.33\times 10^{-2}\,, \quad \left(\frac{\sigma_\ell \nu_s}{\beta_y^*}\right)_- = 2.60\times 10^{-2} \qquad (4\text{-}76)$$

(*ii*) *Select a working point.* Usually, only the primary collisions at the IP are considered in this step. The choice of tunes can be made quite effectively with "weak-strong" beam-beam simulations, in which the high-energy beam is forced to remain undisturbed while the low-energy beam is studied dynamically. (For PEP-II, we are confident that this approximation is reasonable, because more realistic "strong-strong" simulations show that there is little or no beam blowup for the high-energy beam in our design.) This more approximate type of simulation has the advantages that it is relatively fast and that the effects of resonances, such as synchrotron sidebands, are clearly seen (thus allowing, in principle, a theoretical understanding of the underlying beam dynamics). The main figure-of-merit that we use in this study is the beam blowup factor of the low-energy beam.

A tune scan is presented in Fig. 4-90, which shows the vertical and horizontal beam blowup factors of the low-energy beam for each working point scanned [Tennyson, 1991b] (the tunes shown are the "bare lattice" tunes). This tune scan was actually carried out for an earlier design, called APIARY 6.3D, and it *does* include the effect of the parasitic collisions. From the limited perspective of the beam-beam studies presented in this section, the APIARY 6.3D design differs from the present design basically in two ways: (a) the beta functions at the IP of the high-energy ring in the current design are 2/3 as large as they were in APIARY 6.3D and (b) the normalized separation between the beam orbits at the first parasitic crossing, $d/\sigma_{0x,+}$, is ~55% larger in the current design than it was in APIARY 6.3D. The beam-beam parameters and nominal luminosity are the same in the two designs, and the synchrotron tunes are almost the same. Since the parasitic collisions were shown to be weak relative to the IP collisions for APIARY 6.3D [Eden and Furman, 1992a, 1992b; Chin, 1991a; Tennyson, 1991a], and they are even weaker in the current design, as shown below, the tune scan in Fig. 4-90 is still relevant for the current design. Figure 4-91 shows the same portion of the tune plane, with resonance lines through sixth order. The beam-beam interaction causes a tune spread because particles of different betatron amplitude experience different tune shifts. This causes the beam to have a characteristic "footprint" (see Fig. 4-92) that extends diagonally upward from the working point.

For the beam-beam simulations, we have adopted, as suggested by the results in Fig. 4-90, a working point with fractional tunes $\nu_x = 0.64$ and $\nu_y = 0.57$ (both beams). Several existing colliders operate in this region of the tune plane, just above the half-integer [Rice, 1989, 1990; Seeman, 1985], which has the advantage of reduced sensitivity to closed-orbit errors. As our results (presented below) show, this working point is quite acceptable, and we are confident that an optimal working point can be found close to our current choice. Because of the asymmetry of the machine design, it is possible that the optimal working point will be different for the two rings; an optimization study along these lines will be carried out in the near future.

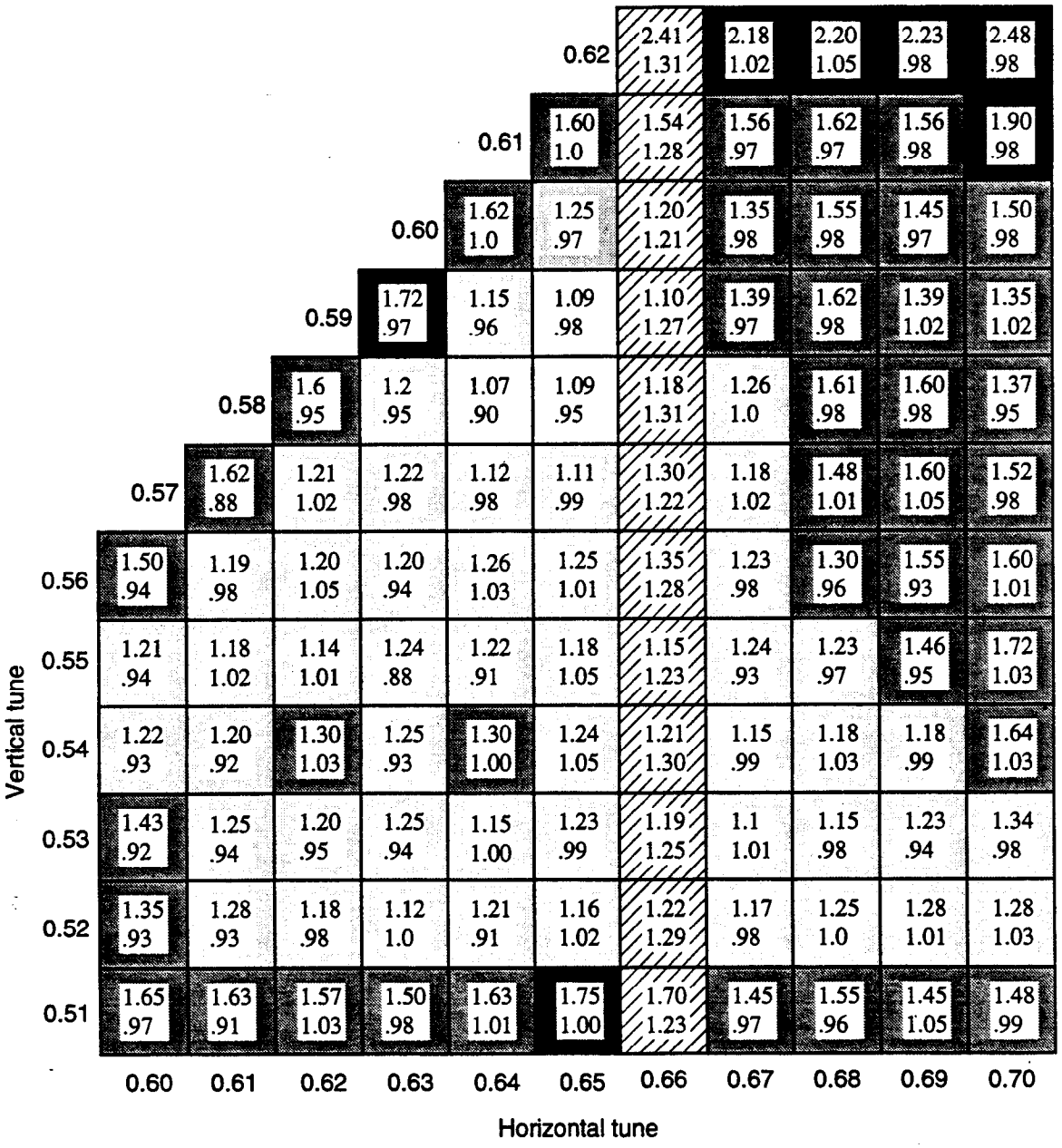

Fig. 4-90. Low-energy beam blowup factors (σ/σ_0) for various working points for the earlier PEP-II design APIARY 6.3D, including parasitic collisions. The numbers in each box are the vertical and horizontal blowup factors at that particular working point. The shading in each box is indicative of the blowup: the darker the shading, the larger the vertical blowup. The cross-hatched boxes indicate horizontal blowup >20%.

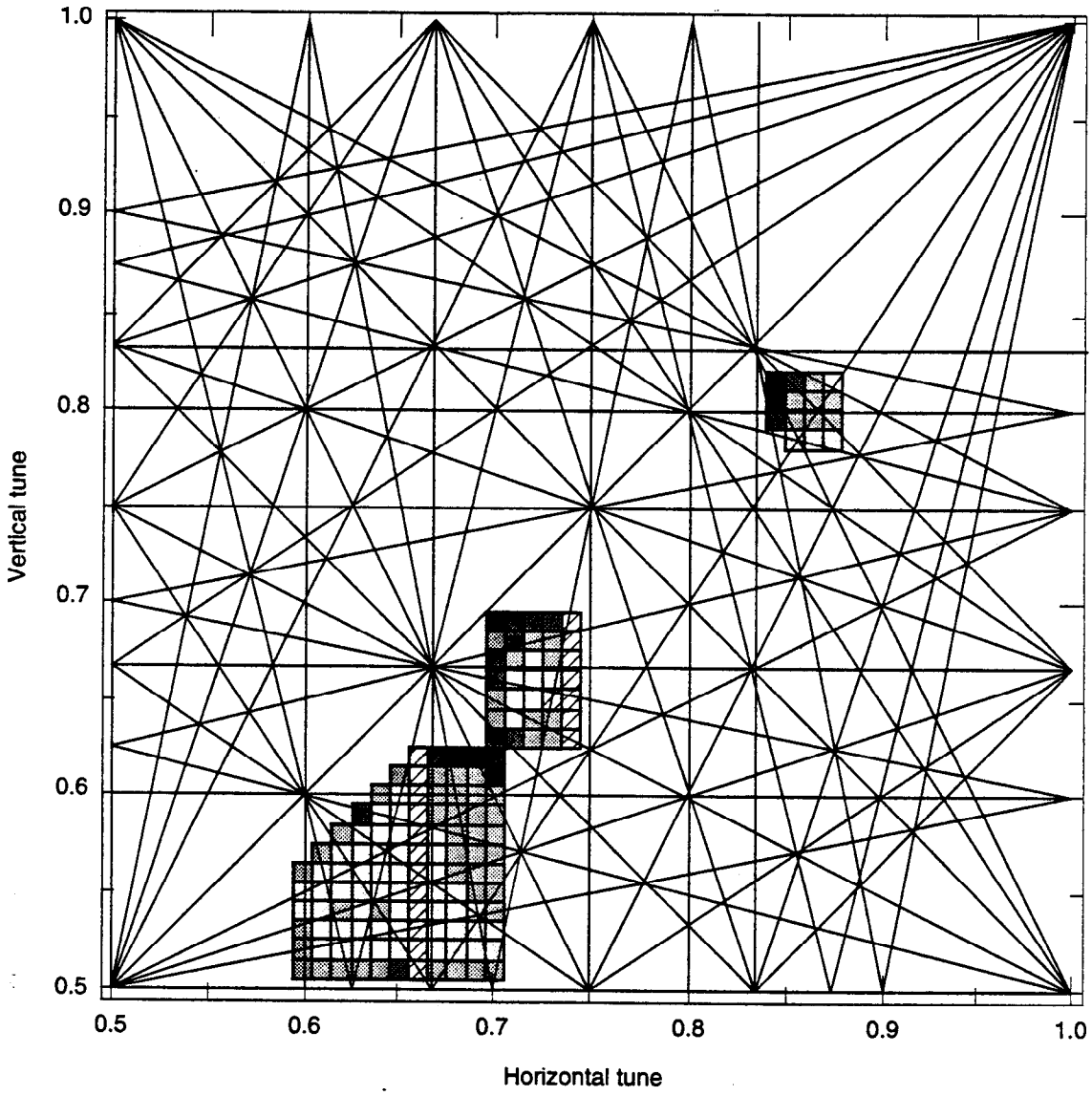

Fig. 4-91. Tune plot with even-order resonance lines through sixth order. This is the same portion of the tune plane as in the previous figure.

We will refer again to results for the earlier designs APIARY 6.3D [Furman, 1991] and APIARY 7.5 [Eden and Furman, 1992] in other subsections below. From the beam-beam perspective, there are only two differences between the present and previous designs: the beta functions of the HER are now smaller than before, and the normalized beam separation at the first parasitic collision is larger. The beam currents and emittances are adjusted such that the beam-beam parameters and nominal luminosity remain unchanged. A comparison is presented in Table 4-37.

(*iii*) *Verify the behavior of the beam-beam interaction.* The next step is to check that the beam-beam interaction remains reasonably weak in the fully coupled beam-beam calculations. This is done with "strong-strong" simulations, in which both beams are

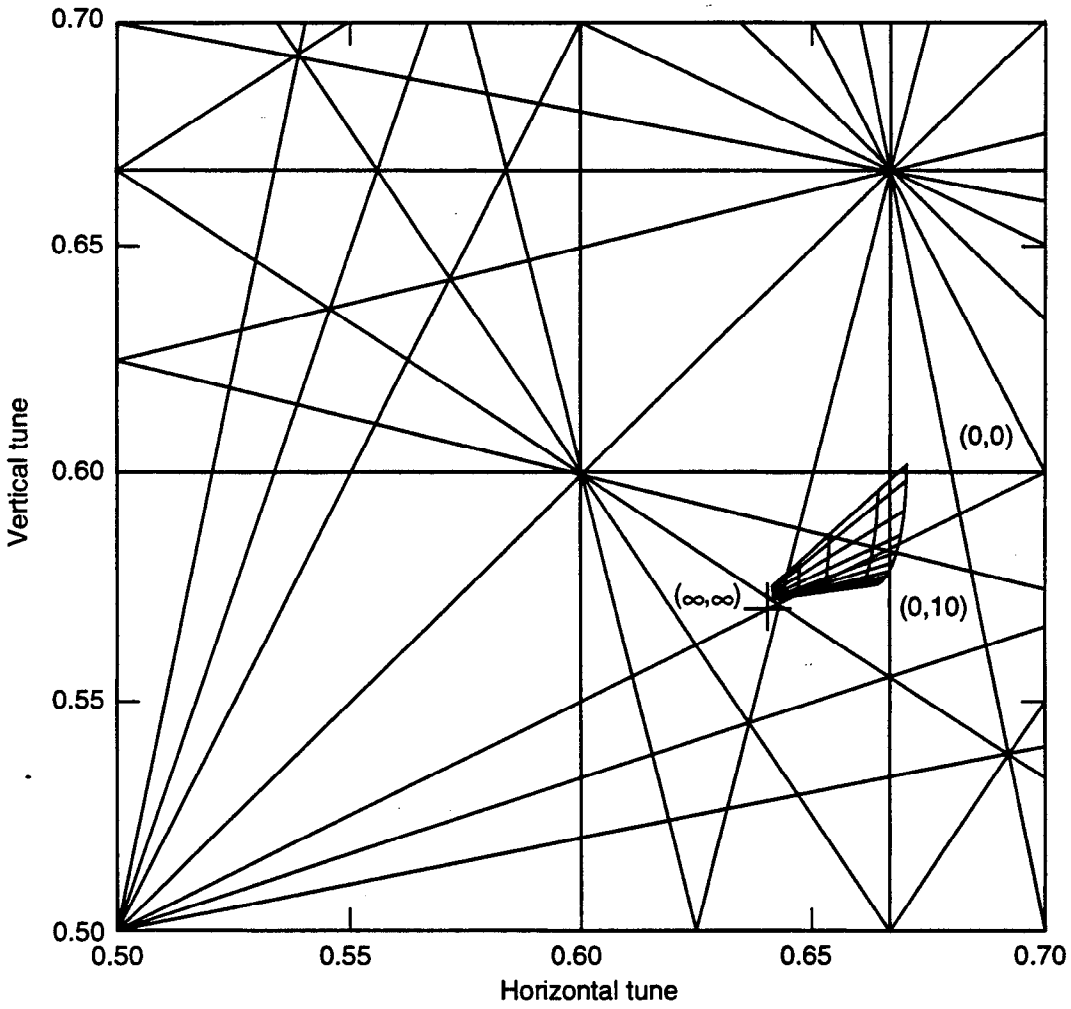

Fig. 4-92. Tune plot and beam footprint. The tune plane shows the working point (cross) and the beam footprint caused by the beam-beam tune spread. The lines in the footprint correspond to particles with amplitudes with constant σ_x or constant σ_y, at 0, 1, 2, 3, 4, 5, 6, 8 and 10σ. The particle closest to the working point has the largest amplitude, $10\sigma_x$ and $10\sigma_y$. The particle furthest away is at the center of the bunch and is labeled (0,0).

allowed to vary dynamically according to their mutual beam-beam interaction. During the initial stage, the study is done with only the primary collisions at the IP. This type of simulation is time consuming, but it is necessary because it is the only way to compute dynamical quantities, such as actual beam blowup and luminosity, and because it can reveal coherent oscillations, closed-orbit distortion, and particle losses. As a check on the robustness of our chosen parameters and working point, we have considered values of ξ_0 much higher than the nominal value of 0.03 in the simulations. This is shown in Fig. 4-93, which gives the calculated blowup factors of all four beam sizes vs ξ_0, and Fig. 4-94, showing the corresponding luminosities. In both Figs. 4-93 and 4-94, we maintain the equality of all four ξ_0 values (which are varied by simply increasing the

Table 4-37. Comparison between the current design and two earlier versions.

	Current design		APIARY 7.5		APIARY 6.3D	
	LEB	HEB	LEB	HEB	LEB	HEB
$\mathcal{L}_0$ [cm^{-2} s^{-1}]	3×10^{33}		3×10^{33}		3×10^{33}	
ξ_{0x}	0.03		0.03		0.03	
ξ_{0y}	0.03		0.03		0.03	
β_x^* [m]	0.375	0.50	0.375	0.75	0.375	0.75
β_y^* [m]	0.015	0.02	0.015	0.03	0.015	0.03
σ_{0x}^* [μm]	152		186		186	
σ_{0y}^* [μm]	6.1		7.4		7.4	
I [A]	2.1	1.0	2.1	1.5	2.1	1.5
d [mm] [a]	3.5		3.5		2.8	
d/σ_{0x} [a]	11.8	14.3	9.6	14.4	7.6	11.5

[a] d is the beam separation at the first parasitic collision, and d/σ_{0x} is the separation normalized to the local horizontal beam size.

number of particles per bunch). In general, the two codes predict reasonably similar dynamical behavior. (The discrepancy at large ξ_0 is probably related to the different ways the two codes handle coherent oscillations, which are significant at such extreme parameter values.)

Because the various beam sizes change differently, the dynamical beam-beam parameters also become different from each other. This means that the transparency symmetry is inherently broken by the dynamics, although not to a great extent.

(*iv*) *Verify that the results are maintained when parasitic crossings are included.* Although the beams collide head-on at the IP, the bunches experience grazing collisions on their way into and out of the region within about ±3 m of the IP, where both beams travel in a common pipe. We must assess the effect of these parasitic crossings on the performance. This is done with strong-strong simulations. Parasitic crossings have a potentially detrimental effect on beam blowup, because they induce odd-order resonances and horizontal-vertical coupling. Taken together, these effects make it harder to find an optimum working point in the tune plane.

There are four parasitic crossings symmetrically located on either side of the IP. All of them occur in the horizontal plane. For the purposes of studying the beam-beam dynamics, the first parasitic crossing (that is, the one closest to the IP on either side) overwhelms the others on account of the relatively small separation, together with the large vertical beta function. The strength of the long-range beam-beam kick at this first parasitic crossing is much greater than those of all the remaining crossings combined. This fact, discussed in more detail below, justifies our considering only this first parasitic

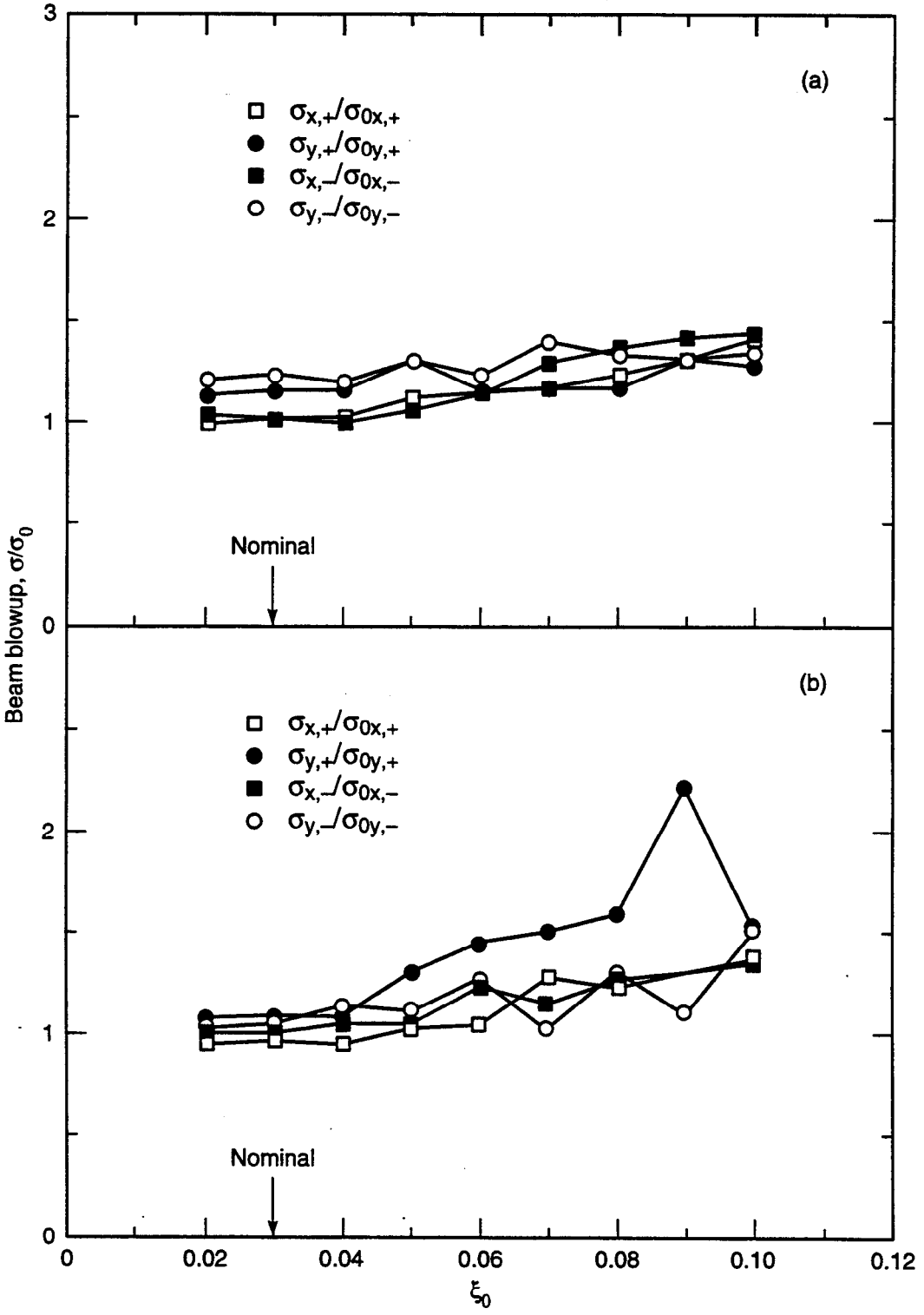

Fig. 4-93. Beam blowup factors vs ξ_0 (IP collisions only). These are the results for the dynamical beam size over nominal beam size for both beams, from both simulation codes: (a) Yokoya's and (b) TRS. The parameter ξ_0 is increased by increasing the number of particles per bunch in both beams, with fixed nominal emittance.

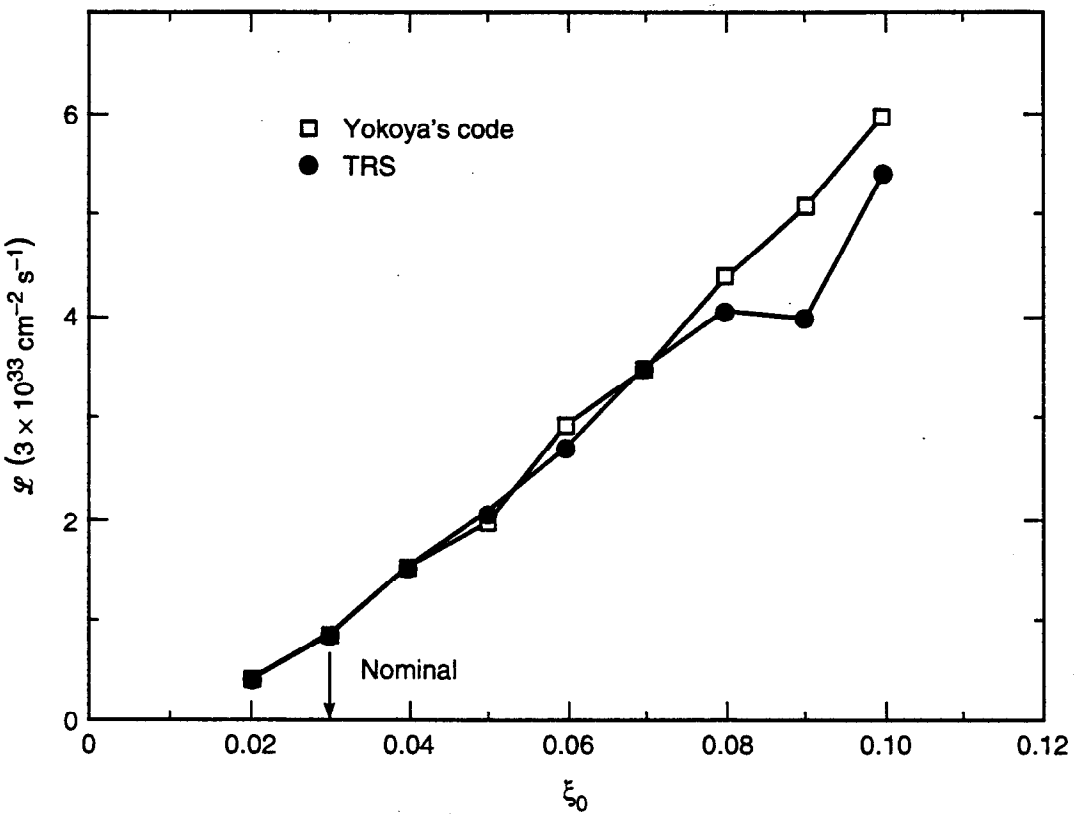

Fig. 4-94. Luminosity vs ξ_0 corresponding to the blown-up beam sizes in Fig. 4-93 (IP collisions only).

crossing in our present calculations. Table 4-38 shows the relevant parameters for the primary and the first parasitic crossing for PEP-II.

In Table 4-38, Δs is the distance from the IP to the parasitic crossing point along the beam trajectory; $2\pi\Delta\nu_x$ and $2\pi\Delta\nu_y$ are the phase advances from the IP to the parasitic crossing; d is the (horizontal) separation between the two closed orbits at the parasitic crossing; and d/σ_{0x} is a measure of the extent of the overlap between the two bunches at the parasitic crossing point. The nominal emittances and number of particles per bunch are listed in Table 4-36. The parasitic crossings induce a tune shift and an amplitude-dependent tune spread in the particles due to the mutual interaction of the two bunches. It can be shown that the incoherent beam-beam parameters of a particle at the center of the positron bunch from a single parasitic interaction point are, to lowest-order approximation, given by [Tennyson, 1991a]

$$\xi_{0x,+}^{(PC)} = -\frac{r_0 N_- \beta_{x,+}}{2\pi\gamma_+ d^2}$$

$$\xi_{0y,+}^{(PC)} = +\frac{r_0 N_- \beta_{y,+}}{2\pi\gamma_+ d^2} \qquad (4\text{-}77)$$

Table 4-38. PEP-II nominal parameters at the IP and first parasitic crossing.

	LER (e^+)		HER (e^-)	
Δs [cm] [a]	63			
d [mm] [a]	3.50			
	IP	First PC	IP	First PC
$\Delta\nu_x$ [a]	0	0.1645	0	0.1432
$\Delta\nu_y$ [a]	0	0.2462	0	0.2449
β_x [m]	0.375	1.43	0.500	1.29
β_y [m]	0.015	26.46	0.020	19.85
α_x	0	–1.68	0	–1.26
α_y	0	–41.99	0	–31.49
σ_{0x} [μm]	151.6	296.3	151.6	243.8
σ_{0y} [μm]	6.063	254.6	6.063	191.0
$\sigma_{0x'}$ [mrad]	0.404	0.404	0.303	0.303
$\sigma_{0y'}$ [mrad]	0.404	0.404	0.303	0.303
d/σ_{0x}	0	11.81	0	14.35
ξ_{0x}	0.03	–0.000224	0.03	–0.000152
ξ_{0y}	0.03	+0.004133	0.03	+0.002326
$\xi_{0x,\mathrm{tot}}$ [b]	0.0296		0.0297	
$\xi_{0y,\mathrm{tot}}$ [b]	0.0383		0.0347	

[a] The first PC occurs at a distance Δs and at a phase advance $\Delta\nu$ from the IP. At this point the nominal orbits are separated horizontally by a distance d.

[b] The total nominal beam-beam parameter is defined to be $\xi_{0,\mathrm{tot}} \equiv \xi_0^{(\mathrm{IP})} + 2\xi_0^{(\mathrm{PC})}$

with the corresponding expressions for the electron bunch obtained by exchanging the indices + and – in Eq. 4-77. Here $\beta_{x,y}$ are the beta functions at the parasitic crossing location. The negative sign in the expression for $\xi_{0x,+}^{(\mathrm{PC})}$ arises from the fact that the horizontal force is a decreasing function of separation at the parasitic crossing. Using the numerical values for the parameters given in Table 4-38, we obtain

$$\begin{aligned} \xi_{0x,+}^{(\mathrm{PC})} &= -0.00022, \qquad \xi_{0x,-}^{(\mathrm{PC})} = -0.00015 \\ \xi_{0y,+}^{(\mathrm{PC})} &= +0.0041, \qquad \xi_{0y,-}^{(\mathrm{PC})} = +0.0023 \end{aligned} \tag{4-78}$$

which shows that the first parasitic crossings together contribute a vertical tune shift of approximately 0.008 to the nominal IP tune shift of 0.03 in the positron beam. The remaining parasitic crossings contribute negligibly to the tune shifts.

A tune shift by itself is not detrimental, since it can be compensated by a shift in the working point. However, as mentioned above, the amplitude dependence causes a tune spread, which is more problematic. This spread, which can be calculated by appropriate numerical integration [Tennyson, 1991a; Siemann, 1993], causes a distortion of the beam footprint, as shown in Fig. 4-95. Such a distortion makes it more difficult to find a good working point; for our present simulation purposes, we have maintained the original working point, $\nu_x = 0.64$, $\nu_y = 0.57$.

As implied by the above, the parasitic crossings produce horizontal-vertical coupling that can cause beam blowup. Obviously if the separation d were large enough, all effects of the parasitic crossings would disappear altogether. To assess this effect, we have carried out simulations in which we vary the separation d and keep all other parameters

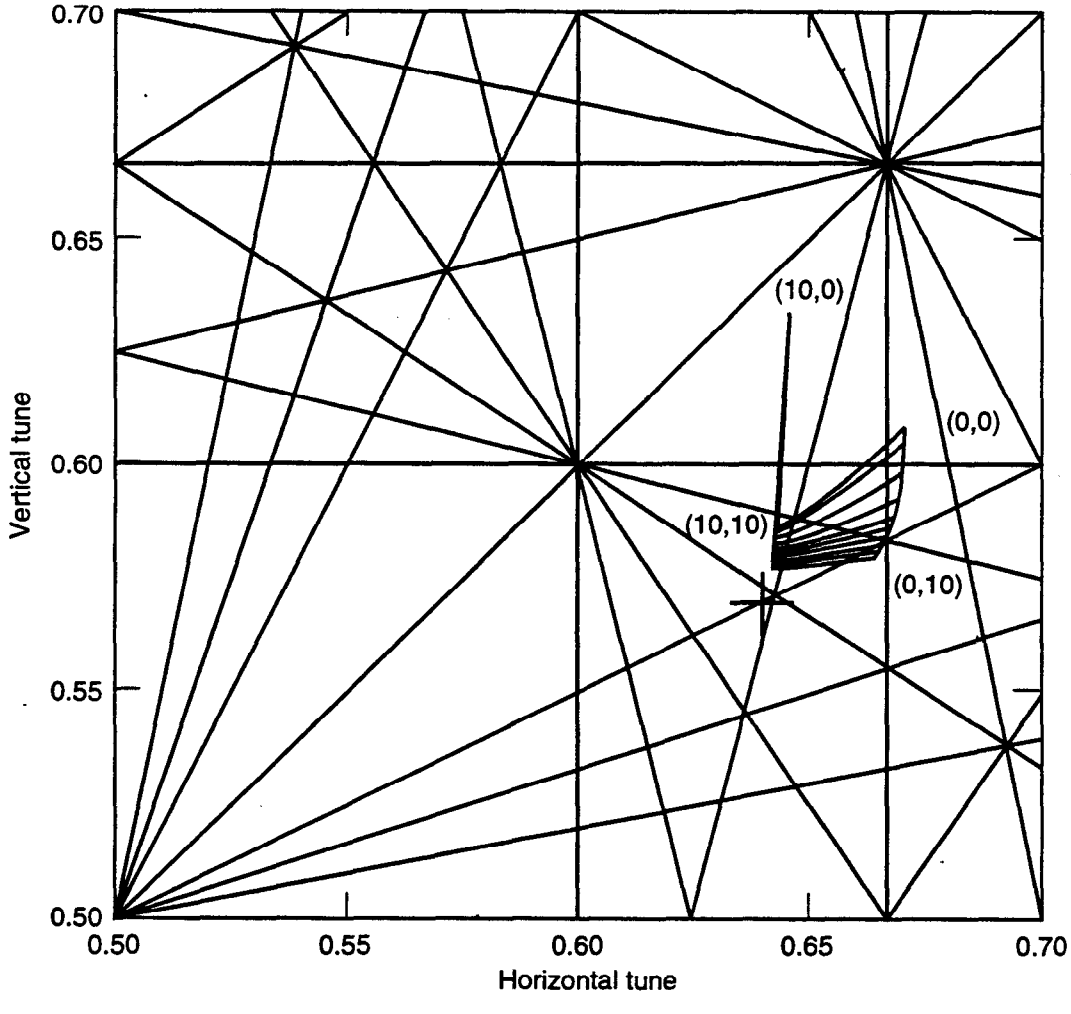

Fig. 4-95. Beam footprint of the LEB, including the effect of the parasitic crossings. The large-amplitude distortion of the footprint produced by the long-range collision is apparent (see Fig. 4-92 for a comparison). The lines in the footprint correspond to particles with constant amplitude (vertical and horizontal) at 0, 1, 2, 3, 4, 5, 6, 8 and 10σ.

fixed. Figure 4-96 shows the beam blowup factors vs $d/\sigma_{0x,+}$ for $\xi_0 = 0.03$, obtained with TRS. Figure 4-97 shows the vertical beam blowup factors for the LEB from both codes for $\xi_0 = 0.03$ and 0.05. Figure 4-98 shows the corresponding luminosity vs $d/\sigma_{0x,+}$ for $\xi_0 = 0.03$ and 0.05. This larger value of ξ_0 is obtained by increasing the number of particles per bunch by a factor of 5/3, at fixed nominal emittance.

The lack of smoothness in the blowup curves as $d/\sigma_{0x,+}$ increases, particularly for $\xi_0 = 0.05$, is almost certainly due to resonance effects. Indeed, as d varies, the cores of the two beams sample different areas of the tune plane on account of the d-dependence of the long-range beam-beam parameter, Eq. 4-77. This effect can be compensated by appropriate changes of the bare-lattice working points of the two beams. Simulations with such tune-compensation have been carried out, and they indeed show smoother blowup curves [Eden and Furman, 1993b].

As mentioned above, there are four parasitic collisions on either side of the IP. Table 4-39 summarizes the relevant parameters for all collisions, including the IP. In this table, s is the distance from the IP where the collision takes place and d is the separation between the beam orbits at that location (in all cases the separation is purely horizontal). The nominal beam-beam parameters ξ_0 of a particle at the center of the bunch are computed according to Eq. 4-77.

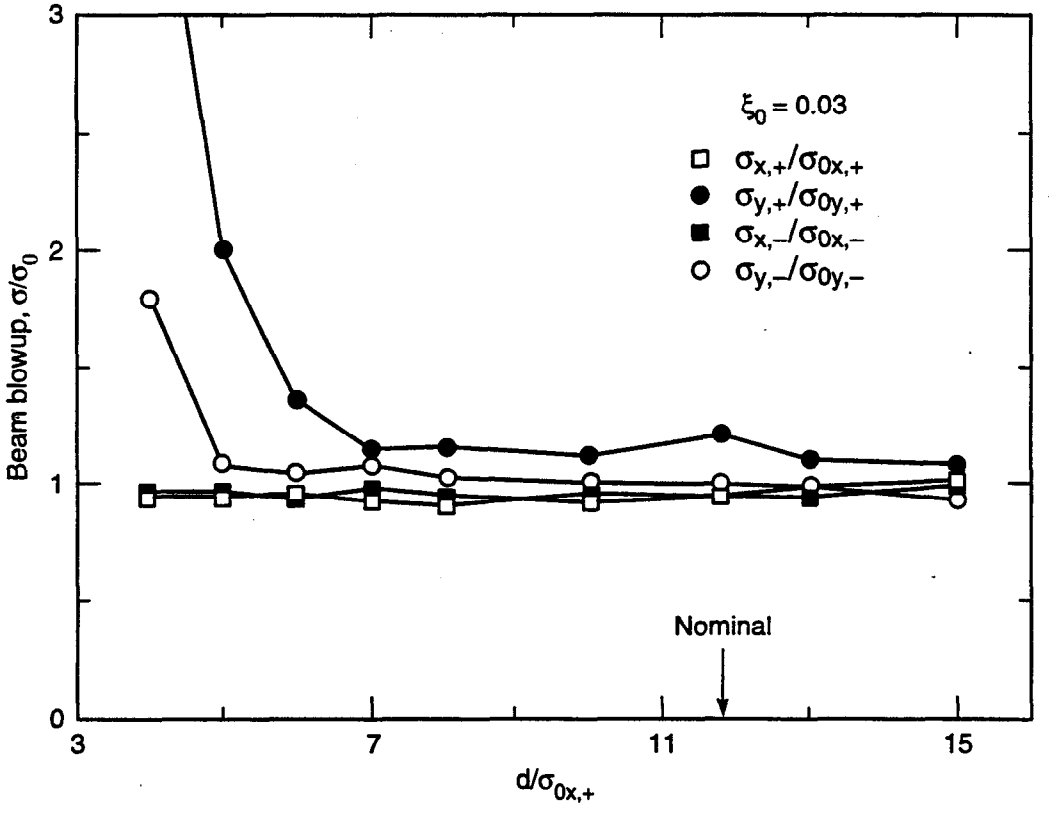

Fig. 4-96. Beam blowup factors vs $d/\sigma_{0x,+}$ for both beams obtained with TRS for $\xi_0 = 0.03$. The nominal beam separation at the parasitic collision, indicated by the arrow, corresponds to $d/\sigma_{0x,+} = 11.8$.

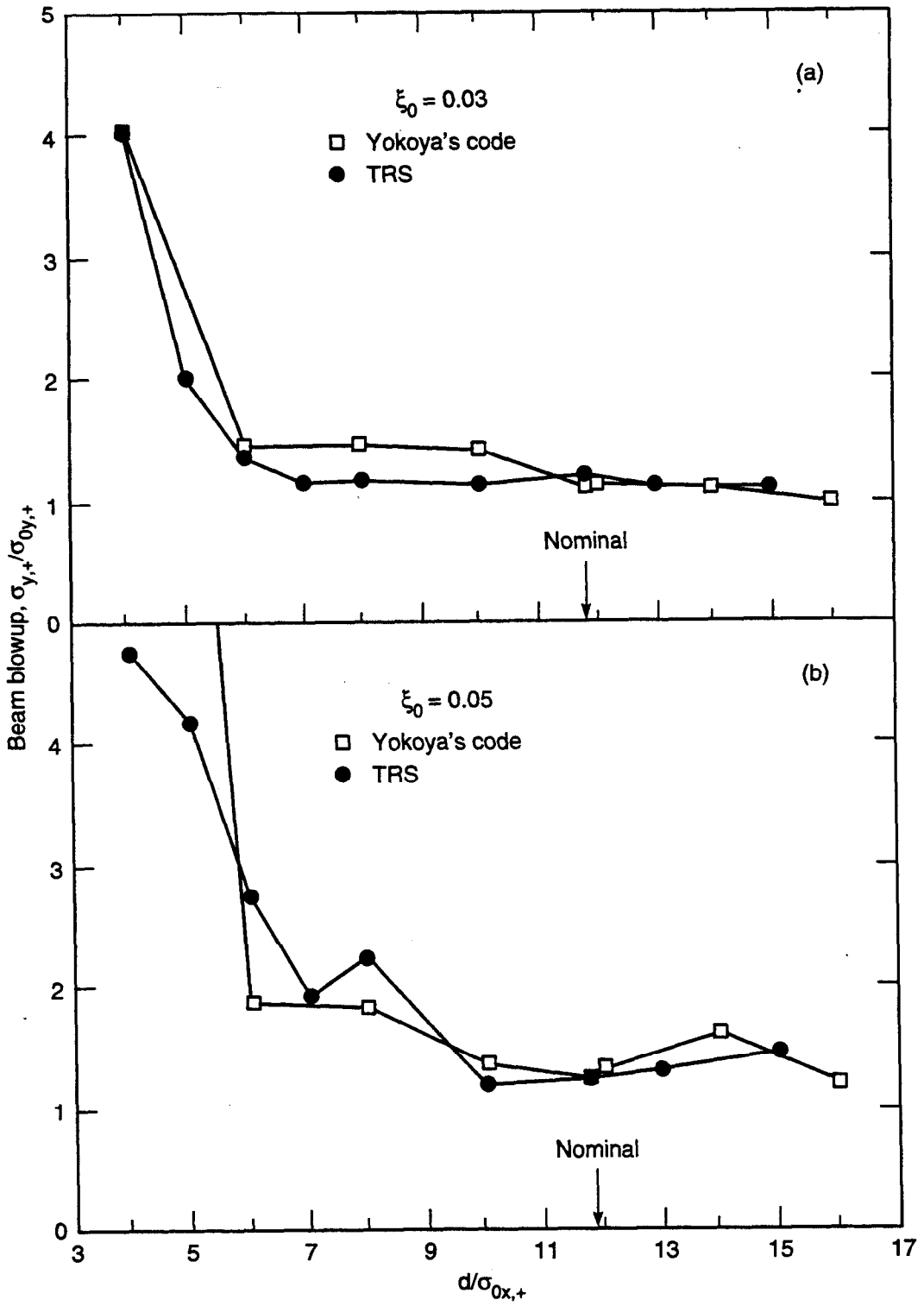

Fig. 4-97. Vertical beam blowup factor for the low-energy (positron) beam vs $d/\sigma_{0x,+}$ for (a) $\xi_0 = 0.03$ and (b) $\xi_0 = 0.05$. The nominal beam separation at the parasitic crossing, indicated by the arrow, corresponds to $d/\sigma_{0x,+} = 11.8$. The remaining three beam sizes are not shown because they exhibit blowup (or contraction) factors of 10% or less in all cases, except at very low values of $d/\sigma_{0x,+}$.

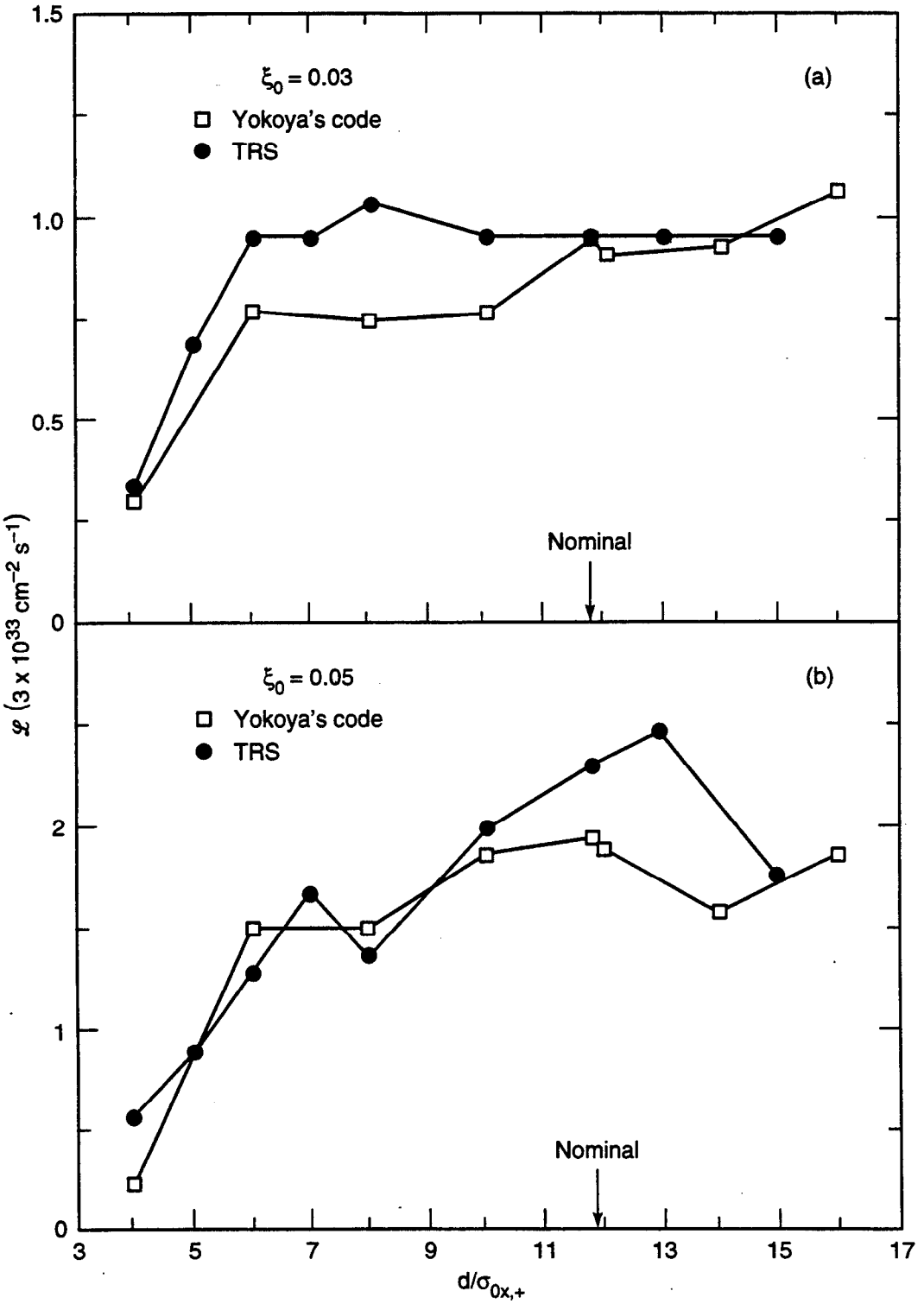

Fig. 4-98. Luminosity vs $d/\sigma_{0x,+}$ for (a) $\xi_0 = 0.03$ and (b) $\xi_0 = 0.05$, corresponding to the blown-up beam sizes shown in Fig. 4-97. Note that, for $\xi_0 = 0.05$, the nominal value of the luminosity is 8.3×10^{33} cm^{-2} s^{-1}.

Table 4-39. Parameters at the IP and all four parasitic crossings.

LER (e^+)				
s (m)	d (mm)	d/σ_{0x}	ξ_{0x}	ξ_{0y}
0.0 (IP)	0.0	0.0	+0.030000	+0.030000
0.63	3.498	11.8	–0.000224	+0.004133
1.26	17.651	33.2	–0.000028	+0.000648
1.89	39.114	39.3	–0.000020	+0.000167
2.52	71.879	38.4	–0.000021	+0.000026
HER (e^-)				
s (m)	d (mm)	d/σ_{0x}	ξ_{0x}	ξ_{0y}
0.0 (IP)	0.0	0.0	+0.030000	+0.030000
0.63	3.498	14.3	–0.000152	+0.002326
1.26	17.651	43.0	–0.000017	+0.000365
1.89	39.114	60.3	–0.000009	+0.000139
2.52	71.879	73.3	–0.000006	+0.000053

The simulation studies presented above indicate that the effect of the parasitic collisions on beam blowup becomes negligible compared with that from the IP when the relative separation $d/\sigma_{0x,+}$ is $\gtrsim 7$. Because the parasitic collisions beyond the first have $d/\sigma_{0x,+} \geq 33.2$, we are confident that their contribution to beam blowup is insignificant. (To account for the combined beam-beam tune shifts of the additional parasitic crossings, a small adjustment of the working point may be needed.)

It is likely that the only significant effect of the parasitic collisions beyond the first would be to excite a coherent dipole mode in the beams. However, because the combined beam-beam tune shifts of these additional parasitic crossings are small, this coherent dipole mode is likely to be insignificant except when the working point is very close to an integer or half-integer, a situation that will be avoided.

4.4.5 Beam Tail Simulations

The beam-beam problem is usually studied in two regimes: the core particles and the tail particles. The two regimes are very different in terms of their physics issues and their effects on machine performance. From an operational point of view, the core particles determine the luminosity, whereas the tail particles determine the lifetime and influence detector backgrounds (both aspects being critical to successful operation).

Compared with the core-particle problem, the tail problem has not been well studied, either with analytical calculations or simulations. The reason for the lack of simulation

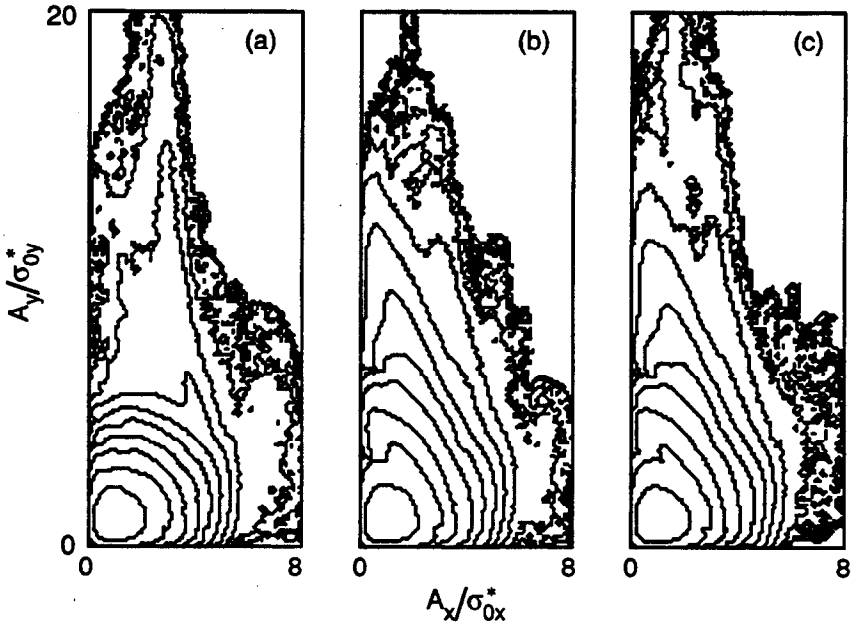

Fig. 4-99. Beam distributions from simulation: (a) without synchrotron motion; (b) with synchrotron motion; (c) with synchrotron motion and parasitic crossings. The horizontal and vertical axes scales are A_x/σ^*_{0x} and A_y/σ^*_{0y}, where $A = \sqrt{2J\beta}$ is the amplitude.

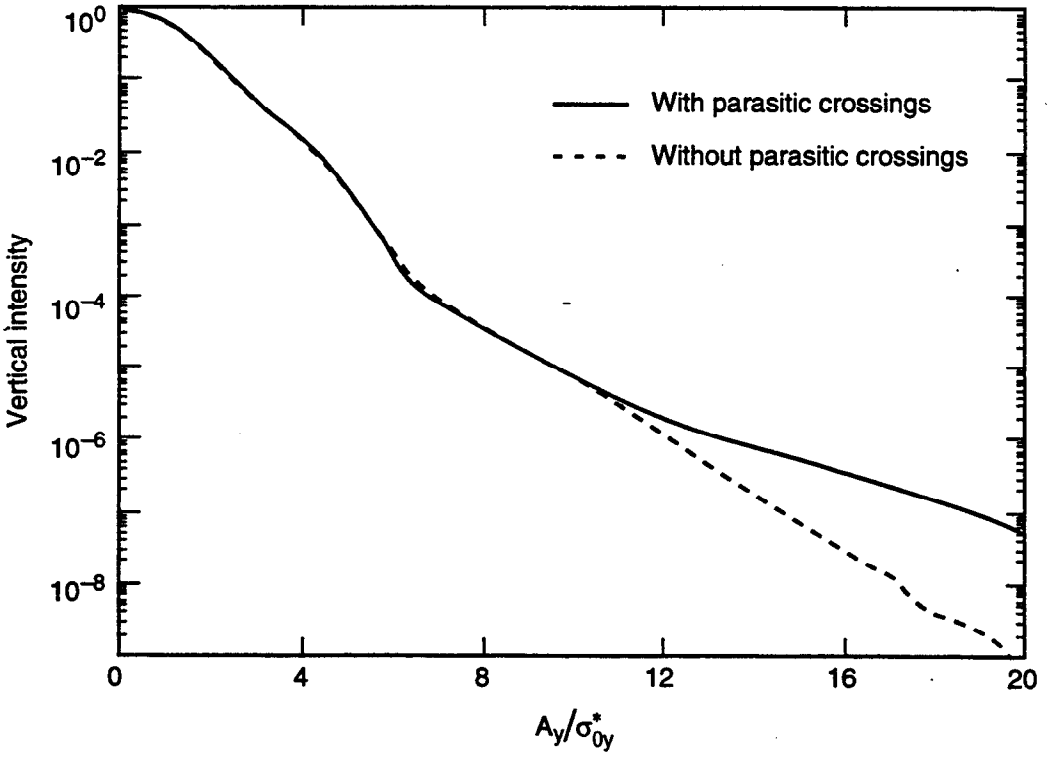

Fig. 4-100. Vertical beam distribution with and without parasitic crossings for the low-energy beam.

results is that particles are rarely in the tail. Even though the number of particles moving into the tail is large enough to degrade the beam lifetime, it is not large enough to provide a tail distribution with satisfactory statistical accuracy in a typical beam-beam simulation with a few hundred superparticles. That is, a simulation with a huge number of particle-turns would be required to give a single tail distribution, which prevents this problem from being studied systematically by standard beam-beam codes.

To avoid this limitation, a new simulation code has been developed by Irwin [1992]. Instead of tracking billions of particle-turns in the core, we concentrate on the particles that are evolving into the tail. To do this, an imaginary boundary is drawn in normalized amplitude space to separate about 100 particles (out of 1000 particles) moving in the tail. Then, we continue tracking the particles and randomly save the coordinates of particles that are above the boundary, until 1000 particle coordinates have been saved. Meanwhile, the coordinate information for any particles that move up across the boundary is also saved. At this point, we track 1000 particles outside the boundary. During the tracking, any particle that drops below the boundary will be reinserted above it by using new coordinates from the crossing information saved previously. After sufficient tracking time (a few damping times), a second boundary (at larger amplitudes) is created and 100 particles outside the second boundary are evolved into 1000 particles. This process can be repeated a few times to keep tracking particles that are going into the tail. Each time we increase the boundary amplitude, we gain a factor of 10 for the number of particles in the tail.

The results of the Irwin code have been compared with the results of conventional tracking for 6 billion particle-turns. Excellent agreement has been achieved, using only 2% of the particle-turns of the conventional tracking code. This indicates that the new simulation code is a very powerful tool for studying beam-tail distributions.

The code features six-dimensional phase-space tracking, one interaction point with asymmetric beam parameters, a linear arc transport with energy-dependent phase advance and beta functions, parasitic crossings, and a multiple-slice beam-beam kick at the interaction point. It has been developed to meet the requirements of PEP-II performance studies.

Figure 4-99 shows the results of a simulation for the PEP-II LER in which the strong bunch is segmented into five slices. An equivalent of about 70 billion particle-turns was simulated. The results show that synchrotron motion is important in the beam-tail distribution. The parasitic crossings do not appear to affect the distribution very much. However, they do change the large amplitude tail by a small amount, which has an impact on lifetime. Figure 4-100 compares the beam distributions in the vertical plane with and without parasitic crossings. The distributions split at large amplitudes. Based on these data, the lifetime can be estimated: For a two-hour lifetime, a $16.5\sigma_y$ physical aperture in the vertical plane is required without parasitic crossings, and a $22\sigma_y$ physical aperture is required with parasitic crossings. (For comparison, we note that the dynamic aperture of the LER exceeds 35σ in the vertical plane, as shown in Section 4.1.3.3.)

More work will be carried out to check various effects, such as different working points and lattice nonlinearities. Our goal is to identify possible problems, rather than to predict the actual operational performance of PEP-II.

size reaches its peak value (about 11 times the nominal storage ring beam size) very quickly, within approximately 300 turns; the beam blowup then damps gradually in the following few radiation damping times. No particle loss was found in the simulation.

The simulations show that the horizontal beam size also blows up, to about three times the nominal stored-beam value, but much more slowly (roughly one radiation damping time). A detailed investigation of the time evolution of the horizontal phase-space distribution shows that the injected beam is sheared into an elongated shape, and eventually spreads out over a circular annulus in horizontal phase space, due to horizontal kicks from the other beam. This leads to a rapid damping of the horizontal baricentroid motion even though the particle amplitudes themselves have not yet been significantly damped. The process would likely be enhanced if the amplitude-dependent tune shifts due to lattice nonlinearities were taken into account.

Although the resultant performance of the horizontal injection scheme in the APIARY 6.3D design would have been acceptable, we have explored two alternative injection schemes in an attempt to seek a solution that entails less blowup of the injected beam. One such scheme is to inject beams vertically instead of horizontally. Obviously, this scheme prevents the injected beam from approaching the other beam at the first parasitic crossing more closely than the nominal separation distance between the two stored-beam orbits. Another scheme is horizontal injection, but with vertical separation at both the IP and the first parasitic crossing (produced by a bumped orbit during the injection process). Simulation results for both of these schemes show substantial reduction of the blowup of the injected beam sizes. No particle loss was found in either case.

Based on these results, we adopted a vertical injection scheme for the intermediate design, APIARY 7.5. Because the two beams cannot get any closer at the parasitic collision point than the nominal (stored-beam) separation distance, the beam-beam kick is weaker on average than during steady-state colliding-beam operation. However, the parasitic beam-beam interaction, being a collision of the two beams at large amplitude in phase space, still tends to shear the injected beam into an elongated shape in vertical phase space. The process is accelerated as the coherent vertical oscillation of the injected beam damps away, because the distance between the two beams gets shorter on average. This behavior, schematically illustrated in Fig. 4-101, is a peculiar point that contrasts with the horizontal injection case (in which the parasitic beam-beam interaction becomes *weaker* as the horizontal coherent oscillation of the injected beam damps away). Obviously, the parasitic beam-beam interaction in both cases approaches the same strength in the steady state.

Although the present design has a substantially larger beam separation at the first parasitic collision and smaller long-range beam-beam parameters for the LEB compared with our earlier designs, we have retained the vertical injection scheme. In this way, we are certain to avoid potentially adverse effects from close encounters of the beams at the parasitic crossing points during injection.

The main storage ring and injection parameters of the present design are listed in Table 4-40; the numbers in square brackets are the values of the corresponding parameters at the time of injection. As in previous simulations, we consider only the first parasitic crossing (that closest to the IP) on either side, because it overwhelms the others.

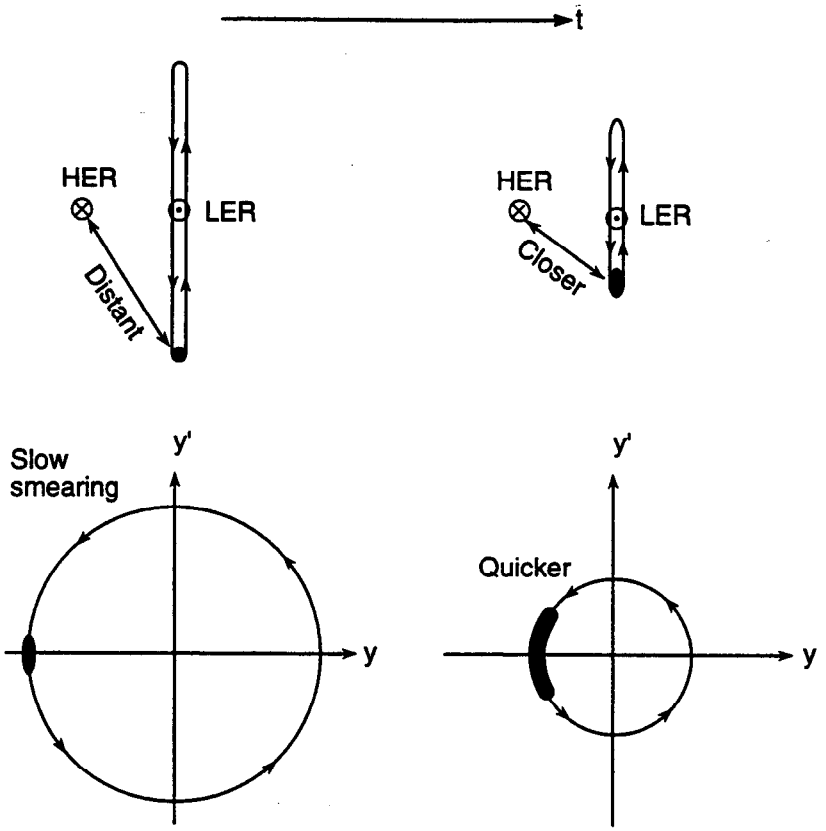

Figure 4-101. Schematic illustration of the parasitic beam-beam interaction during the vertical injection process.

A bunch with 20% of the nominal single-bunch current is injected into the LER with a vertical displacement $22\sigma_{iy}$ from the stored-beam orbit, where σ_{iy} is the nominal (stored-beam) vertical beam size of the LER at the injection point. We assume that the phase advance between the injection point and the first parasitic crossing point is 2π times an integer. The fractional tunes of the working point are taken as $\nu_x = 0.64$ and $\nu_y = 0.57$ for both beams.

Figure 4-102 shows the rms sizes of the injected beam, in units of the nominal stored-beam sizes, versus the turn number after injection. The evolution of the baricentroid motion of the injected beam is shown in Fig. 4-103. The largest turn number, 20000, corresponds to about four radiation damping times. We see that the vertical beam size reaches its peak value of $\sim 3\sigma_{0y}$ very quickly, within approximately 1000 turns. The beam blowup then damps out gradually in the following few radiation damping times. Horizontally, the injected beam converges monotonically toward its equilibrium size due to radiation damping. At an early stage of the simulation, the injected beam is sheared into an elongated shape. This elongated shape closes to a circular annulus after approximately 8000 turns, that is, roughly two damping times. Accordingly, the vertical baricentroid position settles down at the origin as shown in Fig. 4-103. No particle loss from the 200 superparticles was found during the simulation. The high-energy beam sizes, which are not plotted here, show practically no change from their nominal values.

Table 4-40. PEP-II parameters used in the injection simulation studies of the LER. Parameters in brackets are those of the injected beam at the time of injection; the other values correspond to the nominal stored beams.

	LER (e^+)		HER (e^-)	
E [GeV]	3.1		9.0	
C [m]	2200		2200	
$\tau_x = \tau_y$ [turns]	5014		5040	
I_b [mA]	[0.246]		0.565	
σ_ℓ [cm]	1.0		1.0	
ε_{0x} [nm·rad]	61.3 [8.24]		45.9	
ε_{0y} [nm·rad]	2.45 [8.24]		1.84	
d [mm]	3.50			
	IP	First PC	IP	First PC
β_x [m]	0.375	1.43	0.50	1.29
β_y [m]	0.015	26.46	0.02	19.85
σ_{0x} [μm]	152 [56]	296 [109]	152	244
σ_{0y} [μm]	6.06 [11.1]	255 [467]	6.06	191
d/σ_{0x}	0	11.8 [25.2]	0	14.4
A_x/σ_{0x}	10		10	
A_y/σ_{0y}	36		36	

We conclude from these results that the vertical injection scheme is quite comfortable in terms of the beam-beam dynamics. It leads to very little beam blowup and to no particle losses (to the extent that these simulations are able to predict).

4.4.6.2 Simulations with Displaced Beams at Full Current. In this section, we summarize simulation results corresponding to the state reached after injection is complete but the beams are still separated. If the beams are slowly brought into collision in step (4) of the injection process, the results presented in this section also allow a rough understanding of what would happen during this beam-collapsing process. One implicit assumption that is necessary for the relevance of these simulations to the beam-collapsing process is that the time scale for switching off the orbit bumps is longer than a few damping times. If the beam-collapsing process is fast (on the order of one damping time or less), our simulations are probably relevant only to the static situation existing before step (4) is taken. We are also assuming that multibunch coherent beam-beam instabilities are not excited in the separated state or during the beam-collapsing process.

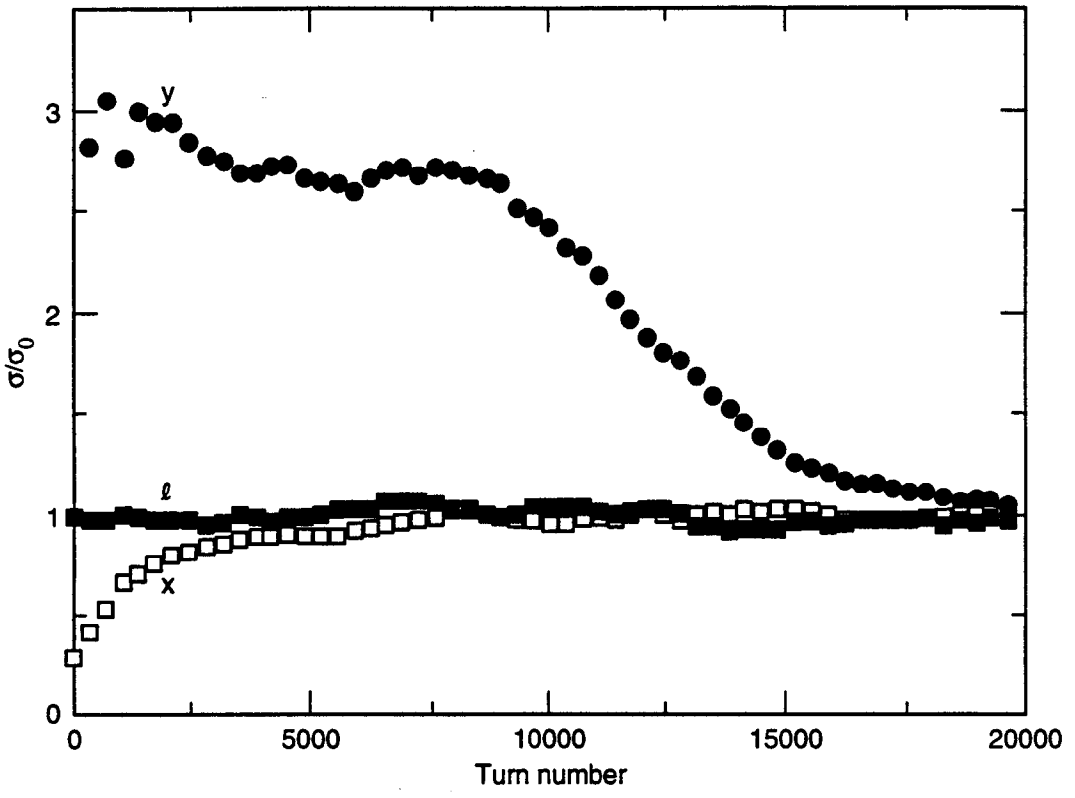

Figure 4-102. Time evolution of the injected beam sizes of the LEB, in units of the nominal stored-beam sizes, during the vertical injection process.

The results below are in the form of beam blowup, σ/σ_0, plotted versus d_x/σ_{0x} or d_y/σ_{0y} for horizontal or vertical separation, respectively, where σ_{0x} and σ_{0y} are the nominal, steady-state, rms beam sizes at the IP, and d_x or d_y is the orbit separation at the IP in either case. In the horizontal separation case, we varied d_x while keeping d_y fixed, and vice versa for the vertical case. We assume that the beam separation is implemented by a closed-orbit bump that is symmetric about the IP and whose elements (orbit bump magnets) are outside the region encompassing the IP and the first parasitic collision points (however, see the discussion below). Since there are no focusing elements between the IP and the first parasitic collisions, the closed orbits inside this region are parallel-displaced from the nominal orbits. As a result, the orbit separation at each parasitic collision is related to that at the IP by simple geometry as follows:

$$\text{Horizontal separation case:} \quad \begin{cases} d_{IP} = d_x & (d_y = 0, \text{ fixed}) \\ d_{PC1} = d_0 + d_x & (d_y = 0, \text{ fixed}) \\ d_{PC2} = d_0 - d_x & (d_y = 0, \text{ fixed}) \end{cases} \tag{4-79}$$

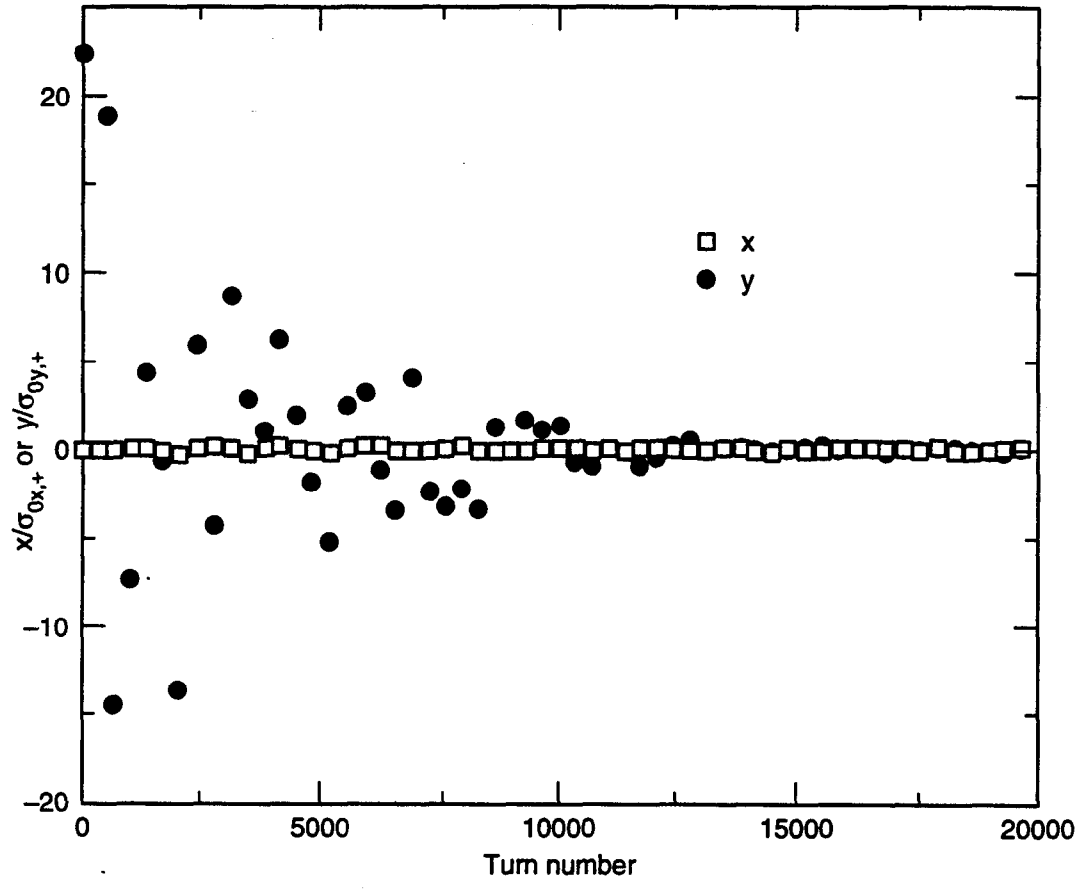

Figure 4-103. Time evolution of the baricentroid positions of the injected low-energy beam, in units of the nominal stored-beam sizes, during the vertical injection processes.

$$\text{Vertical separation case:} \quad \begin{cases} d_{IP} = d_y & (d_x = 0, \text{ fixed}) \\ d_{PC1} = d_y & (d_x = d_0, \text{ fixed}) \\ d_{PC2} = d_y & (d_x = d_0, \text{ fixed}) \end{cases} \tag{4-80}$$

where d_0 is the nominal orbit separation at the first parasitic collision ($d_0 = 3.5$ mm). Parasitic collisions beyond the first were not considered, even though the horizontal-separation alternative would almost certainly demand that they be included in a faithful simulation. The simulation was run with the code TRS at the working point (0.64, 0.57).

In the horizontal-separation alternative, Eq. 4-79 shows that, as the beams are displaced, one of the parasitic collisions (called PC2) gets stronger while the other one (PC1) gets weaker. The collision at the IP also gets weaker. As one can see in Fig. 4-104, beam blowup is not significant provided the separation at the IP is such that $d_x/\sigma_{0x} \lesssim 5$–10. In this regime, the parasitic collisions are still well separated (for an IP separation $d_x/\sigma_{0x} = 5$, the parasitic collision separations are $d_{PC2}/\sigma_{0x,+} = 9.25$ and

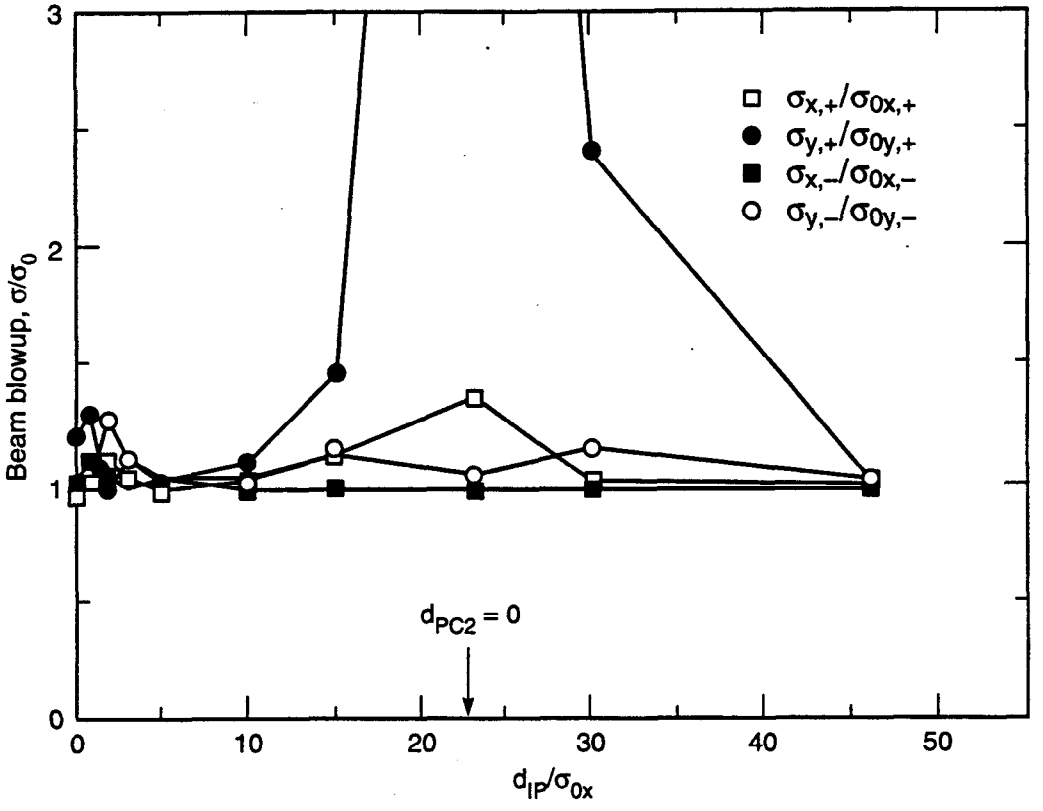

Fig. 4-104. Beam blowup as a function of horizontal beam separation at the IP. As the beam separation at the IP increases, the separation at one of the parasitic collisions (called PC1) increases, while the separation at the other (PC2) decreases. The arrow indicates the separation at which there is a head-on collision at PC2.

$d_{PC1}/\sigma_{0x,+} = 14.4$; the nominal head-on case has $d_x = 0$ and $d_{PC2}/\sigma_{0x,+} = d_{PC1}/\sigma_{0x,+} = 11.8$). However, as one might expect, when the IP separation is so large that the beams collide head-on at the PC2 location (indicated by the arrow labeled "$d_{PC2} = 0$" in the plot), the beam blowup is very large and the simulations also show particle loss. As the beams are further separated, they eventually become so far apart that there are effectively no beam-beam collisions (the last point in the plot, at the unrealistically large separation $d_x/\sigma_{0x} = 46.2$, is such that $d_{PC2}/\sigma_{0x,+} = 11.8$ and $d_{PC1}/\sigma_{0x,+} = 35.4$, and one sees that, indeed, there is no beam blowup).

In the vertical-separation case, as implied by Eq. 4-80, the beams are always more separated than nominal. The results are shown in Fig. 4-105. The LEB blowup becomes substantial (~75%) when $d_y/\sigma_{0y} \gtrsim 1$, and it does not come back down to nominal (that is, unity) until the separation is $d_y/\sigma_{0y} \gtrsim 10$–$12$, corresponding to $d_y \gtrsim \sigma_{0x}/2$.

The simulations above assume that only the first parasitic collisions and the IP come into play. However, the traditional (and simplest) closed-orbit bump is implemented by means of two kicking elements of opposite sign, separated by a distance such that the intervening phase advance is

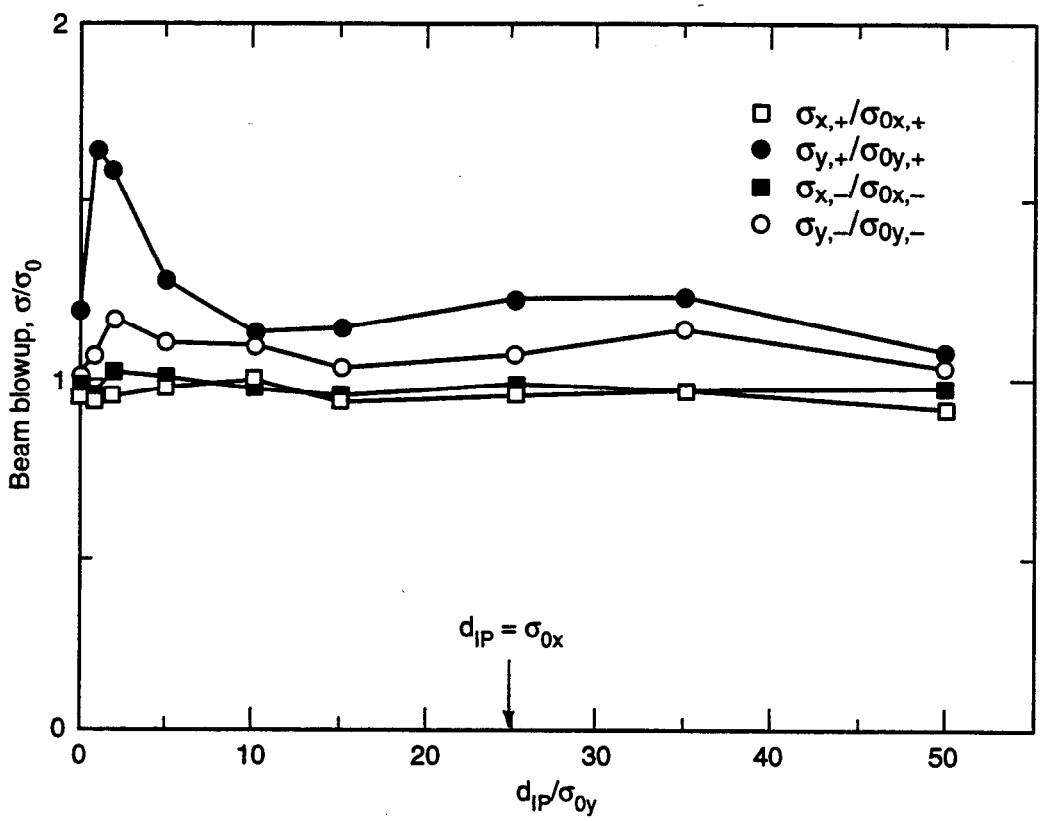

Fig. 4-105. Beam blowup as a function of vertical beam separation. As the beam separation at the IP increases, so does the separation at both PCs. The arrow indicates the point at which the vertical separation equals the nominal horizontal beam size.

$$\Delta\mu = \pi/2, 3\pi/2, 5\pi/2, \ldots \tag{4-81}$$

The PEP-II lattice is such that even the first option, $\Delta\mu = \pi/2$, implies that the bump elements must be located at a distance $\gtrsim$2.5 m from the IP. This is true for both rings, whether the separation is vertical or horizontal. This means that all four parasitic collisions on either side of the IP would be encompassed by such an orbit bump. Of course, it is, in principle, possible to separate beams by means of a more elaborate orbit bump, or a bump that is not closed. Either alternative entails complications.

Thus, if the beams are separated horizontally, the simulations above indicate that the closed-orbit bump must be tightly constrained by the lattice functions and phase advances of all the parasitic collision locations, while there is no such constraint in the vertical-separation case. If an orbit bump encompassing only the IP and the first parasitic collisions could be designed, a horizontal separation $3 \lesssim d_x/\sigma_{0x} \lesssim 10$ would seem to be adequate. (If $d_x/\sigma_{0x} \lesssim 3$, the bump would probably not be very effective, and if $d_x/\sigma_{0x} \gtrsim 10$, the adverse effects of the parasitic collisions could become quite severe.) Realistically, the orbit bump must encompass all parasitic collisions; therefore, care must

be taken in its design so that the beams do not come too close to each other at any parasitic collision point in the separated state.

The conclusion is that vertical separation is favored over horizontal on account of the diminished adverse effects from the parasitic collisions: When the beams are vertically separated, the dynamics is essentially determined by the main collision at the IP. All parasitic collisions, especially the "outer" ones, have negligible effect. A vertical separation $d_y \gtrsim (1\text{–}2)\sigma_{0x}$ is probably adequate for smooth injection. Note that, as a practical matter, it is σ_{0x} that determines the scale for the falloff of the beam blowup, whether the separation is horizontal or vertical. This implies that the orbit separation must be at least a few times σ_{0x} in magnitude (whether it is vertical or horizontal) for it to be effective. This conclusion is consistent with PEP [Chin, 1991b] and CESR [Billing, 1993] experience.

The horizontal-separation alternative does have the advantage that the simulations show no significant beam blowup when the beams are slowly brought into collision. In the vertical-separation case, on the other hand, the simulations show beam blowup of ~75% in the vertical dimension when the beam centers approach to within a distance $d_y \approx (1\text{–}2)\sigma_{0y}$. With the large PEP-II beam-stay-clear specifications, this temporary beam blowup is not a concern.

Based upon these results, a vertical injection scheme with a vertical orbit bump has been adopted for PEP-II.

4.4.7 Discussion

4.4.7.1 Effects of the Primary Parasitic Collisions: the d/σ_0 Rule. Our simulation results show that, if only the IP were considered, the PEP-II design would show behavior quite close to nominal from the beam-beam perspective, implying that the design is conservative in this sense. Limited tune scans, within the approximations embodied by our simulation methods, show that there is plenty of room to operate in the tune plane. Indeed, Fig. 4-94 shows that nominal behavior for the luminosity would persist up to values of ξ_0 significantly larger than 0.03 for the working point chosen. However, the parasitic crossings cause a preferential blowup in the vertical size of the low-energy beam that tends to limit the range of parameters for which nominal behavior prevails. Even so, Fig. 4-98a shows that the effect of the parasitic collisions is to reduce the luminosity by only ~5% from its design value for $\xi_0 = 0.03$. For the higher value of $\xi_0 = 0.05$, shown in Fig. 4-98b, the luminosity degradation from its nominal value, $\mathcal{L}_0 = 8.33 \times 10^{33}$ cm^{-2} s^{-1}, is more significant, although its absolute dynamical value, $\mathcal{L} \lesssim 7 \times 10^{33}$ cm^{-2} s^{-1}, is more than twice the PEP-II design goal.

Another way to achieve the higher-than-nominal value $\xi_0 = 0.05$ is to decrease the emittances by a factor of 3/5 at fixed bunch current. The resultant nominal luminosity in this case is a factor of 5/3 larger, that is, $\mathcal{L}_0 = 5 \times 10^{33}$ cm^{-2} s^{-1}. The beam sizes are a factor of $\sqrt{3/5}$ smaller, and the normalized parasitic separation is thus $d/\sigma_{0x,+} = \sqrt{5/3} \times 11.8 = 15.2$. A simulation for this case is shown in Fig. 4-106; the beam blowup reduces the luminosity to a dynamical value $\mathcal{L} \gtrsim 4 \times 10^{33}$ cm^{-2} s^{-1}.

By comparing the two cases at $\xi_0 = 0.05$, Figs. 4-97b and 4-106, one can see that the first one is more "effective" in increasing the luminosity from its nominal value of

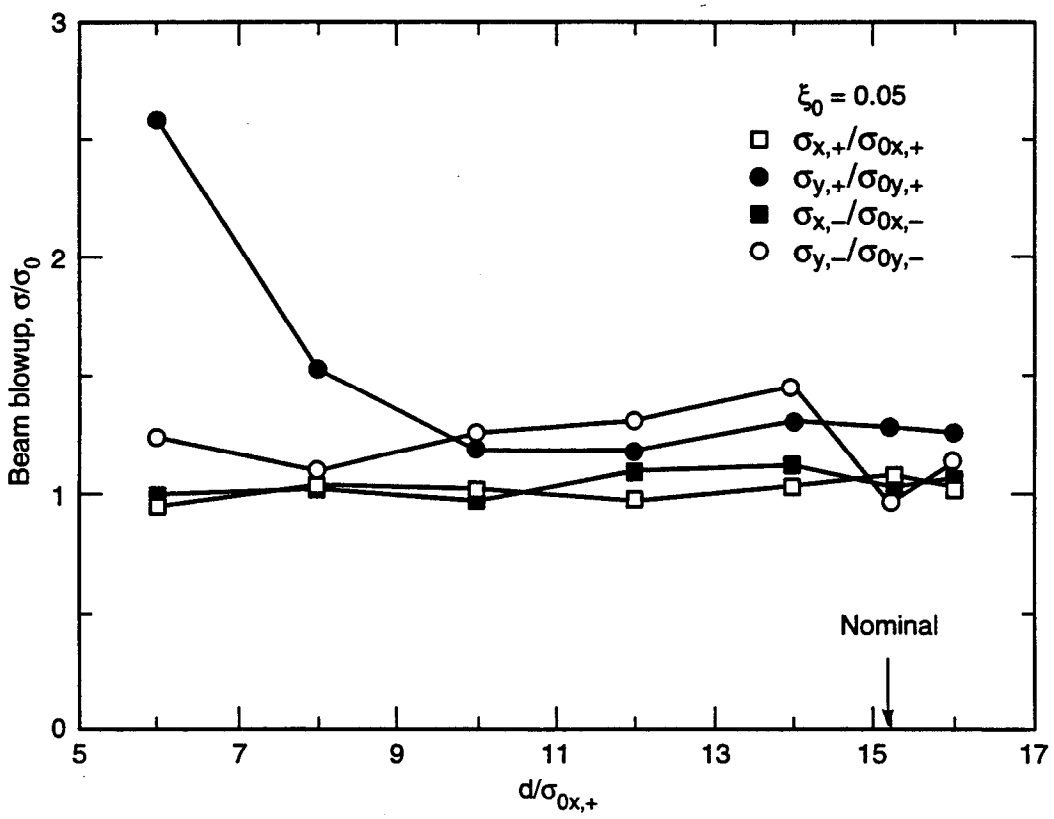

Fig. 4-106. Beam blowup factors vs $d/\sigma_{0x,+}$ for $\xi_0 = 0.05$. This value of ξ_0 is achieved by decreasing the nominal emittances by a factor of 3/5 at fixed bunch current. The corresponding nominal luminosity is 5×10^{33} cm^{-2} s^{-1}. The beam blowup reduces it to a dynamical value $\mathcal{L} \gtrsim 4 \times 10^{33}$ cm^{-2} s^{-1}.

3×10^{33} cm^{-2} s^{-1}, while the second is "safer." The greater effectiveness of the first method is due to the fact that $\mathcal{L}$ depends quadratically on N but only linearly on ε_0^{-1}. The second method is safer in the sense that the actual value of $d/\sigma_{0x,+}$, which is 15.2 in this case, is further away from the onset of significant blowup ($d/\sigma_{0x,+} \approx 9$) than in the first case, for which the actual separation value is 11.8.

All simulation cases show that, if the parasitic collision separation is sufficiently small, there is an onset of substantial beam blowup. This means that a local beam-beam limit has been reached. By examining all of our simulation cases summarized in this report and all previous studies [Chin, 1991a; Tennyson, 1991a, 1991b; Eden and Furman, 1992a, 1992b, 1993a, 1993b], we can state an approximate rule-of-thumb for this beam-beam limit, the *"d/σ_0 rule"*:

- for $\xi_0 = 0.03$, the onset of significant beam blowup occurs when $d/\sigma_{0x,+} \lesssim 7$
- for $\xi_0 = 0.05$, the onset occurs when $d/\sigma_{0x,+} \lesssim 9$

Obviously, this rule has been obtained within the context of our approximations and is thus of limited validity. In particular, it is valid only at a good working point. Nevertheless, it is consistent with similar results obtained from simulations for the

DAΦNE collider [Biscari, 1992], and is in rough agreement with the experience for minimum pretzel separation in existing machines such as CESR [Rice, 1990] and LEP [Goddard, 1992]. (In these last two cases, the constraint on d/σ_0 pertains more to beam lifetime than to core blowup, however.) We take this rule as a qualitatively valid guide for comparative assessments.

The two previous designs, APIARY 6.3D and APIARY 7.5, had nominal values $d/\sigma_{0x,+} = 7.6$ and 9.6, respectively, while the current design has $d/\sigma_{0x,+} = 11.8$. (We always use the beam size of the LEB for normalization purposes, because it is larger than the beam size of the HEB at the first parasitic crossing point and therefore gives a lower value for d/σ_{0x}.) Thus, the PEP-II design is quite safe in this respect—the large value for $d/\sigma_{0x,+}$ ensures that the parasitic collisions are effectively weak so that the dynamics of the beam core is dominated by the primary collision at the IP.

4.4.7.2 Larger Bunch Spacing. It is possible to weaken the parasitic collisions even more by operating PEP-II with a larger bunch spacing. In this case, the natural divergence of the closed orbits provides larger beam separation at the parasitic collisions. For example, one can increase the bunch spacing s_B by 50%, from 1.26 m to 1.89 m, by filling every third RF bucket rather than every second bucket (the RF wavelength is $\lambda_{RF} = 63$ cm). In this case, the first parasitic collision occurs at a distance $\Delta s = 94.5$ cm from the IP instead of 63 cm. In order to maintain ξ_0 and $\mathcal{L}_0$ at their original values of 0.03 and 3×10^{33} cm^{-2} s^{-1}, respectively, we require that the number of particles *per bunch* and nominal emittances of both beams be increased by 50%. The total beam current remains unchanged but the beam separation at the new parasitic crossing point is $d = 10.1$ mm instead of 3.5 mm. Because of intervening focusing elements, $d/\sigma_{0x,+}$ is not the same as before: The new value is $d/\sigma_{0x,+} = 20.1$ instead of 11.8, which implies a much weaker parasitic collision. Simulations for the previous designs APIARY 6.3D and APIARY 7.5 [Eden and Furman, 1992a, 1992b] show that the beam blowup is slightly less for the $s_B = 1.89$ m case than for the $s_B = 1.26$ m case at the nominal value of $d/\sigma_{0x,+}$. What is more important is that the "comfort factor" is significantly larger, since the value of 20.1 for $d/\sigma_{0x,+}$ is much larger than the rule-of-thumb threshold value of 7. Although we have not carried out these simulations for the current design, it is clear that the same conclusion about the beam blowup would be valid.

If the bunches are injected every third bucket but the emittances and bunch currents have their nominal values instead of being 50% larger, then the first parasitic collision is such that $d/\sigma_{0x,+} = 24.6$ and therefore it is truly negligible. In this case, the beam-beam parameter at the IP is still $\xi_0 = 0.03$, but the luminosity is $\mathcal{L}_0 = 2 \times 10^{33}$ cm^{-2} s^{-1}. This operating configuration could be used as a comfortable initial stage in the commissioning of the machine. Table 4-41 shows a comparison of the nominal case with the two alternatives with $s_B = 1.89$ m.

4.4.7.3 Unequal Beam-Beam Parameters. As mentioned earlier, the transparency symmetry in the PEP-II design is not obeyed exactly by the damping decrements or the synchrotron tunes. We have therefore felt motivated to explore consequences of breaking the symmetry in the beam-beam parameters as well. To this end, we carried out simulations [Eden and Furman, 1993a] for the two previous designs, APIARY 6.3D and APIARY 7.5, for unequal beam-beam parameters in two cases:

Table 4-41. Comparison of primary parameters for the nominal case with two options with larger bunch spacing.

	Nominal spacing		s_B = 1.89 larger N		s_B = 1.89 nominal N	
	LEB	HEB	LEB	HEB	LEB	HEB
s_B [m]	1.26		1.89		1.89	
$\mathcal{L}_0$ [cm^{-2} s^{-1}]	3×10^{33}		3×10^{33}		2×10^{33}	
ξ_0	0.03		0.03		0.03	
N [10^{10}]	5.6	2.6	8.4	3.9	5.6	2.6
I [A]	2.1	1.0	2.1	1.0	1.4	0.66
ε_{0x} [nm·rad]	61	46	92	69	61	46
ε_{0y} [nm·rad]	2.5	1.8	3.7	2.8	2.5	1.8
d [mm]	3.5		10.1		10.1	
d/σ_{0x}	11.8	14.3	20.1	20.4	24.6	24.8

Approach A: we set $\xi_{0x,+} = \xi_{0y,+} \equiv \xi_{0+}$ and $\xi_{0x,-} = \xi_{0y,-} \equiv \xi_{0-}$ with $\xi_{0+} \neq \xi_{0-}$

Approach B: we set $\xi_{0x,+} = \xi_{0x,-} \equiv \xi_{0x}$ and $\xi_{0y,+} = \xi_{0y,-} \equiv \xi_{0y}$ with $\xi_{0x} \neq \xi_{0y}$

In both cases, we maintained the pairwise equality of the rms beam sizes at the IP and kept the luminosity fixed at its nominal value, $\mathcal{L}_0 = 3 \times 10^{33}$ cm^{-2} s^{-1}. Other constraints were in effect. In Approach B, the transparency-symmetry constraint on the beam-beam parameters is respected, as explained in Section 4.4.2, but this is not the case in Approach A. The simulation results showed that:

- In both approaches, only the vertical beam blowup is significant, and this blowup behaves smoothly as the beam-beam parameters move away from full equality
- In Approach A, the dynamics favors (that is, beam blowup is less for) $\xi_{0+} \approx 0.024$, $\xi_{0-} \approx 0.04$ over $\xi_{0+} = \xi_{0-} = 0.03$
- In Approach B, the dynamics favors $\xi_{0y} \approx 0.023$, $\xi_{0x} \approx 0.04$ over $\xi_{0x} = \xi_{0y} = 0.03$

In both cases, the dynamical value of the luminosity is slightly increased from the values corresponding to $\xi_{0x,+} = \xi_{0y,+} = \xi_{0x,-} = \xi_{0y,-} = 0.03$. We have every reason to believe that qualitatively similar results apply to the current design. We conjecture that, if the beam-beam parameters were chosen according to the preference expressed by the dynamics, the operation of the machine would perhaps be smoother and more reliable. Of course, there are implications for other areas of the design associated with these changes. Table 4-42 shows values for selected parameters of PEP-II in two examples with unequal beam-beam parameters. Both sets are within the operational reach of the machine. We note that, in both examples, the total current of the LEB is higher than the nominal value.

Table 4-42. Two examples of modified sets of basic parameters based on different choices for the nominal beam-beam parameters, compared with the nominal specification. The nominal luminosity is $\mathcal{L}_0 = 3 \times 10^{33}$ cm^{-2} s^{-1} for all three cases.

	Nominal		Approach A		Approach B	
	LEB	HEB	LEB	HEB	LEB	HEB
ξ_{0x}	0.03	0.03	0.025	0.04	0.04	0.04
ξ_{0y}	0.03	0.03	0.025	0.04	0.025	0.025
σ_{0x} [μm]	152		144		141	
σ_{0y} [μm]	6.06		5.75		9.0	
$r \equiv \sigma_{0y}/\sigma_{0x}$	0.04		0.04		0.06	
d/σ_{0x}	11.8	14.3	12.4	15.1	12.7	15.5
I [A]	2.1	1.0	2.8	0.74	2.5	1.2

4.4.7.4 Pairwise-Equal Beta Functions. As mentioned in Section 4.4.2, a single-particle Hamiltonian analysis leads to a more restrictive set of transparency conditions than those we have adopted [Krishnagopal and Siemann, 1990b]. Motivated by this analysis, we have gone through the exercise of running one simulation case for a modified PEP-II design that satisfies this more restricted symmetry. In this particular example, we have set the beam-beam parameters and the nominal luminosity to their PEP-II nominal values of 0.03 and 3×10^{33} cm^{-2} s^{-1}, respectively, and we have chosen the beta functions at the IP to be $\beta^*_{x,+} = \beta^*_{x,-} = 50$ cm and $\beta^*_{y,+} = \beta^*_{y,-} = 2$ cm. An immediate consequence of going to this configuration is that the total current in the LEB increases to 2.9 A (which is still within the PEP-II design specification). Table 4-43 shows other basic parameters for this modified case, and Fig. 4-107 shows the results for the beam blowup as a function of the beam separation at the first parasitic collision.

In this case, one sees that the beam blowup curves behave symmetrically and tend to rise more gently as the parasitic separation decreases than in the nominal case (Fig. 4-96). However, for the nominal value of the separation, the simulation results for *both* cases show that the dynamical value of the luminosity is within a few percent of 3×10^{33} cm^{-2} s^{-1}.

4.4.7.5 Other Alternatives Studied. In the same spirit of examining departures from the nominal parameters, we also studied the two earlier designs. Specifically, we looked at (a) making $\beta^*_{x,+}$ and $\beta^*_{y,+}$ larger than nominal and (b) making $\sigma_{\ell,+}$ smaller than nominal. The object of both changes was to try to bring transparency condition (iv) closer to being satisfied. Simulations for both cases indicated slightly better luminosity performance. The penalty in case (a) is an increase in the LEB current, and in case (b) an increase in the required RF voltage and a change in the momentum compaction factor.

4.4.7.6 Simulation Parameters. As mentioned in Section 4.4.3, in all the simulation results with TRS presented above we used five damping times and 256 superparticles,

Table 4-43. Modified main PEP-II parameters used in a beam-beam simulation with pairwise-equal beta functions.

	LER (e^+)	HER (e^-)
$\mathcal{L}_0$ [$cm^{-2}\ s^{-1}$]	3×10^{33}	
ξ_{0x}	0.03	0.03
ξ_{0y}	0.03	0.03
ν_x	0.64	0.64
ν_y	0.57	0.57
ν_s	0.052	0.052
σ_ℓ [cm]	1.0	1.0
σ_E/E	1.00×10^{-3}	0.616×10^{-3}
N [a]	7.507×10^{10}	2.586×10^{10}
I [A]	2.862	0.986
β_x^* [m]	0.5	0.5
β_y^* [m]	0.02	0.02
σ_{0x}^* [μm]	175	175
σ_{0y}^* [μm]	7	7
Parameters at the first parasitic collision		
d/σ_{0x}	12.4	12.4
ξ_{0x}	–0.0002	–0.0002
ξ_{0y}	+0.003	+0.003

[a]These values for N do not take into account the existence of the ion-clearing gap.

and represented thick-lens beam-beam effects by using five slices. In order to save computer time, in some cases (typically tune scans) we used fewer superparticles or ran the simulation for only three damping times. In general, for $\xi_0 = 0.03$, the results are qualitatively the same. As an example of these kinds of comparisons, we present below a spot-check with more superparticles. Figure 4-108 shows results with 256 and with 1024 superparticles for the vertical blowup of the LEB, for the nominal design case. The curve with 256 superparticles is taken from Fig. 4-96. One can see that there is essentially no difference in the two cases.

4.4.8 Conclusions

Our results show that, without the parasitic crossings, the beam dynamics performance of the machine is quite close to nominal, up to values of ξ_0 substantially higher than the

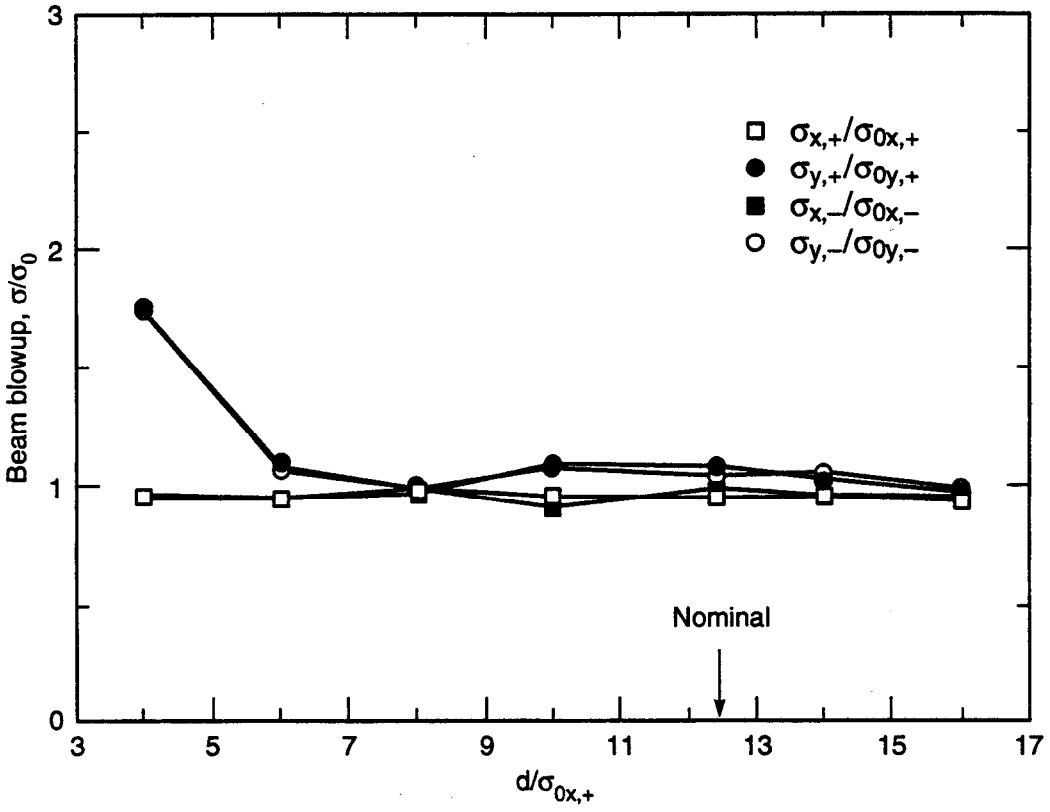

Fig. 4-107. Beam blowup factors vs $d/\sigma_{0x,+}$ for a beam-beam simulation (using TRS) with pairwise-equal beta functions. This should be compared with the nominal case, shown in Fig. 4-96.

design specification of 0.03. The parasitic crossings introduce a horizontal-vertical coupling due to the large value of the vertical beta function. This has the effect of increasing the vertical size of the low-energy beam, with a corresponding lowering of the luminosity. However, because the other three transverse beam sizes are not changed much, the luminosity degrades no more than 5% from its nominal value for $\xi_0 = 0.03$. For $\xi_0 = 0.05$, the relative degradation is larger, of the order of 15%; however, since the nominal luminosity is larger in this case ($\mathcal{L}_0 = 8.3 \times 10^{33}$ cm^{-2} s^{-1}), the *absolute* value of the luminosity is about 7×10^{33} cm^{-2} s^{-1}, which exceeds the PEP-II design specification.

The calculated results for the value of $\xi_0 = 0.05$ were achieved by increasing the bunch currents by a factor of 5/3 from the nominal values at fixed emittance. Another way of achieving $\xi_0 = 0.05$ is to decrease the emittances by a factor of 3/5 at fixed bunch current. In this case, because of the reduced beam size, the parasitic collisions have an increased normalized separation, namely $d/\sigma_{0x,+} = 15.2$ instead of a nominal value of 11.8. The expected luminosity in this case is $\mathcal{L}_0 = 5 \times 10^{33}$ cm^{-2} s^{-1}, but the beam blowup leads to a dynamical value of $\mathcal{L} \gtrsim 4 \times 10^{33}$ cm^{-2} s^{-1}. This second mode of operation with $\xi_0 = 0.05$ is somewhat more easily accomplished than the first as a result of the lower beam-current requirements and the larger parasitic collision separation.

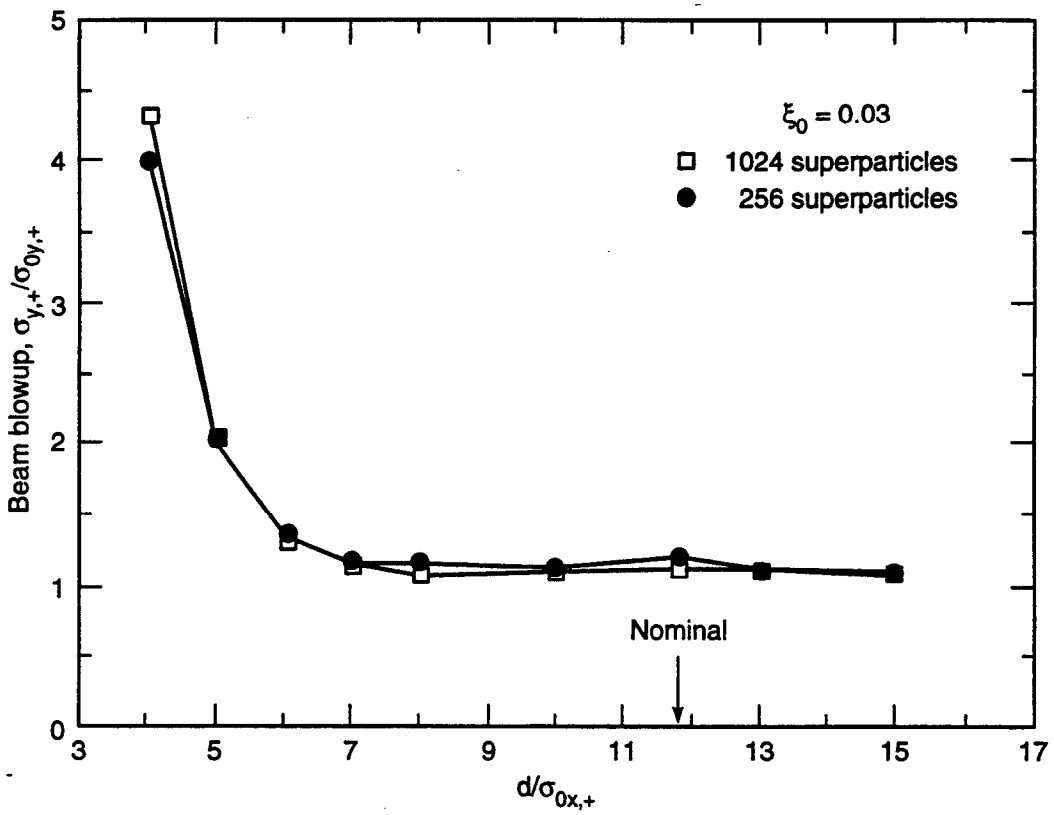

Fig. 4-108. Comparison of simulation results with TRS for 256 vs 1024 superparticles per bunch. The vertical blowup factor of the LEB is plotted vs $d/\sigma_{0x,+}$ for the nominal design case. The curve with 256 superparticles is taken from Fig. 4-96.

Our simulations for luminosity performance, based on studies of the dynamics of the beam core, suggest a simple rule-of-thumb for the effective weakness of the parasitic collisions: Once a good working point has been found, the parasitic collisions are effectively weak when $d/\sigma_{0x,+} \gtrsim 7$ for $\xi_0 = 0.03$ (or $d/\sigma_{0x,+} \gtrsim 9$ for $\xi_0 = 0.05$). Obviously, a prudent approach dictates choosing a design value for $d/\sigma_{0x,+}$ larger than 7; all our evidence to date confirms that the nominal separation value of 11.8 for PEP-II will be quite comfortable.

The influence of parasitic crossings beyond the first one is quite weak. (To take account of these collisions may require a very small adjustment of the working point.) They may induce a coherent dipole oscillation in the beams, but this instability should be easily avoided by a suitable choice of working point.

In general, from the perspective of beam-beam dynamics, we conclude that the energy asymmetry of PEP-II presents no qualitatively new problems compared with those arising in single-ring colliders.

Although our studies show completely acceptable luminosity performance of the nominal design, we have explored to some extent how this performance varies as some parameters take on values that are different from, but close to, nominal. Obviously these

changes would have implications for other areas of the design, or for the operation of the machine. Three such variations are:

- Increase the bunch spacing from $2\lambda_{RF} = 1.26$ m to $3\lambda_{RF} = 1.89$ m, with a concomitant increase in emittances and bunch currents, so that the total beam current, nominal beam-beam parameters, and nominal luminosity remain unchanged
- Adopt unequal beam-beam parameters according to two approaches: (A) make the beam-beam parameters of the LEB different from those of the HEB, but keep the horizontal and vertical parameters equal for each beam; (B) make the beam-beam parameters equal in the two beams, but horizontal parameters different from vertical
- Set the beta functions at the IP pairwise equal

Because the luminosity performance is already quite close to nominal, these alternatives do not improve the performance more than a few percent for $\xi_0 = 0.03$. Thus, the advantage of making these changes may only be in further weakening the effect of the parasitic collisions compared with the nominal design.

Beam-beam simulations of the injection process show that the vertical injection scheme with vertical beam displacement is quite comfortable, since it induces a temporary beam blowup of only a factor of three, which is easily accommodated within the physical aperture.

The lifetime is an important issue that we are just beginning to study. This is the most difficult and expensive part of beam-beam simulations. Preliminary results show that, in the absence of machine nonlinearities, the beam lifetime is comfortably long. (Thus far, we have not included magnet nonlinearities in the simulation studies.) Because magnet nonlinearities are more important at the tails of the beam than at the core, they are unlikely to affect the luminosity performance of PEP-II. However, their influence on the beam lifetimes may be significant and should be estimated.

Based on our results, and the possibilities for improvement described above, we are convinced that the PEP-II design with a luminosity of 3×10^{33} cm^{-2} s^{-1} is quite comfortable. While important issues remain to be studied in more detail, such as beam lifetimes, optimal choice of working point, and effects of magnet nonlinearities on beam dynamics performance, we are confident that our solution will meet and has margin to exceed its luminosity goals.